

© 2019 by Akshat Puri. All rights reserved.

MEASUREMENT OF ANGULAR AND MOMENTUM DISTRIBUTIONS OF CHARGED
PARTICLES WITHIN AND AROUND JETS IN Pb+Pb AND pp COLLISIONS AT
 $\sqrt{S_{NN}} = 5.02$ TeV WITH ATLAS AT THE LHC

BY

AKSHAT PURI

DISSERTATION

Submitted in partial fulfillment of the requirements
for the degree of Doctor of Philosophy in Physics
in the Graduate College of the
University of Illinois at Urbana-Champaign, 2019

Urbana, Illinois

Doctoral Committee:

Professor Matthias Grosse Perdekamp, Chair
Professor Anne Marie Sickles, Advisor
Professor Aida El-Khadra
Professor Bryce Gadaway

Abstract

Studies of the fragmentation of jets into charged particles in heavy-ion collisions can help in understanding the mechanism of jet quenching by the hot and dense matter created in such collisions, the quark-gluon plasma. This thesis presents a measurement of the angular distribution of charged particles around the jet axis as measured in Pb+Pb and pp collisions collided at a center of mass energy of $\sqrt{s_{\text{NN}}} = 5.02$ TeV. The measurement is done using the ATLAS detector at the Large Hadron Collider, and utilizes 0.49 pb^{-1} of Pb+Pb and 25 pb^{-1} of pp data collected in 2015. The measurement is performed for jets reconstructed with the anti- k_t algorithm with radius parameter $R = 0.4$, and is extended to regions outside the jet cone. Results are presented as a function of Pb+Pb collision centrality, and both jet and charged-particle transverse momenta. It was observed that in Pb+Pb collisions there is a broadening of the jet for charged particles with $p_T < 4$ GeV, along with a narrowing for charged particles with $p_T > 4$ GeV. Ratios between the angular distributions in Pb+Pb and pp showed an enhancement for particles with $p_T < 4$ GeV in Pb+Pb collisions, with the enhancement increasing up to 2 for $r < 0.3$, and remaining constant for $0.3 < r < 0.6$. Charged particles with $p_T > 4$ GeV show a small enhancement in the jet core for $r < 0.05$, with a growing suppression of up to 0.5 for $r < 0.3$ in Pb+Pb collisions. The depletion remains constant for $0.3 < r < 0.6$.

For my Mother, Father, and Brother

Contents

Chapter 1 Introduction	1
Chapter 2 Experimental Setup	3
2.1 The Large Hadron Collider	3
2.2 The ATLAS Detector	5
2.2.1 Inner Detector	5
2.2.2 Calorimeter	7
2.2.3 Muon Spectrometer	9
2.2.4 Other subsystems	9
Chapter 3 ATLAS Qualification Task	12
3.1 Introduction	12
3.2 Datasets and Event Selection	12
3.3 Procedure	16
3.4 Uncertainties	17
3.4.1 Cross calibration factor uncertainties	17
3.4.2 Uncertainties on HI JER	18
3.5 Qualification Task Conclusion	28
Chapter 4 Measurement of Angular Correlations Between Tracks And Jets	29
4.1 Definition of Measured Quantities	29
4.2 Input Data	32
4.2.1 Data samples	32
4.2.2 Trigger Selection	33
4.2.3 Monte Carlo Samples	34
4.3 Event Selection	37
4.3.1 Centrality Selection	38

4.4	Jet Reconstruction	39
4.5	Basic Cuts and Corrections	44
4.5.1	Jet Selection and final energy calibration	44
4.5.2	Track selection	46
4.5.3	Track momentum correction	51
4.5.4	Track reconstruction efficiency	51
4.5.5	Fake rates	57
4.5.6	Underlying event subtraction of tracks	60
4.5.7	Unfolding	72
4.6	Systematic Uncertainties	75
4.6.1	Jet energy scale uncertainty	77
4.6.2	Jet energy resolution	78
4.6.3	Track selection and efficiency	78
4.6.4	Systematic uncertainty due to unfolding	79
4.6.5	Systematic uncertainty due to the UE event subtraction	80
4.6.6	MC non-closure	80
4.6.7	Correlations between the systematic uncertainties in Pb+Pb and pp collisions	81
4.7	Results	82
4.8	Discussion	104
4.8.1	$R_{D(p_T,r)}$ distributions	104
4.8.2	Differences of $D(p_T, r)$ distributions	107
4.8.3	p_T integrated distributions	109
A	Appendix A HI JER Uncertainty	112
A.0.1	Deriving the HI JER	112

Chapter 1

Introduction

The Large Hadron Collider (LHC) at the European Center for Nuclear Research (CERN), is one of the worlds most expensive and complicated machines. It was built with the purpose of accelerating subatomic particles to close to the speed of light and colliding them to study their underlying structure. Detectors around the LHC ring, the biggest of which are ATLAS (A Toroidal LHC ApparatuS), CMS (Compact Muon Solenoid), ALICE (A Large Ion-Collider Experiment), and LHCb (LHC-Beauty), study these collisions and use the debris as a playground to verify and expand the "Standard Model" of particle physics. This thesis will focus on measurements of collisions involving heavy ions as measured by the ATLAS detector.

Relativistic heavy ion collisions such as those at the LHC provide insight into the interactions between quarks and gluons. These fundamental building blocks of all matter interact via the strong force, the theoretical framework of which is described by Quantum Chromodynamics (QCD). This theory dictates that quarks and gluons are confined, i.e. locked together to form composite particles and cannot exist independently, making their study extremely difficult. Relativistic heavy ion collisions provide an extreme environment where nuclear matter can "melt" and form a deconfined medium that consists of free quarks and gluons. This state of matter, called the Quark Gluon Plasma (QGP) is what existed a few microseconds after the Big Bang, and is what eventually cooled and expanded to form the existing universe. It

The quark-gluon plasma (see Refs. [1, 2] for recent reviews) can be probed by jets, sprays of particles that come from hard scattering processes between the nucleons involved in the collision. These jets are produced early in the collision and interact with the QGP as they make their way to the detector. Studying the rates and characteristics of these jets in Pb+Pb collisions, and comparing them to similar quantities in pp collisions can provide information on the properties of the QGP. In particular, studying the fragmentation pattern of these jets and how the energy is distributed around the jet axis can provide more information on the jet structure and put constraints on the medium response to the jet.

This thesis is split into 4 main chapters. An overview of the LHC and the ATLAS detector is given in Chapter 2, Chapter ?? will describe the QCD framework that will give context to the measurements discussed, Chapter 3 will describe the work undertaken to become a member of the ATLAS Collaboration,

and Chapter 4 will provide a detailed description of the measurement to determine the angular distributions of charged particles in Pb+Pb and pp collisions.

Chapter 2

Experimental Setup

This section will describe the large hadron collider complex and the ATLAS detector and its various subsystems.

2.1 The Large Hadron Collider

The Large Hadron Collider (LHC) is a part of the European Organization for Nuclear Research (CERN). It has a circumference of 27 kilometers, making it the world's largest particle accelerator, and is housed in a tunnel that is up to 175 meters below the surface of the earth. The LHC ring has eight arcs and eight straight sections, with each straight section being approximately 528 m long. Four of the straight sections are where the major detectors are located, while the other four are used for machine utilities, radio frequency, collimation and beam dumps. The arc sections are built using 1232 dipole superconducting magnets, providing a magnetic field of up to 8.33 T. Another 392 quadrupole magnets are used for focussing the particle beam. Sixteen radio frequency (RF) cavities that provide a voltage of 2 MV and operate at 400 MHz are used to accelerate the proton or ion beams that are kept in their circular path by the dipole magnets. The magnets are cooled down to 1.9 K via liquid Helium.

The LHC beam pipe has two rings with the counter-rotating beams and uses a twin-bore magnet design that optimizes for both cost, as well as space. The counterrotating beams require opposite magnetic dipole fields in both rings, with separate magnetic and vacuum chambers, with the common sections only at the insertion regions and where the major experimental detectors are located. These detectors are: A Toroidal LHC Apparatus (ATLAS), Compact Muon Solenoid (CMS), A Large Ion Collider Experiment (ALICE), and Large Hadron Collider - Beauty (LHCb) [3].

Studying the rare events that the LHC was designed for requires high beam energies and intensities, and the LHC is capable of reaching up to center of mass energies, $\sqrt{s} = 14$ TeV for protons and $\sqrt{s_{NN}} = 5.5$ TeV for lead ions. The LHC delivers up to $10^{34}\text{cm}^2\text{s}^{-1}$ of luminosity to the ATLAS and CMS detectors when colliding protons. The LHCb detector is a lower luminosity experiment, that receives up to $10^{32}\text{cm}^2\text{s}^{-1}$, and ALICE, a dedicated ion experiment aims at a peak luminosity of $10^{27}\text{cm}^2\text{s}^{-1}$ for nominal lead-lead operation.

A schematic of the entire accelerator complex and the path followed by protons and heavy ions is shown in Fig. 2.1. The protons in the LHC are obtained by stripping a hydrogen atom of its electrons with an electric field. They are then supplied to the LHC via the Linac2 - Proton Synchrotron Booster - Proton Synchrotron - Super Proton Synchrotron chain. The complete ionization of lead on the other hand is done in multiple stages, with the first stage in Linac3, which provides Pb^{+29} via an ion source. The Pb^{+29} lead ions are further stripped of electrons by passing them through a $0.3 \mu\text{m}$ foil. The Pb^{+54} ions are selected via mass spectrometer and sent to the Low Energy Ion Ring (LEIR), followed by the Proton Synchrotron and Super Proton Synchrotron, and then finally the LHC. The final stripping of lead ions takes place after the PS, on a 0.8 mm thin aluminum foil.

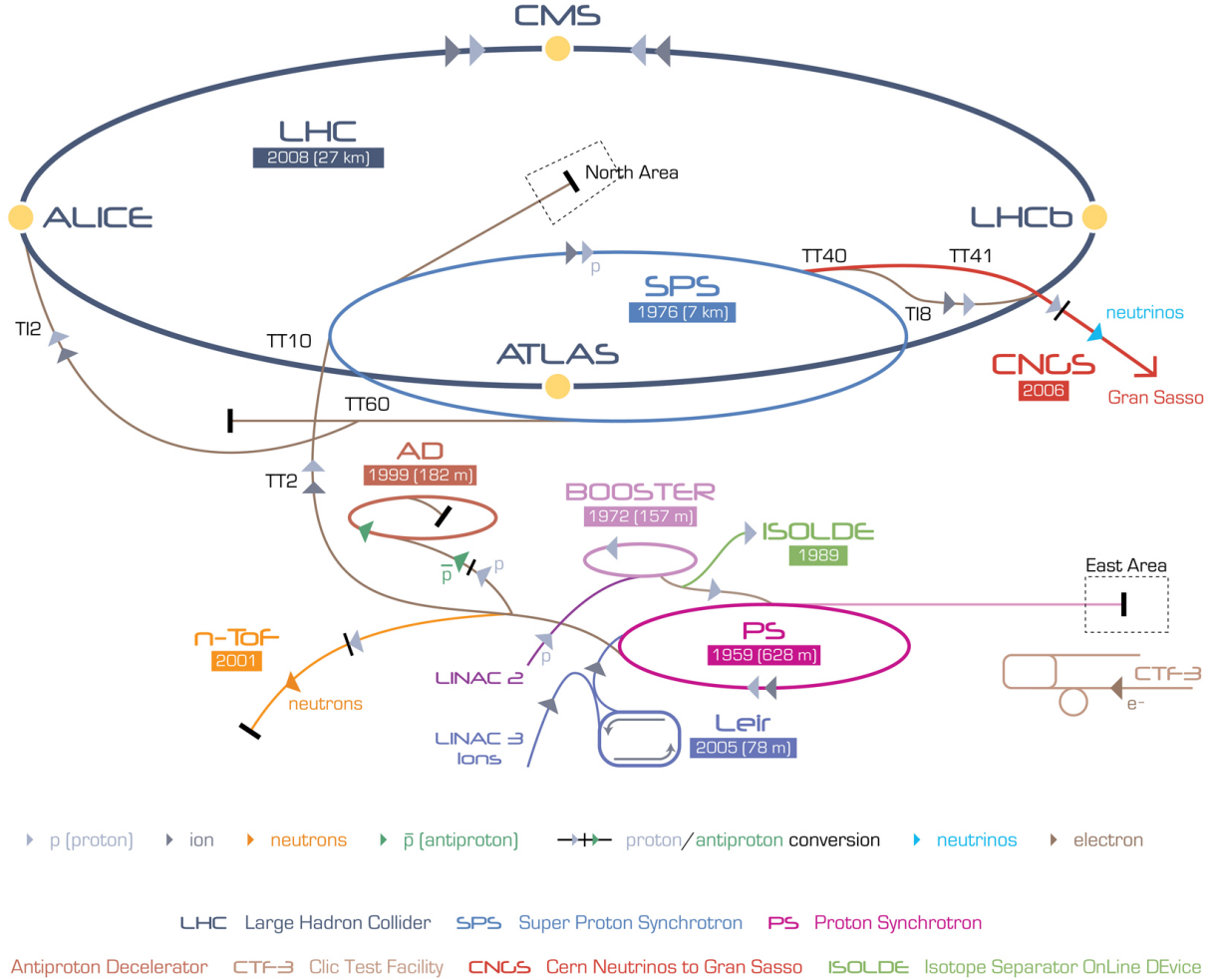


Figure 2.1: The accelerator complex at CERN. ATLAS can be seen inside the SPS on the LHC ring. Figure taken from Ref. [4]

The LHC beams consist of bunches of protons or lead ions with a nominal bunch spacing of 25 ns that corresponds to 2808 bunches.

In 2015, the LHC delivered an integrated luminosity of 0.49 pb^{-1} of Pb+Pb and 25 pb^{-1} of pp data.

2.2 The ATLAS Detector

The ATLAS detector (Fig. 2.2) is a general purpose detector at the LHC. It uses a right-handed coordinate system with its origin at the nominal interaction point (IP) in the centre of the detector and the z -axis along the beam pipe. The x -axis points from the IP to the centre of the LHC ring, and the y axis points upward. Cylindrical coordinates (r, ϕ) are used in the transverse plane, ϕ being the azimuthal angle around the beam pipe. The pseudorapidity is defined in terms of the polar angle θ as $\eta = -\ln \tan(\theta/2)$. The detector is symmetric in the forward-backward direction, with the positive z direction being the A side, and the negative z direction being the C side. It has full 2π coverage in azimuth. The transverse momentum p_T , the transverse energy E_T , and the missing transverse energy $E_{T\text{miss}}$ are defined in the $x - y$ plane unless stated otherwise. The distance ΔR in the pseudorapidity-azimuthal angle space is defined as $\Delta R = \sqrt{\Delta\eta^2 + \Delta\phi^2}$.

The detector was designed keeping in mind the goals of the physics it aimed to explore, and as such has the following characteristics:

- Fast, radiation-hard electronics and sensor
- Fine granularity to be able to manage large particle fluxes
- Large acceptance in pseudorapidity and full azimuthal coverage
- Good electromagnetic calorimetry for photon and electron identification
- Good hadron calorimetry for accurate jet and missing transverse energy measurements
- Good muon identification and momentum resolution
- Highly efficient trigger system

These design goals are achieved with the main subsystems: the inner detector, the calorimeter, the muon spectrometer, and the trigger system. The main analysis discussed in this thesis uses the inner detector, calorimeter, and the trigger system. The muon system is described for completeness.

2.2.1 Inner Detector

The inner detector (Fig. 2.3) is designed to reconstruct the charged particle trajectories for particles with momenta down to 0.5 GeV in the interval $|\eta| < 2.5$. It is immersed in a 2T magnetic field from the central

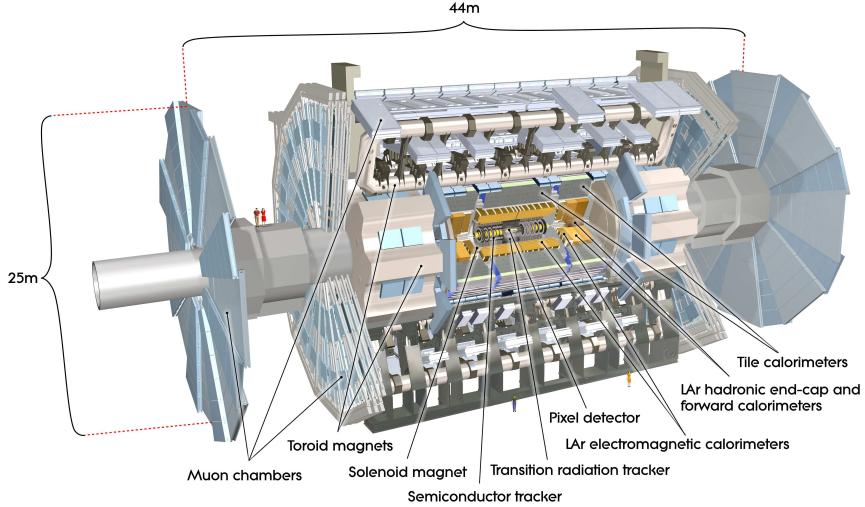


Figure 2.2: The ATLAS detector. Figure taken from Ref. [5].

solenoid that covers a region of 5.3 m long and has a diameter of 2.5 m. The inner detector has capabilities for pattern recognition, momentum and vertex measurements, and electron identification. These measurements are made using the inner pixel detector, the semi-conductor tracker (SCT), and the transition radiation tracker (TRT).

Pixel system: This system is segmented in $R - \phi$ and comprises of four pixel layers : the innermost insertable B layer (IBL) and three identical silicon pixel detectors. The IBL was added to the ATLAS detector during the first long shutdown of the LHC in 2013-2014. It consists of 14 carbon fiber staves, 2 cm wide and 64 cm long, surrounding the beam pipe at a mean radius of 33 mm, and covering a pseudorapidity region of ± 3 . Each stave consists of 26880 pixels in a matrix of 80 columns ($50 \mu\text{m}$ pitch), by 336 rows ($250 \mu\text{m}$ pitch) [6, 7]. The other three layers have a pixel size in $R - \phi \times z$ of $50 \times 400 \mu\text{m}^2$. The accuracies in the barrel region are $10 \mu\text{m}^2 (R - \phi)$ and $115 \mu\text{m}^2 (z)$. The end cap regions have an accuracy of $10 \mu\text{m}^2 (R - \phi)$ and $115 \mu\text{m}^2 (R)$. The hit resolution ranges from $\sim 8 (R - \phi)$ and $\sim 40 \mu\text{m} (z)$ for the innermost layer, to $\sim 10 \mu\text{m} (R - \phi)$ and $\sim 115 \mu\text{m} (z)$ for the next three layers [5]. The pixel detector has approximately 80.4 million readout channels.

Semi Conductor Tracker: This subsystem has a coverage that overlaps with the pixel layers, and is arranged in concentric cylinders around the beam axis, with the end caps being disks perpendicular to the beam axis. The SCT has eight strip ($80 \mu\text{m}$ pitch) layers that are crossed by each track. Small angle stereo strips (40 mrad) are used to measure both coordinates, with one set of strips in each layer, parallel to the beam direction. The end cap region has nine layers of double sided modules with strips in the radial

direction, with each also having a mean pitch of $80\ \mu\text{m}$. The intrinsic resolution is $\sim 17\mu\text{m}$ ($R - \phi$) and $\sim 580\mu\text{m}$ (z). There are approximately 6.3 million readout channels from the SCT. [5].

Transition Radiation Tracker: The TRT uses a combination of a xenon based gas and 4mm diameter straw tubes and provides for a large number of hits (up to 36) per track. It covers the region $|\eta| < 2.0$, and has a resolution of $\sim 130\mu\text{m}$ in $r - \phi$, with no information in the z direction. The barrel region of the TRT has straws that are 144 cm long and are parallel to the beam axis, with the wires divided into two halves at $\eta = 0$. The end-caps have 37 cm long straws in a radial configuration. The TRT has approximately 315,000 channels. [5].

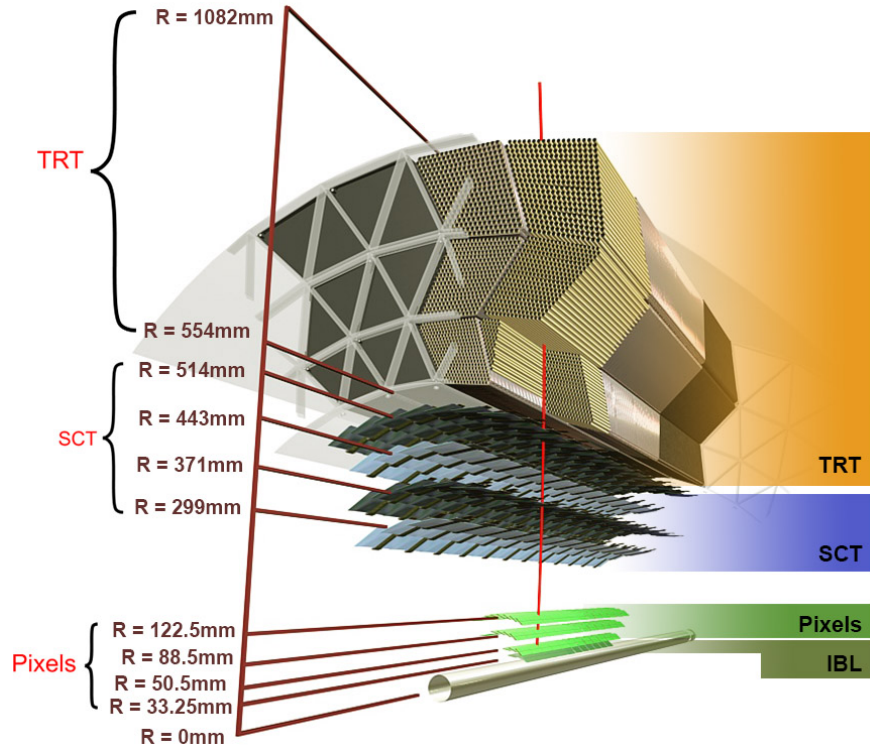


Figure 2.3: ATLAS Inner Detector System

2.2.2 Calorimeter

The calorimeter covers the eta range of $|\eta| < 4.9$ for using a variety of different techniques. The parameters are summarized in the table below. Over the eta $|\eta| < 2.5$, where there is overlap with the inner detector, the highly granular electromagnetic calorimeter is used for precision measurements of electrons and photons. The rest of calorimeter has coarser granularity that is sufficient for jet reconstruction. The calorimeter contains the electromagnetic and hadronic showers, and limits the punch through to the muon system. The EMCal has a

radiation depth greater than 22 radiation lengths in the barrel, and greater than 24 radiation lengths in the end caps. The approximately 10 interaction lengths in the barrel and end cap provide good resolution for high energy jets. The total thickness of the calorimeter is 11 interaction lengths at $\eta = 0$. The calorimeter is divided into different subsystems, including the Liquid Argon Electromagnetic Calorimeter (LAr EMCal) and the Hadronic calorimeter (HCal).

LAr EMCal: The EMCal covers the region $|\eta| < 1.475$ and has two end caps ($1.375 < |\eta| < 3.2$). It also contains the central solenoid. The barrel calorimeter is divided into two half barrels, separated by 4mm at $z = 0$. Each end cap is divided into two coaxial wheels, with the inner one covering $2.5 < |\eta| < 3.2$ and the outer one covering $1.375 < |\eta| < 2.5$. The EMCal uses accordion shaped kapton electrodes and lead absorber plates that provide full azimuthal symmetry. The EMCal is subdivided into three sections in its depth over $|\eta| < 2.5$, the region used for precision physics. The $|\eta| < 1.8$ region also uses a pre-sampler detector that uses an active LAr layer to correct for energy lost upstream of the calorimeter. A main source of this loss is the central solenoid.

Hadronic Calorimeter: The hadronic calorimeter consists of the tile, LAr Hadronic end cap, and the LAr forward calorimeter. The tile covers the region $|\eta| < 1.0$, with its two barrels covering the range eta $0.8 < |\eta| < 1.7$. It uses steel as the absorber and scintillating tiles for the active material. The tile calorimeter extends radially from an inner radius of 2.28 m to 4.25 m. It has a three layer that are 1.5, 4.1, and 1.8 interaction lengths thick in the barrel region, and 1.5, 2.6, and 3.3 interaction lengths in the extended barrel region. The total detector thickness is 9.7 interaction lengths at $\eta = 0$.

The LAr hadronic end cap calorimeter (HEC) consists of two independent wheels per end cap, and is behind the EMCal end cap. It extends out from $1.5 < |\eta| < 3.2$, and overlaps with the forward calorimeter and the tile calorimeter. The HEC covers the radial region of 0.475 to 2.03 m.

The LAr Forward calorimeter provides coverage over the $3.1 < |\eta| < 4.9$. It is approximately 10 interaction lengths deep, and has three modules, one of which is optimized for electromagnetic measurements, while the other two for hadronic measurements. Each module is made of concentric rods and tubes parallel to the beam axis.

A summary of the depth of the calorimeter in terms of the interaction lengths, as a function of pseudorapidity is shown in Fig. 2.4.

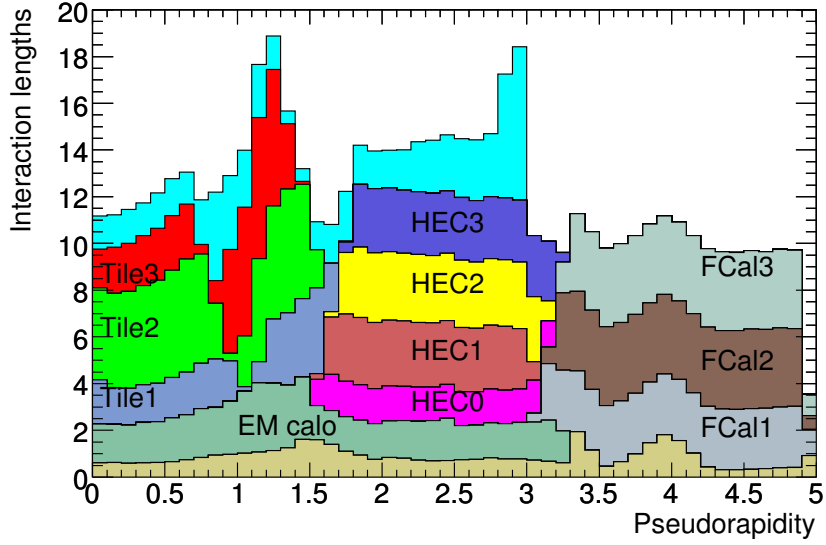


Figure 2.4: Cumulative material in the calorimeter system in units of interaction length as a function of $|\eta|$.

2.2.3 Muon Spectrometer

The muon spectrometer is based on the magnetic deflection of muon tracks in the toroid magnets. The barrel toroid provides bending over the $|\eta| < 1.4$ range, and the end cap magnets provide bending in the $1.6 < |\eta| < 2.7$ range. In the transition region ($1.4 < |\eta| < 1.6$), the magnetic deflection is from a combination of the barrel and end-cap fields. The barrel region has tracks that are measured in chambers in a cylindrical configuration around the beam axis. The transition and end-cap have chambers perpendicular to the beam axis.

2.2.4 Other subsystems

Other major subsystems of the ATLAS detector include the Zero Degree Calorimeter (ZDC), the trigger system

ZDC

The zero degree calorimeter plays a key role in determining the centrality of heavy ion collisions. It consists of quartz rods and tungsten plates, and measures neutral particles at $|\eta| \geq 8.2$. It is made of four modules, one electromagnetic, and three hadronic. The Modules are made of 11 tungsten plates that are perpendicular to the beam direction. Photomultiplier tubes are used to detect the Cherenkov radiation from particle showers.

Trigger System

The trigger and data acquisition system (TDAQ) have different subsystems that are associated with sub-detectors. There are three distinct levels: L1, L2, and the event filter. The latter two form the High Level Trigger (HLT) system. The L1 trigger, shown in Fig.2.5, uses custom electronics, while the HLT, shown in Fig.2.6, is software based. Each level uses information from the previous level to select events.

The first level uses limited detector information and makes decisions based on muons, electron, photons, jets, and τ -leptons carrying a high transverse momentum. It is also capable of identifying large missing and total transverse energy. It has a maximum acceptance rate of 75kHz and makes a decision in less than $2.5\mu s$. This event rate is further reduced to 200 Hz by the HLT that uses the full granularity and precision of the inner detector, calorimeter and muon systems to select events.

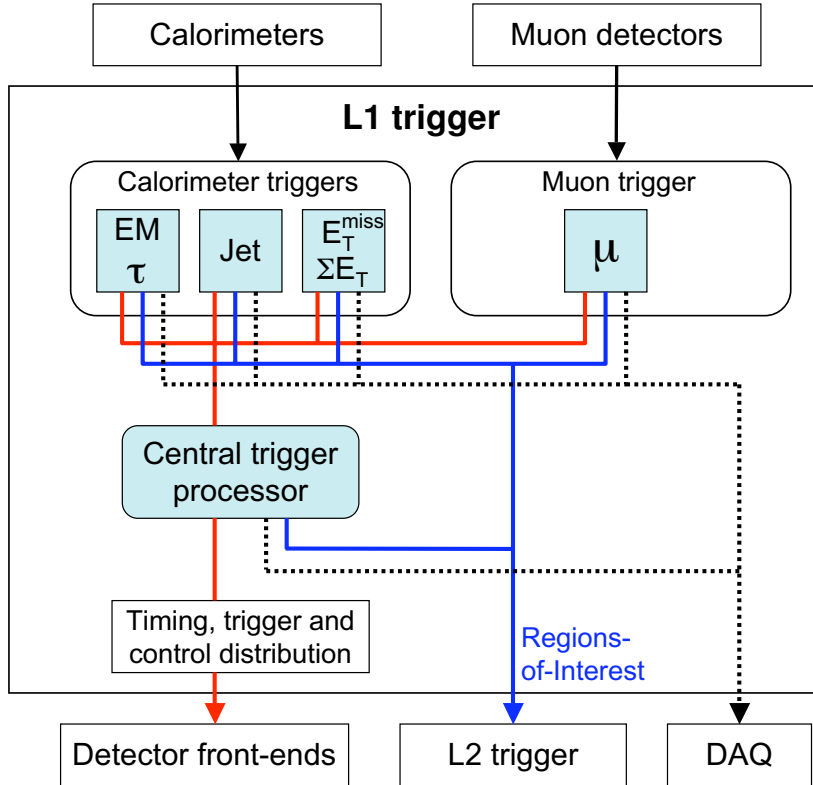


Figure 2.5: Block diagram of the L1 Trigger System.

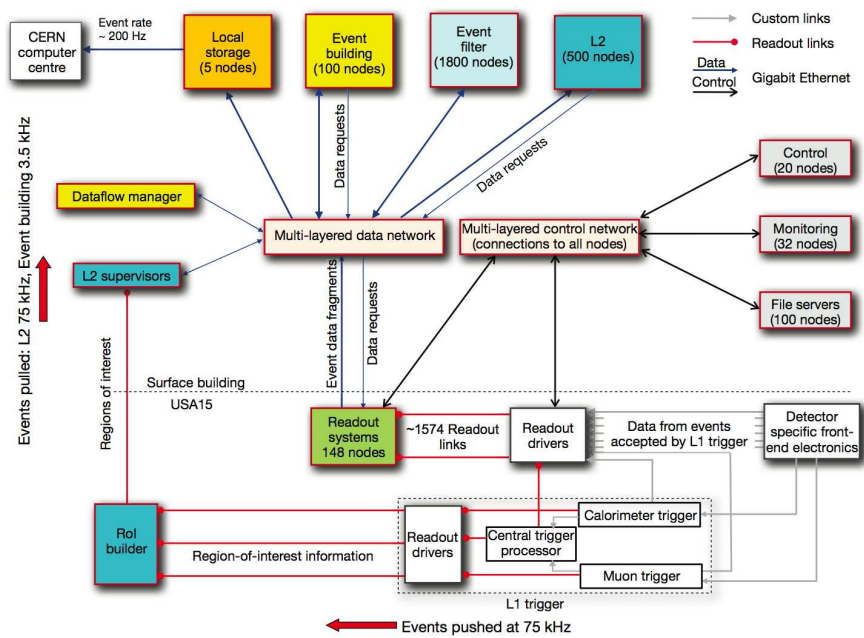


Figure 2.6: Block diagram of the HLT Trigger system.

Chapter 3

ATLAS Qualification Task

To gain authorship in the ATLAS collaboration, one has to contribute towards ATLAS technical work. My qualification task was to derive the cross calibration heavy ion jets and the related uncertainties. The aim of the cross calibration procedure, first described in [8] is to use jets constructed by the pp jet reconstruction algorithm (EMTopo jets) [9–11] to calibrate jets reconstructed using the heavy ion reconstruction algorithm (HI jets) discussed in [12].

Deriving and applying this calibration was vital to all Run 2 heavy ion jet analyses from ATLAS [13–16].

3.1 Introduction

The performance of the EMTopo jets is well understood in pp collisions [9] [10]. The goal of the cross calibration procedure, first described in [8] is to use these jets to calibrate the HI jets, that are reconstructed using the HI reconstruction algorithm discussed in [12]. On average, the p_T of the HI jets is expected to differ from the EMTopo jets due to the differences in the reconstruction algorithm, and the insitu corrections that are applied to the latter. The insitu corrections cannot directly be derived for heavy ions because of the high multiplicity, but comparing the HI and EMTopo jets in data and MC and scaling the HI jets with the ratio of $\langle p_T^{\text{HI}} / p_T^{\text{EMTopo}} \rangle$ in data and MC allows the application of EMTopo insitu corrections to HI jets [8]

3.2 Datasets and Event Selection

The data used in the cross calibration study was obtained in the 2015 13 TeV run, and the MC was generated as part of the MC15 period C. A list of the datasets is given in Table 3.1.

Table 3.1: List of datasets

Datasets	#Events [Millions]
group.phys-hi.data15_13TeV.ZeroBias.merge.AOD.p2634.2016HIPAOD	12M
group.phys-hi.data15_13TeV.express_express.merge.AOD.p2634.2016HIPAOD	2M
mc15_13TeV.361021.Pythia8EvtGen_A14NNPDF23LO_jetjet_JZ1W.merge.AOD.e3569_s2832_r7968_p2686	2M
mc15_13TeV.361022.Pythia8EvtGen_A14NNPDF23LO_jetjet_JZ2W.merge.AOD.e3668_s2832_r7968_p2686	2M
mc15_13TeV.361023.Pythia8EvtGen_A14NNPDF23LO_jetjet_JZ3W.merge.AOD.e3668_s2832_r7968_p2686	2M
mc15_13TeV.361024.Pythia8EvtGen_A14NNPDF23LO_jetjet_JZ4W.merge.AOD.e3668_s2832_r7968_p2686	2M
mc15_13TeV.361025.Pythia8EvtGen_A14NNPDF23LO_jetjet_JZ5W.merge.AOD.e3668_s2832_r7968_p2686	2M

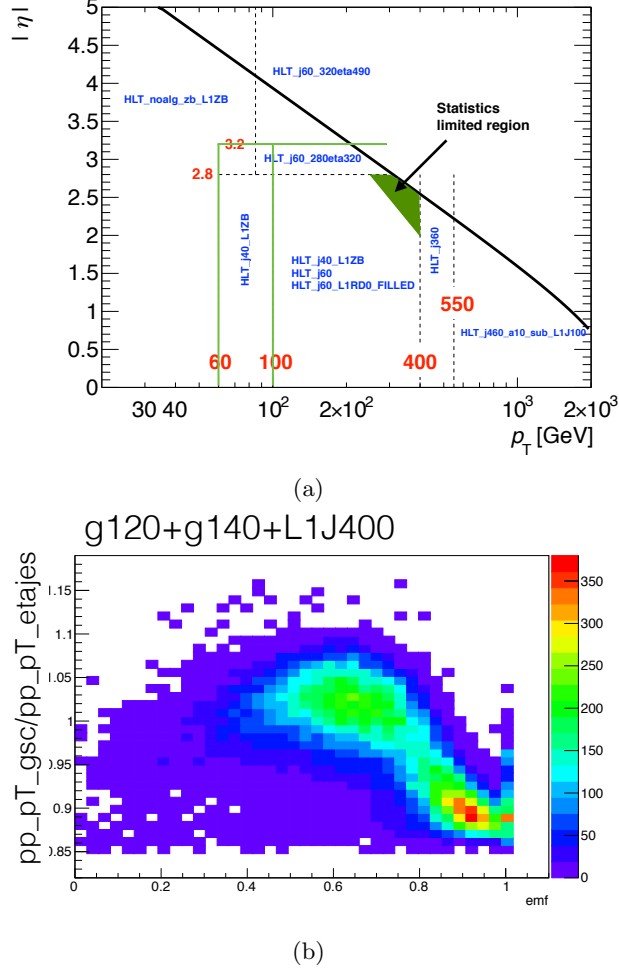


Figure 3.1: The jet selection criteria in data based on different triggers. (a) $p_T - \eta$ phase space for different trigger regions used in the ZeroBias and express streams ??The effect of the GSC calibration, as a function of the electromagnetic fraction (emf) of the jet. The peak at high emf is indicative of photons

Events in data were selected based on the trigger $\eta - \phi$ map given in Fig. 3.1. The HLT_j40_L1ZB, HLT_j60, and the HLT_j60_L1RD0_FILLED triggers were extended out to $|\eta| < 3.2$.

Furthermore, events firing the HLT_j360 trigger were vetoed if they also fired the HLT_noalg_L1J400, HLT_g120_loose, or the HLT_g140_loose. This was done to ensure that the jets entering the study were not in the wide turn on region of the aforementioned triggers. This also helped exclude photons (as can be seen in 3.1(b)).

MC events were filtered based on pileup. The MC generation settings included an average of combined 2015-2016 pileup profiles [17]. This can be seen in the top plot of Fig. 3.2, where the μ distribution in MC has a very wide spread, whereas the data (purely 2015) is localized around a central value. Events with $7 < \mu < 18$ were selected, and the jet p_T in MC was weighted with the ratio $\mu_{\text{Data}}/\mu_{\text{MC}}$ (in addition to the eventweight present in JZXW MC samples).

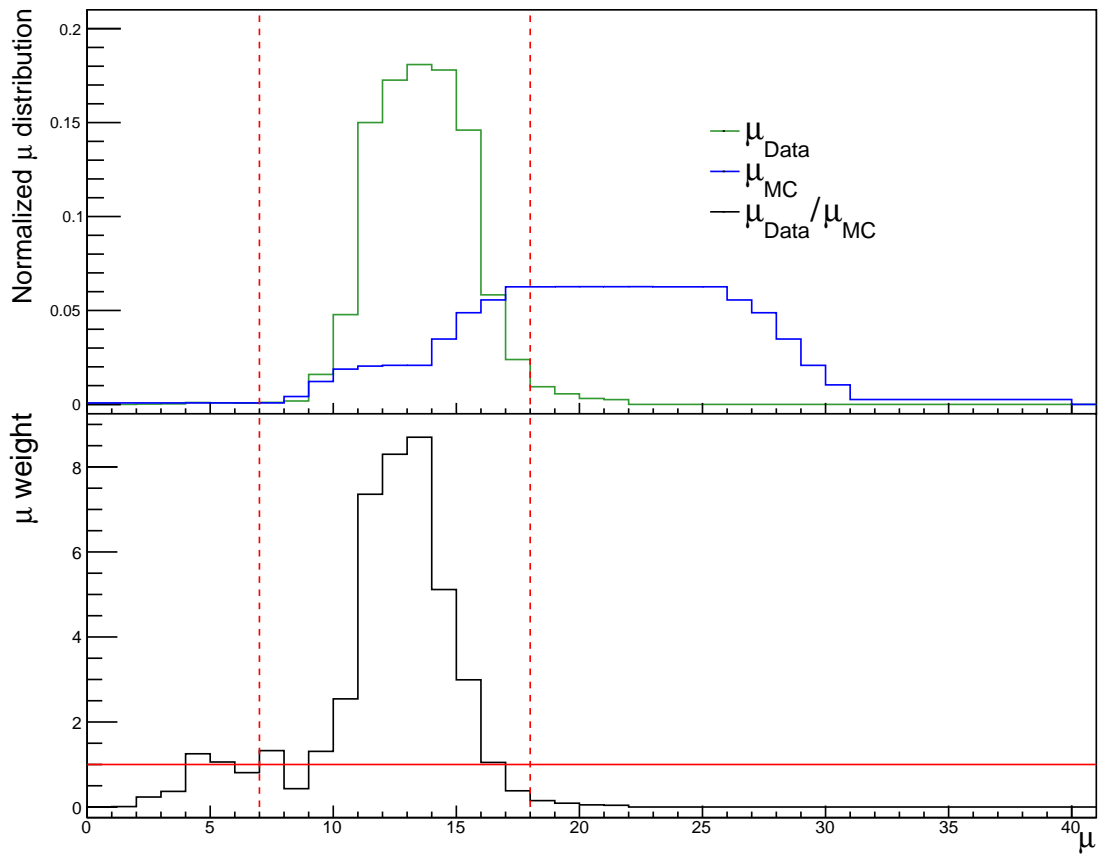


Figure 3.2: The top plot shows the normalized μ distribution in data and MC. The bottom plot is a ratio of the two quantities. The jet selection criteria in MC is based on the pileup conditions. Events with $7 < \mu < 18$ were selected.

Other standard cuts included jet cleaning (*LooseBad* cut level with the option *doUgly* set to *TRUE*) and applying a GRL data15_13TeV.periodAllYear_DetStatus-v75-repro20-01_DQDefects-00-02-02_PHYS_Standard GRL_All_Good_25ns.xml)

The HI, EMTopo, and Truth jets were also isolated and matched to each other (and to truth in MC) with the criteria given in Tables 3.2 and 3.3. The isolation p_T cut choice was dictated by the minimum p_T with which the HI and EMTopo jets are reconstructed (5 GeV for HI, 10 GeV for EMTopo). An investigation showed that for isolation p_T cuts below 20 GeV, there was a large difference (upto at least a factor of 2) in the number of EMTopo jets matched to truth jets, compared to HI jets matched to truth jets. The cross calibration factors were evaluated for jets with $30 < p_T < 1000$ GeV.

Table 3.2: Isolation criteria used in the evaluation of the nominal cross calibration factors

Jet Collection	Radius cut	p_T cut [GeV]
AntiKt4EMTopo	1.0	20.0
AntiKt4HI	1.0	20.0
Truth (in MC)	0.6	20.0

Table 3.3: Matching criteria used in the evaluation of the nominal cross calibration factors

Jet Collections	Radius cut
AntiKt4EMTopo + Truth	0.2
AntiKt4HI + Truth	0.3
AntiKt4(EMTopo+HI)	0.4

3.3 Procedure

The results presented here were performed using the ATLAS detector and calorimeter systems [5]. Jets with a radius of $R = 0.4$ were reconstructed using the antikt algorithm. The specifics of this procedure as applied to reconstruct the standard EMTopo jets and the HI jets are described in detail in [10] and [12] respectively. A brief summary is given below.

The EMTopo jets reconstruction involves using topological clusters of energy deposits in the calorimeter (calorimeter description in [5]). The antikt algorithm [18], as implemented in the FastJet software package [19] is applied to these clusters, to reconstruct EMTopo jets with a $R = 0.4$. The background in these jets, coming from the pile-up, is reduced by applying a p_T and jet area dependent subtraction [20]. The jets are then calibrated using a energy and η dependent calibration factor, derived from MC studies. The EMTopo jets for this study were calibrated up to MC based EtaJES, as described in [21].

The HI jet reconstruction also uses the anti- k_T algorithm, but the inputs are $\Delta\eta \times \Delta\phi = 0.1 \times \frac{\pi}{32}$ logical towers, deriving from the energy deposited in calorimeter cells. A fundamental difference between the reconstruction algorithms is how the underlying event (UE) is dealt with. The UE subtraction procedure involves the UE average transverse energy density (ρ), and the magnitude (ν_2) and phase (Ψ_2) of the elliptic modulation from flow. The subtraction applied to each cell within the jet is given as:

$$E_T^{\text{subtr}} = E_T^{\text{cell}} - \rho(\eta^{\text{cell}}, \phi^{\text{cell}}) A^{\text{cell}} \{1 + 2\nu_2 \cos[2(\phi - \Psi_2)]\} \quad (3.1)$$

where η^{cell} and ϕ^{cell} are the cell coordinates, and A^{cell} is the cell area in $\eta - \phi$ space. E_T^{subtr} and E_T^{cell} are the cell energies before and after subtraction [22]. The average UE transverse energy density is estimated from the cell transverse energies, whereas Ψ_2 is determined from the FCal.

$$\rho \equiv \left\langle \frac{E_T^{\text{cell}}}{A^{\text{cell}}} \right\rangle \quad (3.2)$$

$$\Psi_2 = \frac{1}{2} \tan^{-1} \frac{\sum E_T^{\text{cell}} \sin 2\phi^{\text{cell}}}{\sum E_T^{\text{cell}} \cos 2\phi^{\text{cell}}} \quad (3.3)$$

$$\nu_2 = \frac{\sum E_T^{\text{cell}} \cos 2(\phi^{\text{cell}} - \Psi_2)}{\sum E_T^{\text{cell}}} \quad (3.4)$$

The subtracted energy is seen to be independent of the jet E_T

A summary of the differences between the EMTopo and HI jet reconstruction methods is given in Table 3.4.

Table 3.4: A summary of the differences between the EMTopo and HI jet reconstruction algorithm. Adapted from [22].

	EMTopo	HI
Inputs	Topological clusters	Calorimeter towers
Subtraction	Median p_T density	Average local energy density

The heavy ion jets were calibrated (upto *EtaJES*) using the procedure given in [23], and the EMTopo jets were calibrated upto GSC (i.e. *JetArea_Residual-Origin_EtaJES_GSC*) using the ICHEP recommendations [21]. This was done so that the cross calibration factors could be applied as a correction on top of the insitu correction. This allowed changing the insitu correction, without re-deriving the cross-calibration factors.

A ratio of the EMTopo and HI jets, selected as described in Section 3.2 was taken in both data and MC. The relative response and resolution in data and MC is shown in Fig. 3.3 and 3.4. The distributions were calculated in the following $|\eta|$ bins: 0 - 0.3, 0.3 - 0.8, 0.8 - 1.2, 1.2 - 2.1, 2.1 - 2.8, 2.8 - 3.6, 3.6 - 4.4.

The cross calibration factors, obtained by taking a ratio of the above relative response plots, were fit to a

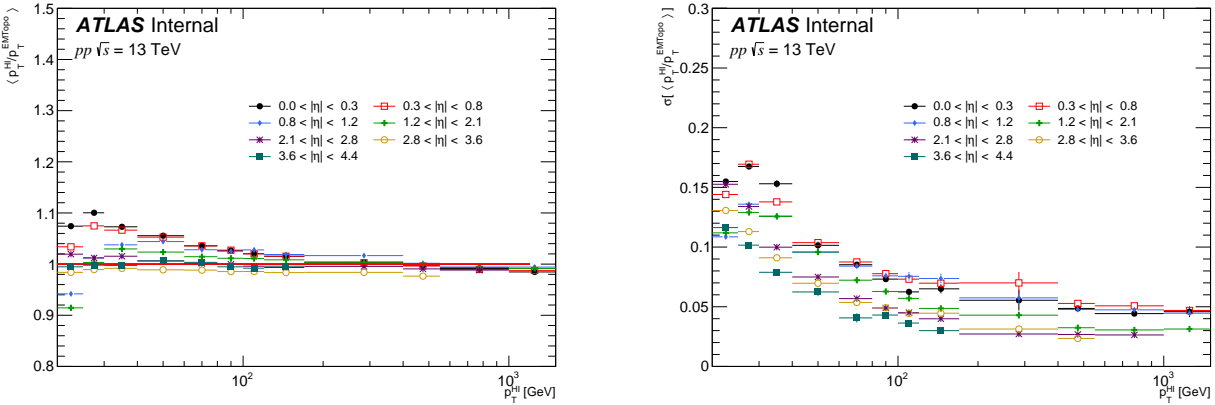


Figure 3.3: The relative response (left) and relative resolution (right) in data, as a function of the HI jet p_T

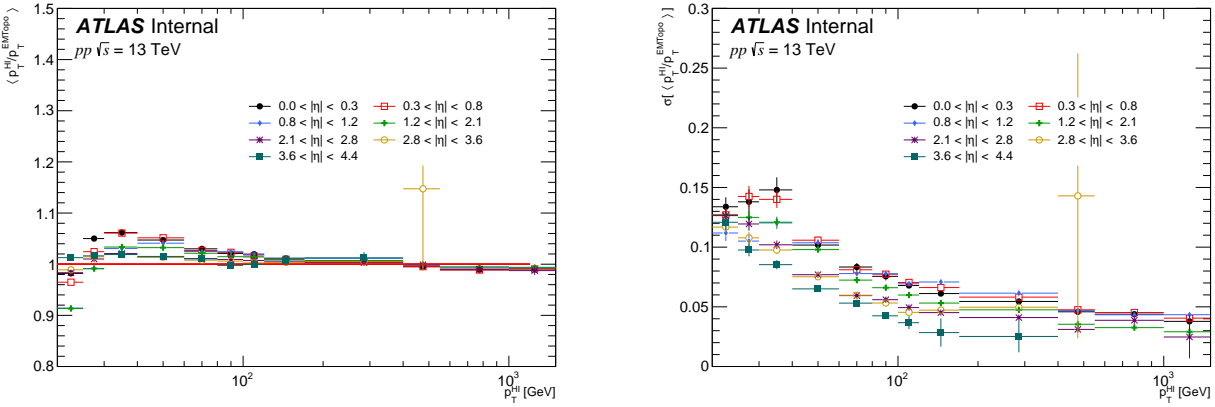


Figure 3.4: The relative response (left) and relative resolution (right) in MC, as a function of the HI jet p_T

polynomial in $\log [c_0 + c_1 \log(x) + c_2 (\log(x))^2]$ and are shown in Fig. 3.5. A ratio of the data to the fits is shown in Fig. ??.

3.4 Uncertainties

3.4.1 Cross calibration factor uncertainties

The statistical uncertainties come from the fits (using TVirtualFitter), whereas the systematics come from changing the parameters of the jet isolation criteria. These are summarized in Table 3.5. Having a moderate nominal p_T cut on the isolation ensured that fluctuations in the HI reconstructed jets did not veto good jets. The p_T cut was also determined by the minimum p_T reconstructed by the reconstruction algorithms. The range of fits from this parametrization are shown in Fig. 3.6. The systematical uncertainties, evaluated as

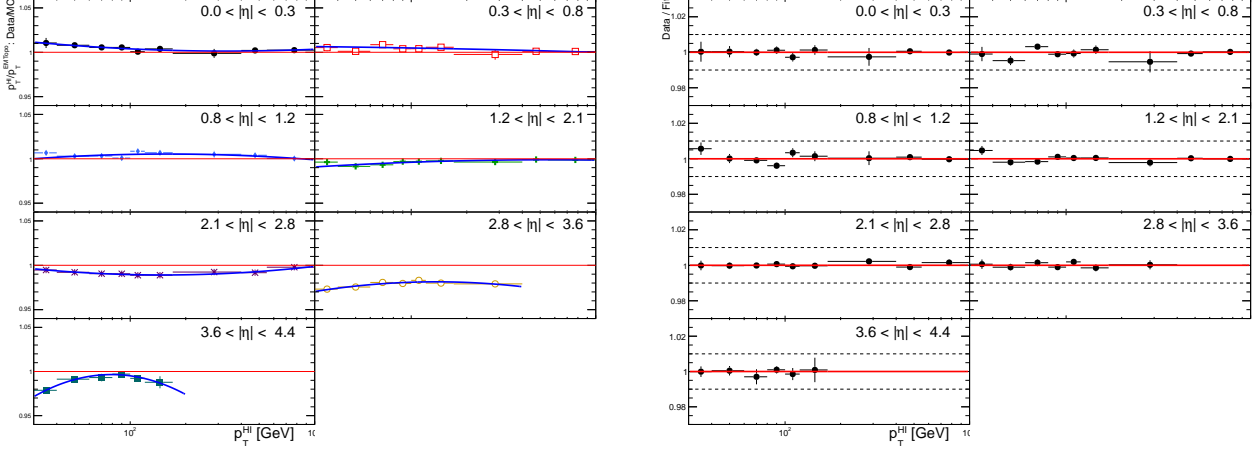


Figure 3.5: The cross calibration factors, obtained from taking a ratio of the relative response in data and MC. A ratio of the data to the fit is given on the right

the maximum absolute difference between the nominal fit and any other iteration, are show in in Fig. 3.7.

Table 3.5: The isolation and matching parameters were varied to get the systematics. See Fig. 3.6

	Nominal		Iteration 1		Iteration 2		Iteration 3		Iteration 4	
Isolation	R	p_T [GeV]	R	p_T [GeV]	R	p_T [GeV]	R	p_T [GeV]	R	p_T [GeV]
AntiKt4EMTopo	1.0	20.0	1.0	16.0	1.0	18.0	1.0	25.0	1.0	30.0
AntiKt4HI	1.0	20.0	1.0	16.0	1.0	18.0	1.0	25.0	1.0	30.0
Truth	0.6	20.0	0.6	16.0	1.0	18.0	0.6	25.0	1.0	30.0

3.4.2 Uncertainties on HI JER

The uncertainties on the heavy ion jet energy resolution ($\delta\sigma_{\text{HI}}$) can be shown to be given by:

$$\delta\sigma_{\text{HI}} = \frac{\delta R_{\text{HI}}}{2\sigma_{\text{HI}}} \quad (3.5)$$

where $R_{\text{HI}} = \sigma_{\text{HI}}^2$. We also can also derive (see A for derivation):

$$\delta^2 R_{\text{HI}} = \lambda^4 \delta^2 R_{\text{EMTopo}} + \delta^2 B \quad (3.6)$$

$$\delta R_{\text{EMTopo}} = 2\sigma_{\text{EMTopo}} \delta\sigma_{\text{EMTopo}} \quad (3.7)$$

$$\lambda = \frac{\text{Cov}(\Delta p_T^{\text{EMTopo}}|_{\text{noGSC}}, \Delta p_T^{\text{HI}})}{\text{Cov}(\Delta p_T^{\text{EMTopo}}|_{\text{GSC}}, \Delta p_T^{\text{HI}})} \quad (3.8)$$

$$\delta B = \sigma(p_T^{\text{HI}}/p_T^{\text{EMTopo}})_{\text{data}} - \sigma(p_T^{\text{HI}}/p_T^{\text{EMTopo}})_{\text{MC}} \quad (3.9)$$

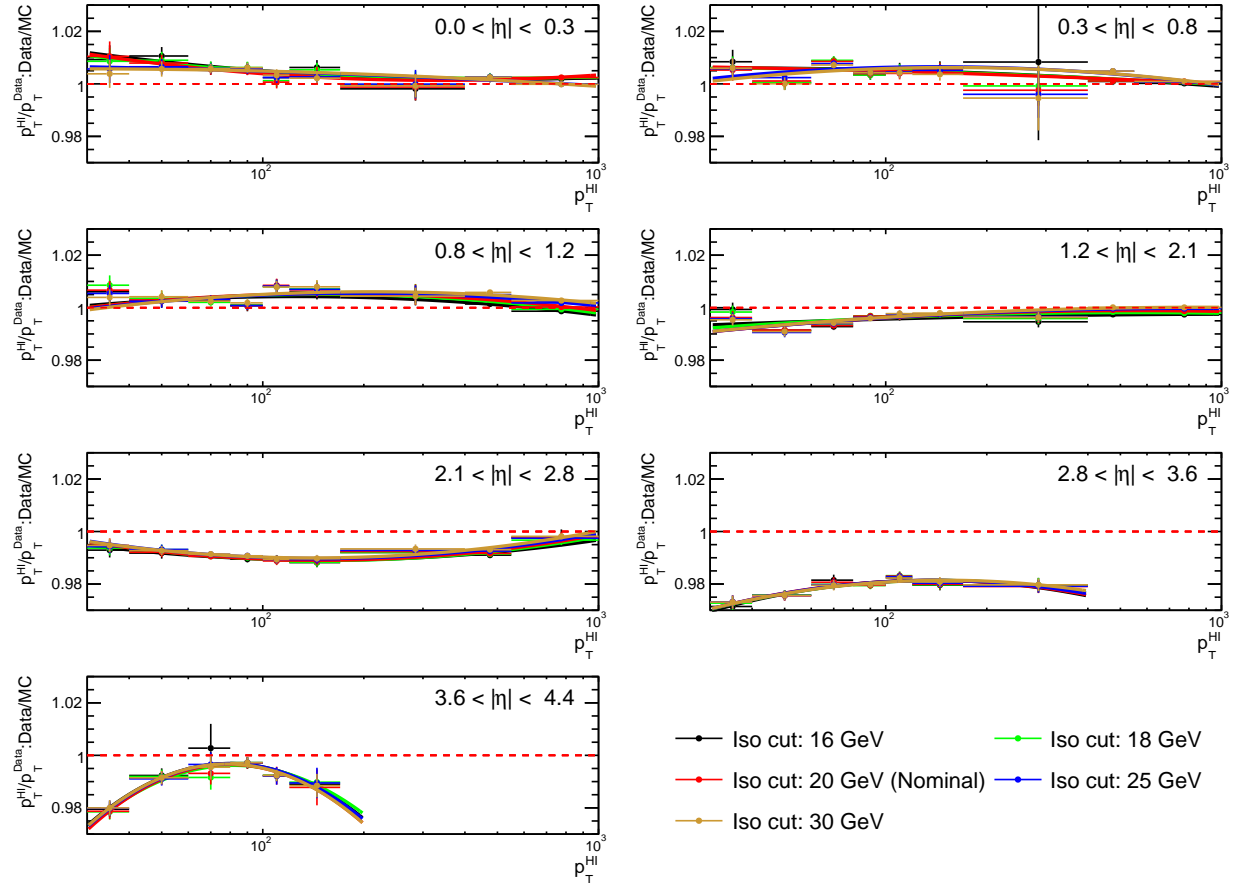


Figure 3.6: The fits to the cross calibration factors, with different isolation/matching cuts, as specified in Table 3.5.

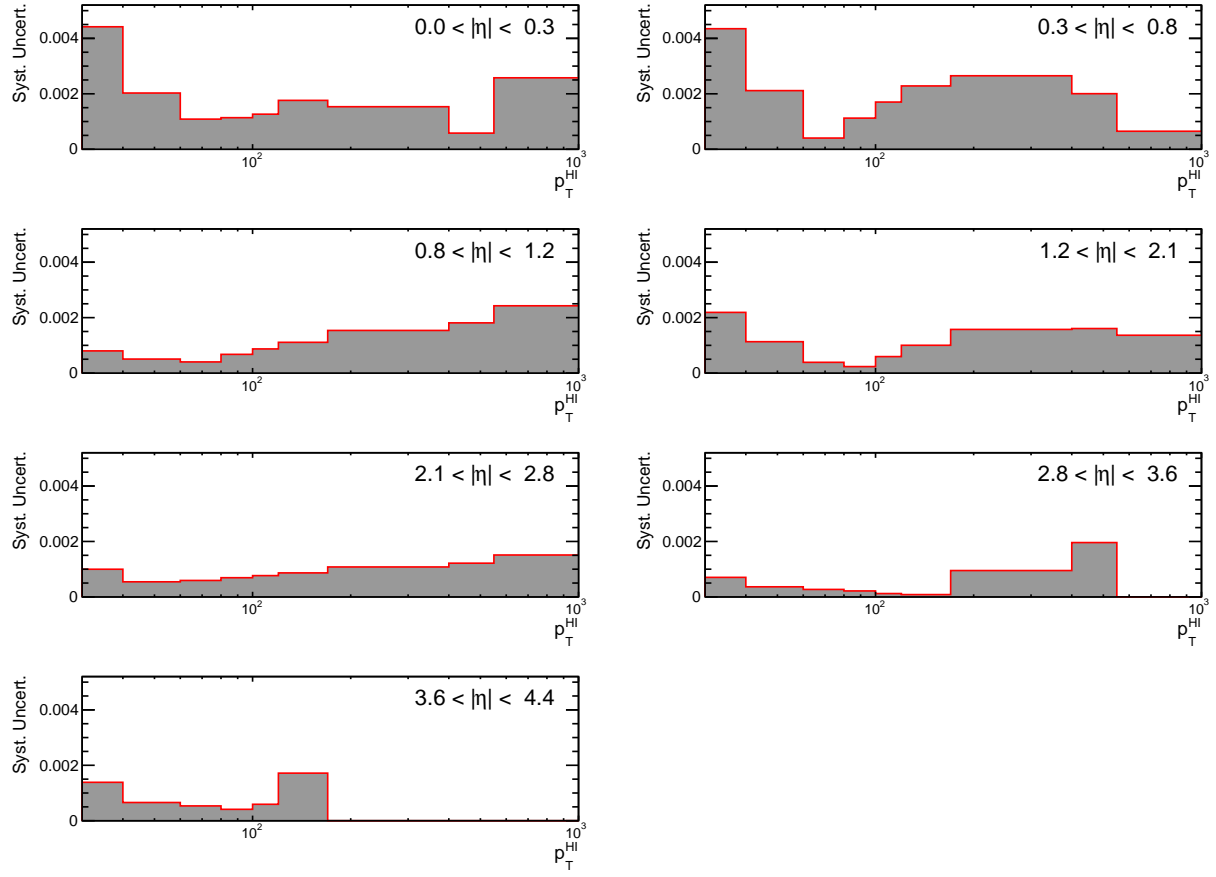


Figure 3.7: The systematic uncertainty, equal to maximum difference between the nominal fit and the fits from varying the parameters (as summarized in Table 3.5).

σ_{EMTopo} and $\delta\sigma_{\text{EMTopo}}$ were evaluated using the JER tool [24], whereas σ_{HI} was measured in the data (shown in Fig 3.8. λ was determined using $\Delta p_T^{\text{EMTopo}} = p_T^{\text{EMTopo}} - p_T^{\text{Truth}}$ and $\Delta p_T^{\text{HI}} = p_T^{\text{HI}} - p_T^{\text{Truth}}$ evaluated with and without the GSC calibration.

Fluctuations in σ_{EMTopo} and σ_{HI} were removed by fitting to the form

$$a + (b/p_T) + (c/p_T)^2 \quad (3.10)$$

These are shown in Fig. 3.9. The $\Delta p_T^{\text{EMTopo}}$ vs. Δp_T^{HI} for with and without the GSC can be seen in Fig. 3.10 and Fig. 3.11 respectively. The λ distribution can be seen in Fig. 3.12. A comparison between $\delta\sigma_{\text{EMTopo}}$ and $\delta\sigma_{\text{HI}}$ can be seen in Fig. 3.13. The ratio $\delta\sigma_{\text{EMTopo}}/\delta\sigma_{\text{HI}}$ can be expressed as below:

$$\frac{\delta\sigma_{\text{HI}}}{\delta\sigma_{\text{EMTopo}}} = \frac{\delta R_{\text{HI}}}{\delta R_{\text{EMTopo}}} \frac{\sigma_{\text{EMTopo}}}{\sigma_{\text{HI}}} \quad (3.11)$$

This factorization (plotted in Fit. 3.14) showed that the large differences between $\delta\sigma_{\text{EMTopo}}$ and $\delta\sigma_{\text{HI}}$ were coming from the differences in the uncertainties, as opposed to differences in the actual resolutions themselves. The same quantity, $\delta\sigma_{\text{EMTopo}}/\delta\sigma_{\text{HI}}$, as calculated in Run I is shown in Fig. 3.15 [8].

3.5 Qualification Task Conclusion

The cross calibration factors, along with its systematic and statistical uncertainties were derived in different η regions, as a function of p_T^{HI} , and are shown in Fig. 3.16. The factors themselves are the level of 1%, and do not show much variation with p_T . Furthermore, the uncertainties are primarily statistical in nature.

A p_T dependent uncertainty on the HI JER was also derived, and can be seen in Fig. 3.13.

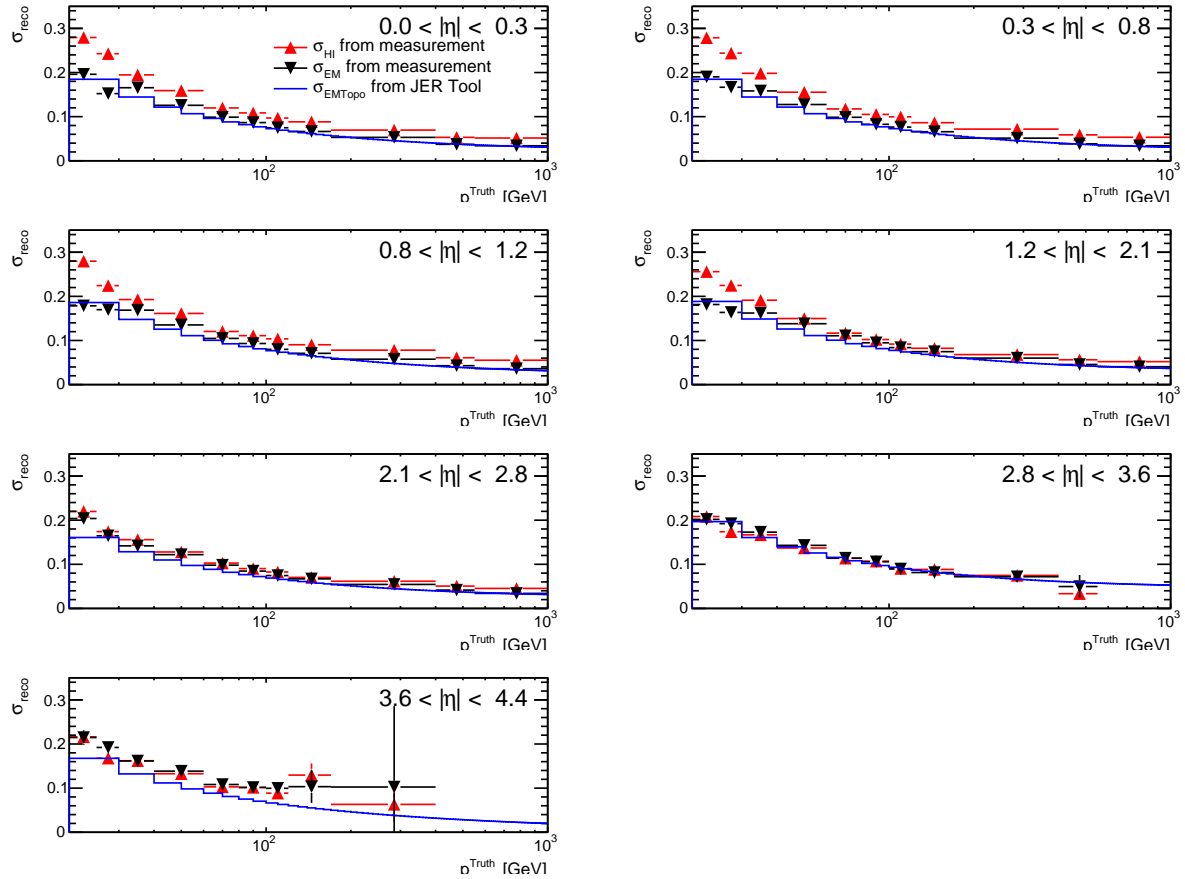


Figure 3.8: A comparison of the JER of EMTopo and HI jets from the datasets, as well as from the JER Tool.

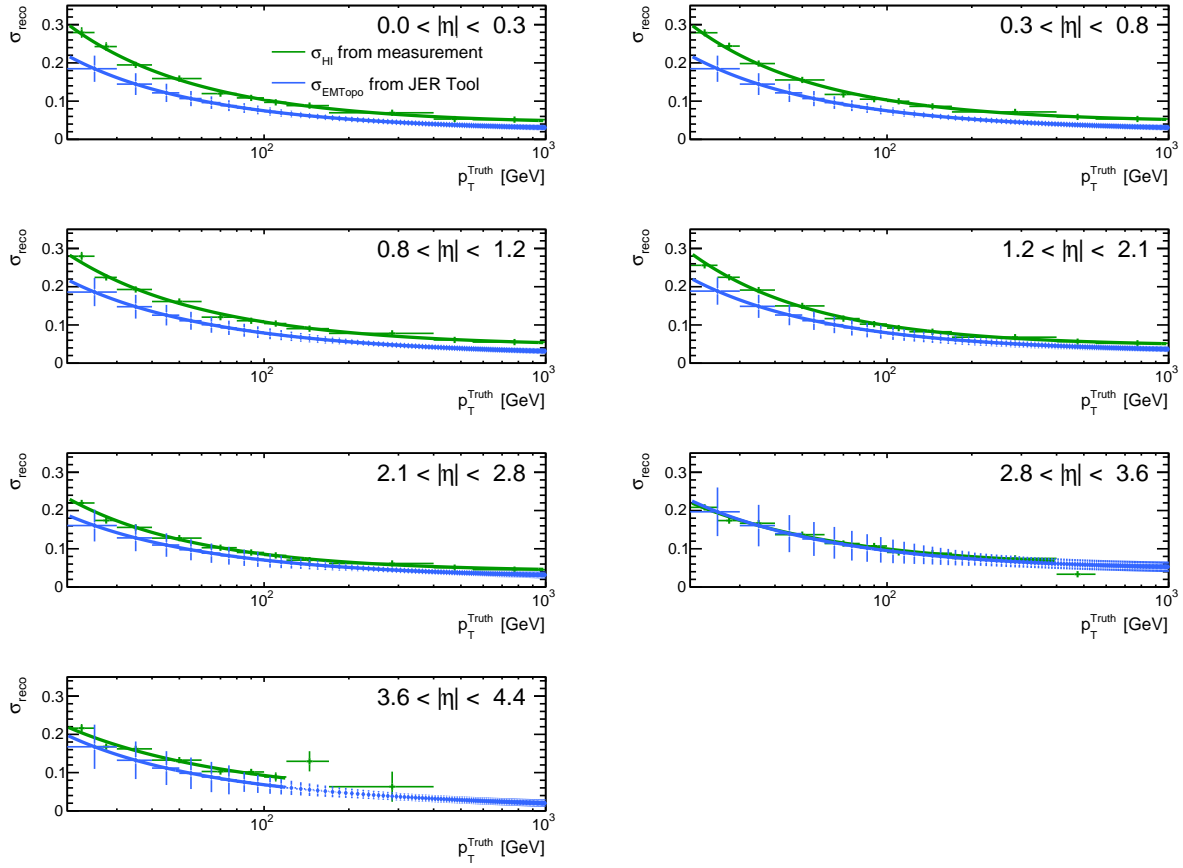


Figure 3.9: The JER for HI and EMTopo jets fit to Eq. 3.10

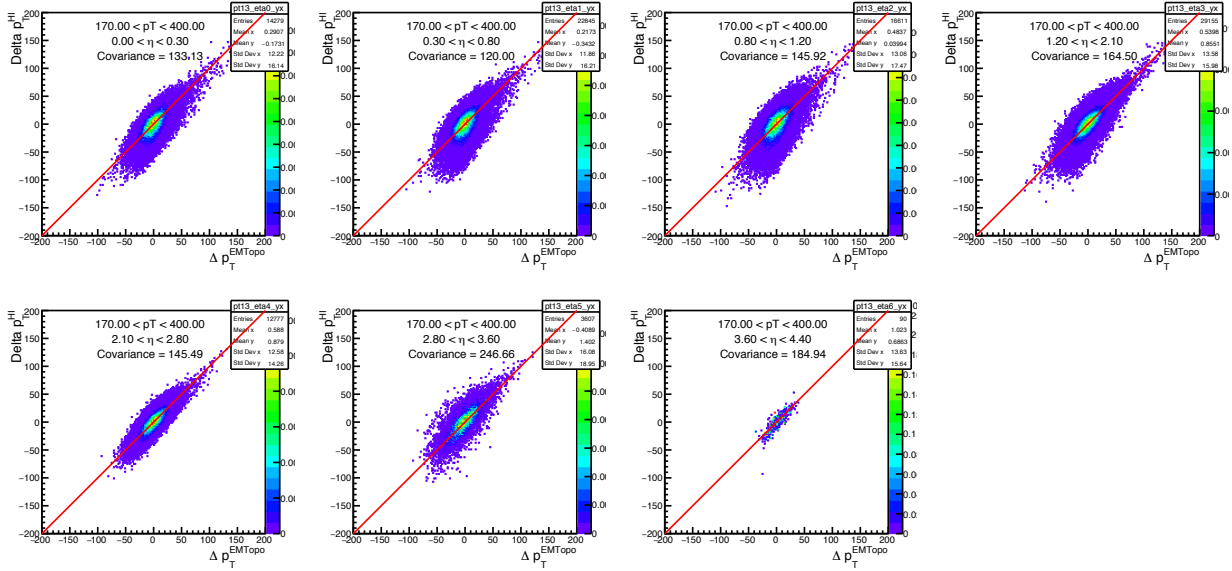


Figure 3.10: The $\Delta p_T^{\text{EMTopo}}$ vs. Δp_T^{HI} distribution in all η bins, for $170 < p_T^{\text{Truth}} < 400$ GeV, with the GSC calibration applied to the EMTopo jets.

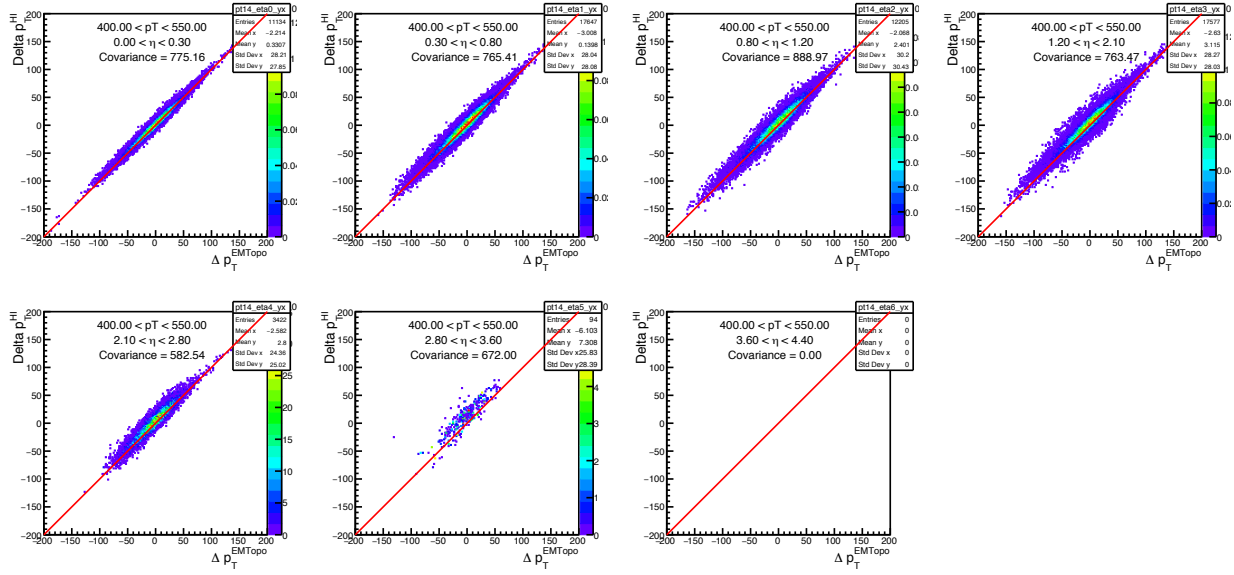


Figure 3.11: The $\Delta p_T^{\text{EMTopo}}$ vs. Δp_T^{HI} distribution in all η for $170 < p_T^{\text{Truth}} < 400$ GeV, with no GSC calibration applied to the EMTopo jets.

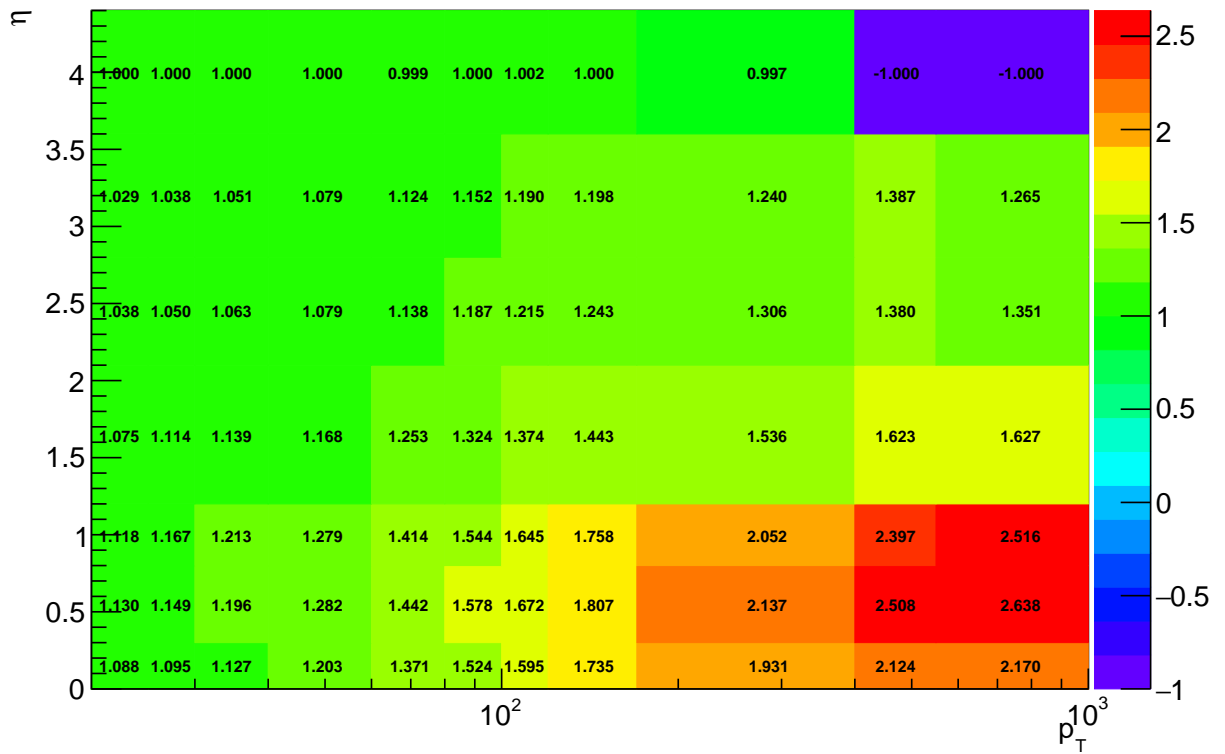


Figure 3.12: The distribution of λ as calculated in Eq. 3.8 in various bins of p_T and η .

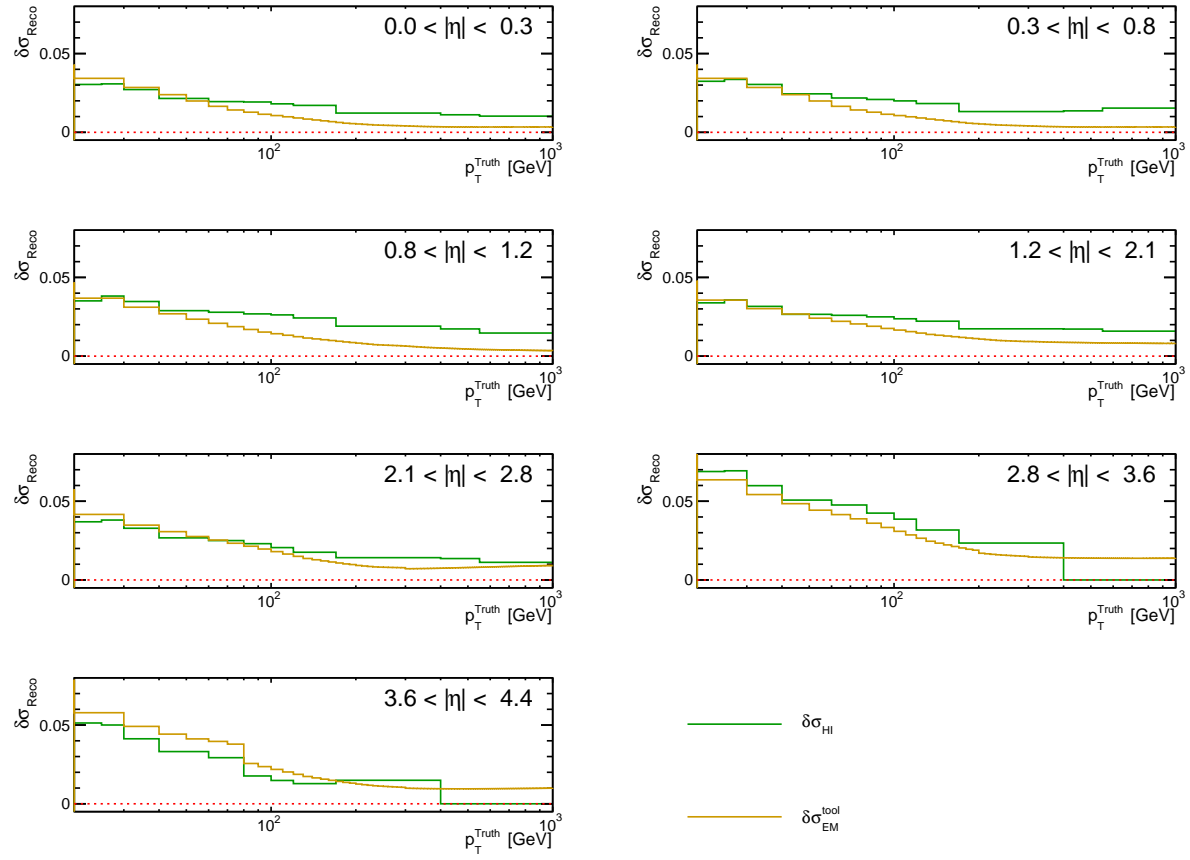


Figure 3.13: A comparison between $\delta\sigma_{\text{EMTopo}}$ and $\delta\sigma_{\text{HI}}$ in various η bins

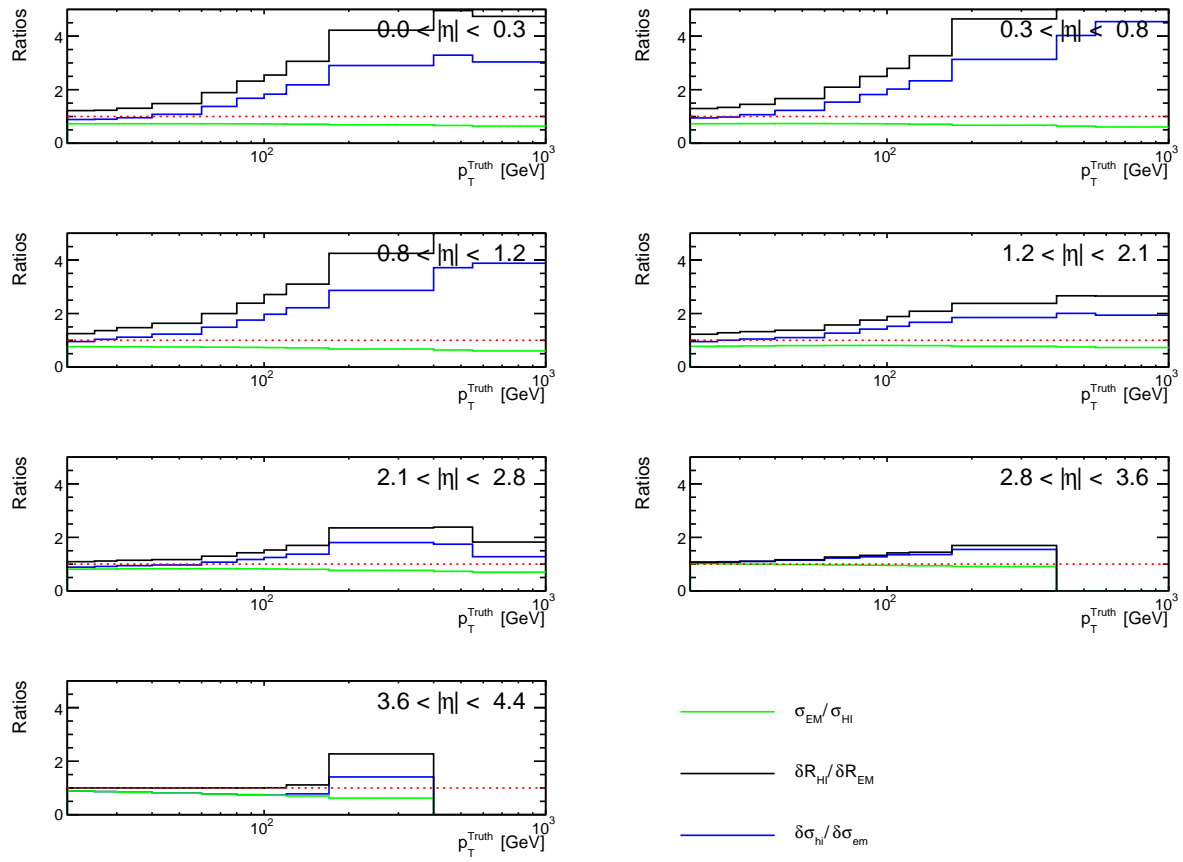


Figure 3.14: Factorizing the ratio $\delta\sigma_{\text{EMTopo}}/\delta\sigma_{\text{HI}}$ shows that the dominant effect is from the uncertainties themselves (as opposed to a difference in the resolutions)

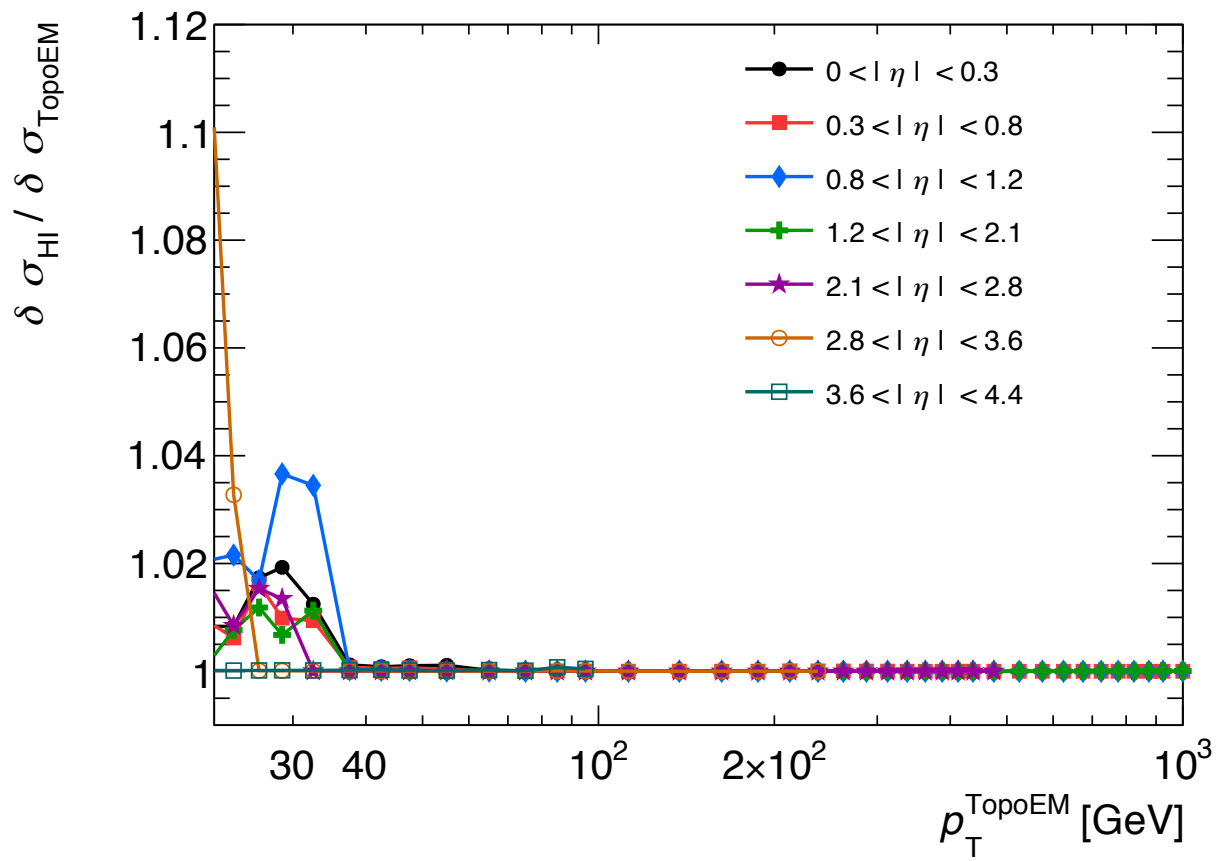


Figure 3.15: The ratio $\delta\sigma_{\text{EMTopo}} / \delta\sigma_{\text{HI}}$ as evaluated in Run I [8]

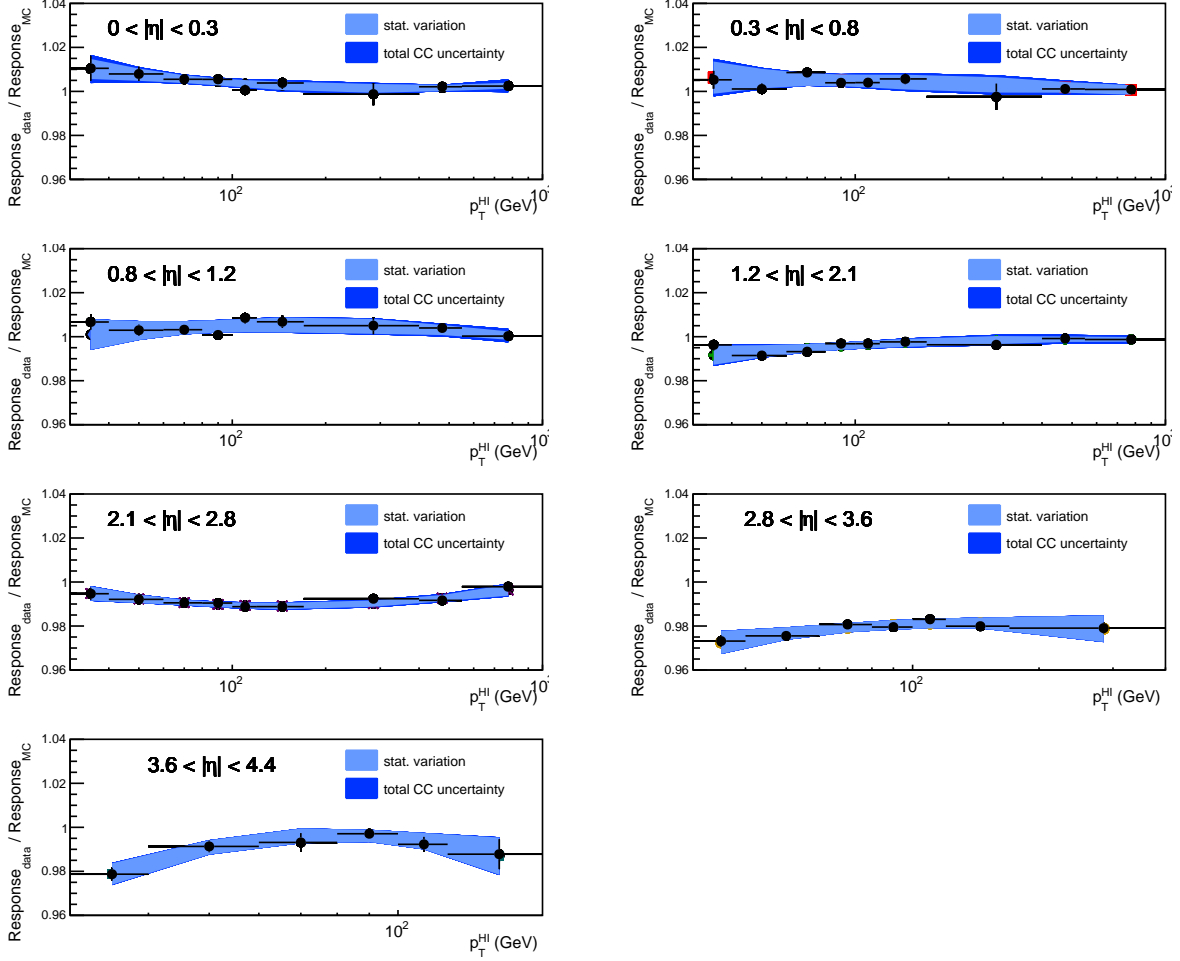


Figure 3.16: The cross calibration factors in different η regions, as a function of p_T^{HI} , along with their uncertainties.

Chapter 4

Measurement of Angular Correlations Between Tracks And Jets

This section discusses the main analysis undertaken by the author. This chapter is divided into the sections detailed below:

- 4.1 defines and discusses the quantity measured,
- 4.2 discusses the datasets used
- 4.3 describes the various event selection criteria
- 4.5 describes the cuts and corrections applied to the measured quantities
- 4.6 discusses the systematic uncertainties
- 4.7 describes the results
- 4.8 goes into a discussion of the results.

4.1 Definition of Measured Quantities

The main quantity of interest here is the charged particle p_T distribution in and around the jet as illustrated in Fig. 4.1. The measured quantity is defined as:

$$D(p_T, r) = \frac{1}{N_{\text{jet}}} \frac{1}{A} \frac{dn_{\text{ch}}(p_T, r)}{dp_T}, \quad (4.1)$$

where N_{jet} is the number of jets in consideration, $A = \pi(r_{\max}^2 - r_{\min}^2)$ is the area of an annulus around the jet with its inner and outer radii r_{\min} and r_{\max} . The angular distance from the jet axis is given by $r = \sqrt{\Delta\eta^2 + \Delta\phi^2}$ ¹, and $n_{\text{ch}}(p_T, r)$ is the number of charged particles with a given p_T within the annulus. The measurement is performed for the following successive intervals in r around the jet, forming the annuli with inner and outer radii r_{\min} and r_{\max} : 0.0, 0.05, 0.1, 0.15, 0.2, 0.25, 0.3, 0.4, 0.5, 0.6, 0.7, 0.8

¹ $\Delta\eta$ and $\Delta\phi$ are the distances between the jet axis and the charged particle position in pseudorapidity and azimuth

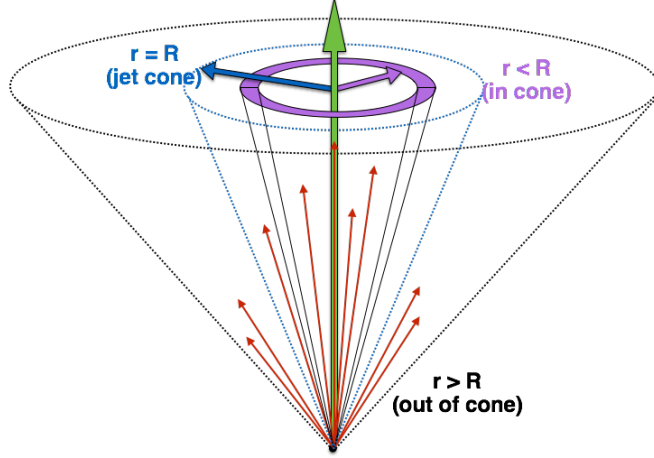


Figure 4.1: Illustration of the tracks in and around the jet.

The entire analysis flow of this measurement, along with the various cuts and corrections (discussed in Sec. 4.5) is shown in Fig:4.2 and briefly described in the following paragraph.

First, the measured charged particle yield, dn_{ch}^{meas}/dp_T^{ch} , within an annulus with radii r_{min} and r_{max} is evaluated as:

$$\frac{dn_{ch}^{meas}}{dp_T^{ch}} = \frac{1}{\epsilon(p_T^{ch}, \eta^{ch})} \frac{\Delta N_{ch}(p_T^{ch}, r)}{\Delta p_T^{ch}} \quad (4.2)$$

where $\Delta N_{ch}(p_T^{ch}, r)$ is the number of charged particles in a given p_T^{ch} range that passed the jet and track selection criteria, $r = (r_{min} + r_{max})/2$, and $\epsilon(p_T^{ch}, \eta^{ch})$ is the charged particles reconstruction efficiency correction, applied on a track-by-track basis. In Pb+Pb collisions, the measured distributions are affected by charged particles from the underlying event, and thus need to be subtracted out (see Sec. 4.5 for details):

$$\frac{dn_{ch}^{sub}}{dp_T^{ch}} = \frac{dn_{ch}^{meas}}{dp_T^{ch}} - \frac{dn_{ch}^{UE}}{dp_T^{ch}} \quad (4.3)$$

The final $D(p_T, r)$ distributions are then evaluated after unfolding and normalizing with respect to the unfolded number of jets, $N_{jet}^{unfolded}$, as well as the area A of the annulus at given distance r :

$$D(p_T, r) = \frac{1}{N_{jet}^{unfolded}} \frac{1}{A} \frac{dn_{ch}^{unfolded}}{dp_T^{ch}} \quad \text{where } A = \pi(r_{max}^2 - r_{min}^2) \quad (4.4)$$

The unfolding procedure is a combination of a two-dimensional Bayesian unfolding method in p_T^{jet} and p_T^{ch} , one-dimensional Bayesian unfolding method to correct jet spectra for the normalization and a one-dimensional bin-by-bin correction for the jet and track position resolution.

The analysis is performed differentially in p_T^{jet} , and centrality, with the jet p_T bin size growing logarithmically with p_T^{jet} to ensure good statistics in the full range of the measurement. This scheme was also used in

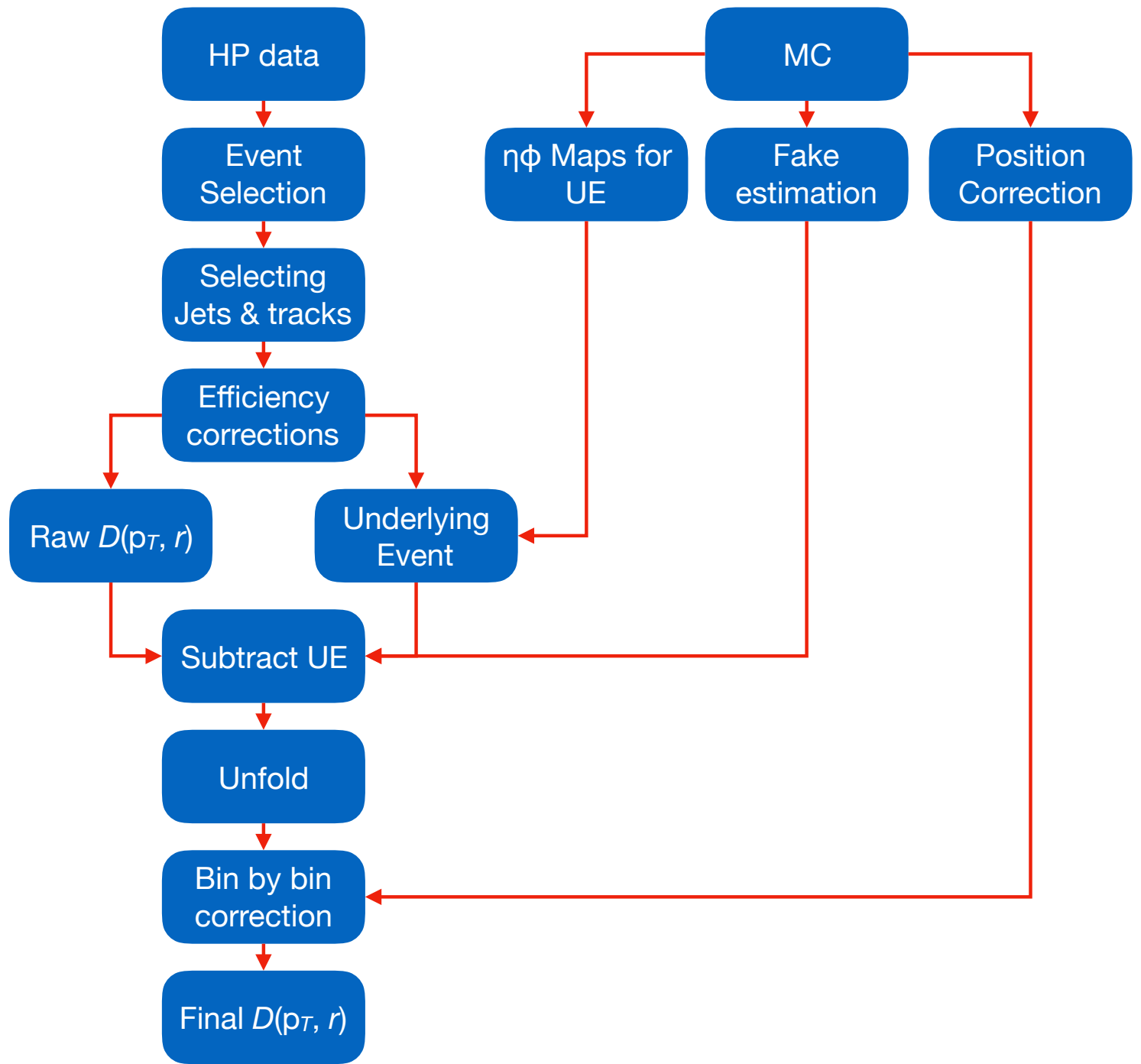


Figure 4.2: The diagram presents various corrections and cuts that are applied during the analysis.

other ATLAS jet measurements [25].

In order to quantify the differences between charged particle spectra in Pb+Pb and pp collisions, the ratios of the charged particle spectra in Pb+Pb collisions to those in pp collisions are also reported:

$$R_{D(p_T, r)} \equiv \frac{D(p_T, r)_{\text{Pb+Pb}}}{D(p_T, r)_{pp}} \quad (4.5)$$

4.2 Input Data

4.2.1 Data samples

This analysis used the original processing of pp (reconstruction tag 7744) and Pb+Pb (reconstruction tag 7874) collisions at $\sqrt{s_{\text{NN}}} = 5.02$ TeV recorded in 2015 with a total integrated luminosity of 25 pb^{-1} and 0.49 nb^{-1} respectively. The run numbers for each set are given below:

- 2015 pp data: 286282, 286361, 286364, 286367, 286411, 286474
- 2015 Pb+Pb data: 286711, 286717, 286748, 286767, 286834, 286854, 286908, 286990, 287038, 287044, 287068, 287222, 287224, 287259, 287270, 287281, 287321, 287330, 287334, 287378, 287380, 287382, 287560, 287594, 287632, 287706, 287728, 287827, 287843, 287866, 287924, 287931

Various hard probe triggers (high- p_T jets, muons, electrons, and photons) are group into a Hard Probe (HP) stream and Main stream in Pb+Pb and pp data taking periods respectively. The pp data samples from the Main stream used in this analysis are listed in Table 4.1. For the analysis of the Pb+Pb data the officially produced HION7 derivation samples from the Hard Probe stream are used. The list of datasets together with detailed description of HION7 derivation setup can be found in Ref. [26]. Additionally to the jet triggered data sample, Pb+Pb collisions recorded by Minimum-Bias (MB) triggers grouped in to MB stream are utilized in this analysis. The following MB data sets are used: `data15_hi.0028*.physics_MinBias.merge.AOD.r7874_p2580`.

description	data set names	# runs
		6
2015 pp , hard probes	<code>data15_5TeV.periodK.physics_Main.PhysCont.AOD.repro20_v03</code>	5
2015 pp , hard probes	<code>data15_5TeV.periodVdM.physics_Main.PhysCont.AOD.repro20_v03</code>	1

Table 4.1: Summary of data samples used in the pp analysis.

4.2.2 Trigger Selection

To maintain efficiency for events containing hard probes specific jet triggers are used. First, events are identified at the L1 trigger by various L1 triggers. These L1 “seeds” are passed to the High Level Trigger (HLT) where jet trigger algorithm with various thresholds on p_T of the jet was used for the final selection.

Low p_T HLT jet triggers in pp collisions were seeded by L1 MB random trigger (L1RD0) or L1 triggers requiring different thresholds on total energy in the calorimeter (L1TE). High p_T HLT jet triggers in pp collisions were seeded by different L1 jet triggers performing a simple sliding window algorithm to find jet candidates (L1J). In Pb+Pb collisions, L1 total energy triggers were used to seed all HLT jet trigger chains.

We analyze jets selected from jet triggers in the region of jet p_T for which the triggers are fully efficient² for jets. Since the analysis only used jets above 100 GeV, the appropriate triggers were selected. For pp , only the HLT_j85 trigger (fully efficient above 88.8 GeV) was used. For Pb+Pb the only trigger used was the HLT_j75_ion_L1TE50 (fully efficient above 91 GeV).

The performance of the jet trigger in 2015 is described in [27] and the trigger efficiency is presented in Figure 4.3 (pp collisions) and Figure 4.4 (Pb+Pb collisions). The trigger efficiency for two low thresholds is evaluated using MB events. The low p_T thresholds are used as the reference to evaluate the performance at higher p_T . The efficiency for the higher threshold is bootstrapped from lower thresholds. The broader turn-on of the jet trigger in Pb+Pb compared to pp collisions is caused by significant differences between the HI jet trigger reconstruction algorithm used at the time of the data taking and the current version of the offline reconstruction software.

In addition to the jet triggered sample, a MB triggered sample defined by a logical OR of the total energy trigger with a threshold of 50 GeV and the ZDC coincidence trigger was used as part of the MC overlay procedure

The event fraction as a function of run number for both the hard probes stream and the minimum bias overlay stream in Pb+Pb is shown in Fig. 4.5

The run dependence of the underlying event (a core part of this measurement) was tested by dividing the data and MC into three periods with approximately equal number of events in each period: 286711 – 287259, 287270 – 287632, and 287706 – 287931. The underlying event determined for each period compared to the nominal underlying event evaluated for the entire dataset is shown in Fig. 4.6, and it can be seen that the UE is stable throughout the data taking period.

²Efficiency is better than 99%

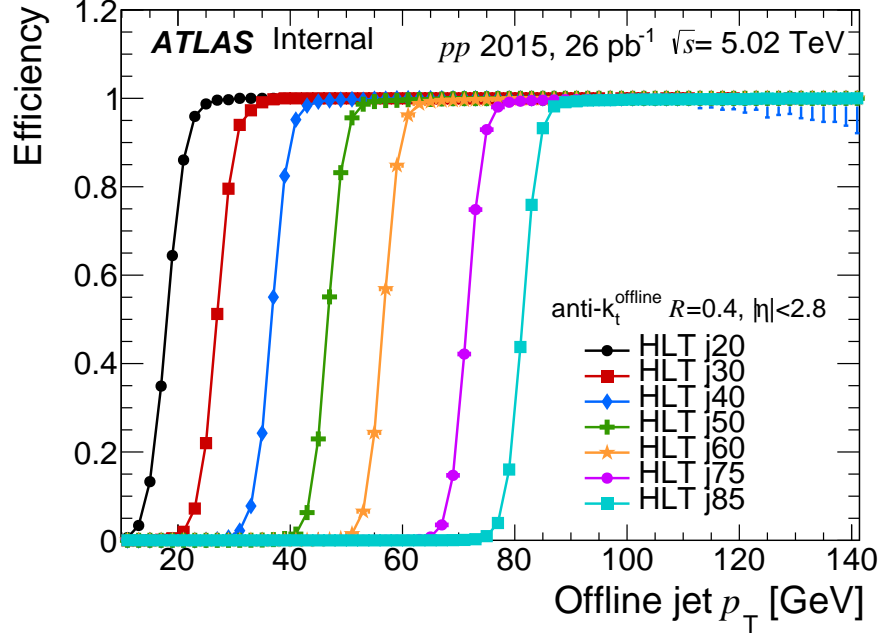


Figure 4.3: Trigger efficiencies for $R=0.4$ offline jets for seven HLT jet triggers in pp collisions at 5.02 TeV.

4.2.3 Monte Carlo Samples

This analysis also utilizes MC15 PYTHIA8 pp jet events at $\sqrt{s} = 5.02$ TeV with the A14 ATLAS tune and the NNPDF23LO pdfs [28]. The definitions of the pp MC samples can be found in Tab. 4.2. The Pb+Pb MC uses POWHEG+PYTHIA8 events that are overlayed on top of MB Pb+Pb collisions. These samples are listed in Tab. 4.3.

JZ	Dataset Name
2	<code>mc15_5TeV.420022.PowhegPythia8EvtGen_A14_NNPDF23LO_CT10ME_jetjet_JZ2R04.merge.DAOD_HION7.e4109_s2860_r7792_r7676_p3442</code>
3	<code>mc15_5TeV.420023.PowhegPythia8EvtGen_A14_NNPDF23LO_CT10ME_jetjet_JZ3R04.merge.DAOD_HION7.e5067_s2860_r7792_r7676_p3442</code>
4	<code>mc15_5TeV.420024.PowhegPythia8EvtGen_A14_NNPDF23LO_CT10ME_jetjet_JZ4R04.merge.DAOD_HION7.e5067_s2860_r7792_r7676_p3442</code>

J	$R = 0.4$ p_T^{truth} [GeV]	σ [nb] $\times \epsilon$	#events
2	60–160	$(6.4 \times 10^5) \times (4.27 \times 10^{-3})$	5.8 M
3	160–400	$(4.7 \times 10^3) \times (5.28 \times 10^{-3})$	5.9 M
4	400–800	$(2.7 \times 10^1) \times (4.58 \times 10^{-3})$	5.8 M

Table 4.2: 5.02 TeV PYTHIA8 pp MC samples.

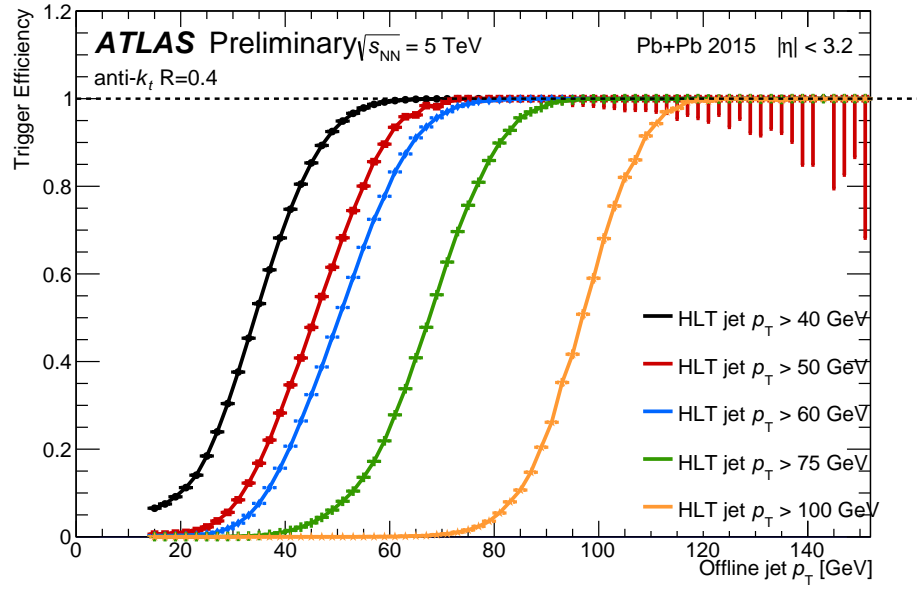


Figure 4.4: Jet trigger efficiency in centrality inclusive (0-80%) Pb+Pb collisions for R=0.4 offline jets.

JZ	Dataset Name
2	mc15_5TeV.420022.PowhegPythia8EvtGen_A14_NNPDF23LO_CT10ME_jetjet _JZ2R04.merge.DAOD_HION7.e4109_d1421_r8238_r8052_p3196
3	mc15_5TeV.420023.PowhegPythia8EvtGen_A14_NNPDF23LO_CT10ME_jetjet _JZ3R04.merge.DAOD_HION7.e4109_d1421_r8238_r8052_p3196
4	mc15_5TeV.420024.PowhegPythia8EvtGen_A14_NNPDF23LO_CT10ME_jetjet _JZ4R04.merge.DAOD_HION7.e4109_d1421_r8238_r8052_p3196

Table 4.3: Pb+Pb data overlay datasets used here.

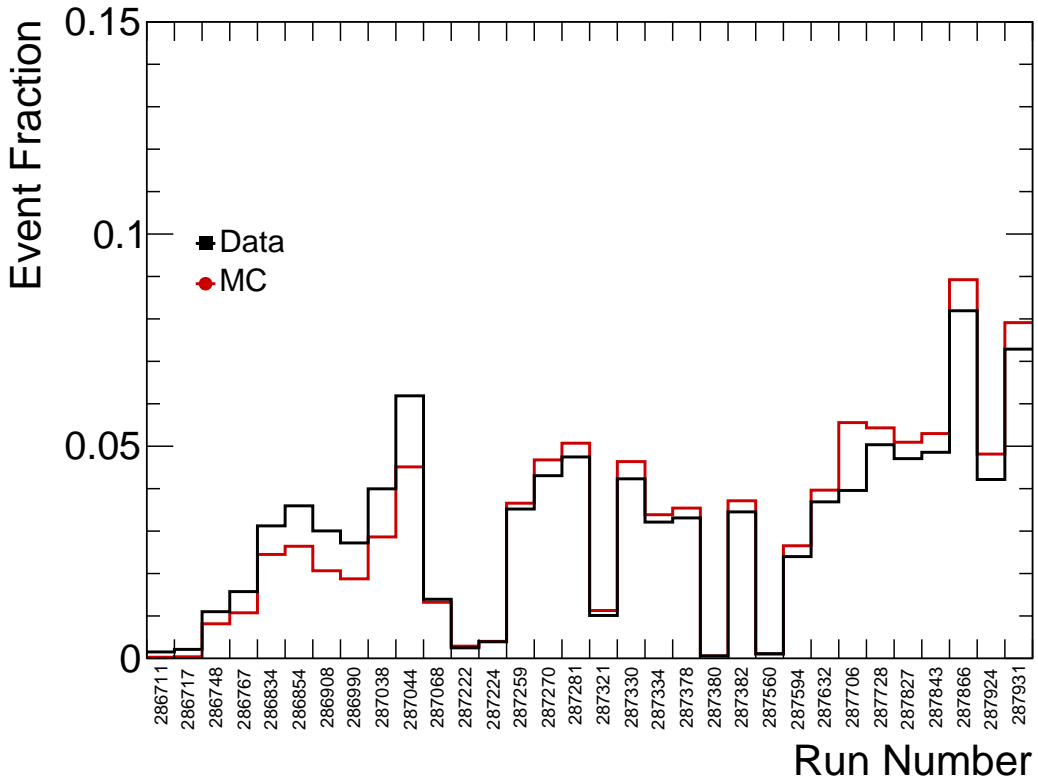


Figure 4.5: Event fraction as a function of runs for Hard Probes and the Minimum Bias Overlay Streams in Pb+Pb collisions.

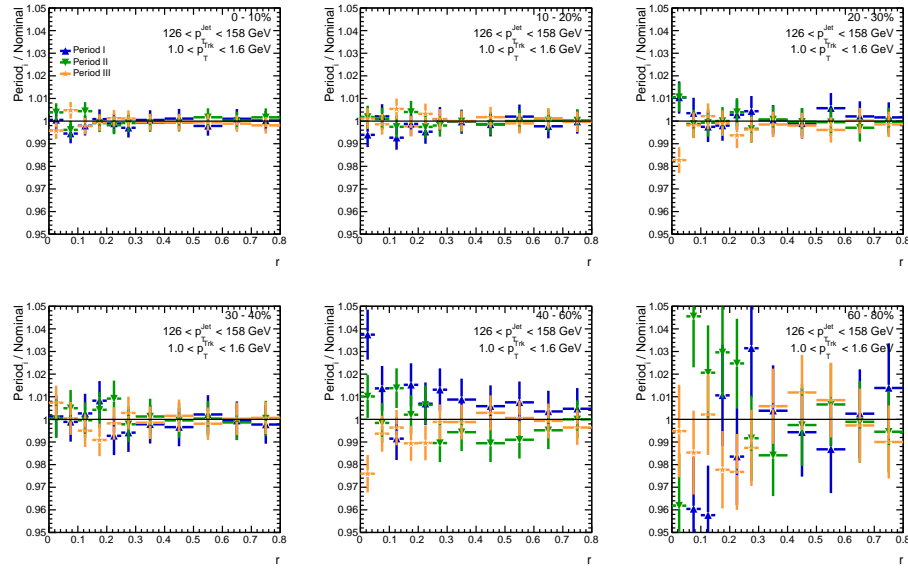


Figure 4.6: Stability of the underlying event for three different periods of the data taking. The different curves indicate the ratio of the underlying event in each period of data taking to the underlying event determined in the entire dataset.

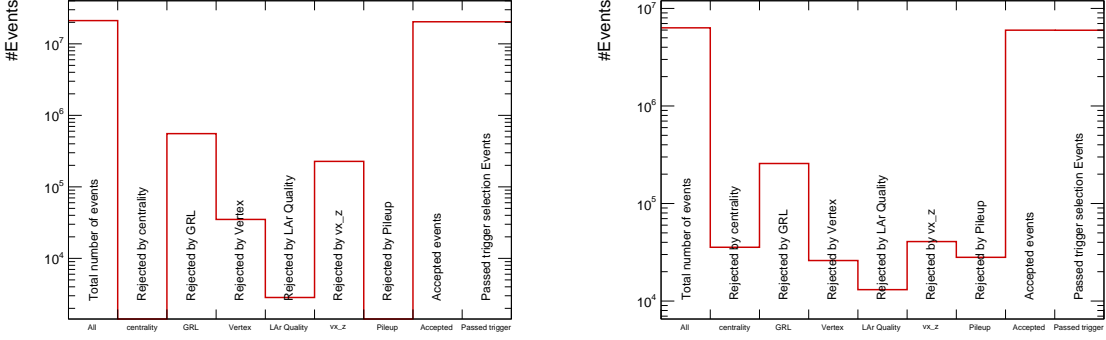


Figure 4.7: The number of 2015 pp (left) and $Pb+Pb$ (right) events used and rejected by various event quality cuts.

4.3 Event Selection

The standard ATLAS event quality requirements were applied for the event selection both for the pp and $Pb+Pb$ event selection.

- All the sub-detector systems were required to be fully functional: all the data were required to pass the official good run list:

```
data15_5TeV.periodAllYear_DetStatus-v75-repro20-01_DQDefects-00-02-02_PHYS_HeavyIonP_All_Good.xml (2015 pp)
data15_5TeV.periodVdM_DetStatus-v75-repro20-01_DQDefects-00-02-02_PHYS_HeavyIonP_All_Good.xml (2015, VdM pp)
data15_hi.periodAllYear_DetStatus-v75-repro20-01_DQDefects-00-02-02_PHYS_HeavyIonP_All_Good.xml (2015 Pb+Pb).
```

- All events are required to have a good reconstructed primary vertex.
- The primary vertex must be within 150 mm from the center of ATLAS detector, as a fiducial tracking region.
- Additional event cleaning to remove additional detector imperfections as described here [29] is used.
- In $Pb+Pb$ collisions the pileup contribution is removed using the `HIAAnalysisTools` [30].

Figures 4.7 presents the total number of pp and $Pb+Pb$ events, respectively, entering the analysis together with rejection power of various event quality cuts. A slightly higher fraction of empty events without primary vertex is observed in pp collisions. Some of these events are rejected by multiple cuts. ‘‘Rejection by centrality’’ indicates the number of event in HP stream that is outside the 0-80% centrality bin.

4.3.1 Centrality Selection

The centrality of the collision is a degree of the overlap of two colliding nuclei that can be quantified by the impact parameter that is the distance between the centers of the two nuclei. If they collide head on the collision is central, if they just graze each other we speak about peripheral collisions. We cannot measure the impact parameter to determine the centrality, but we can measure the overall event activity in the collision, characterized e.g. by the sum of E_T measured in FCal calorimeters on both sites. Central collisions have large E_T deposits in the FCal, peripheral have small E_T deposits.

In this analysis, The ΣE_T^{FCal} distribution is divided into percentiles of the total inelastic cross section for Pb+Pb collisions. The first percentile, 0 – 10%, represents the 10% of collisions with the largest event activity, smallest impact parameter. The last percentile, 90 – 100%, represents the 10% of collisions where there is the smallest event activity and largest impact parameter. Seven centrality classes have been used: 0-10%, 10-20%, 20-30%, 30-40%, 40-60%, 60-80%. The most peripheral collisions 80-100%, are excluded due to the small number of jets. The centrality selections are documented in Ref. [31]. The Pb+Pb MC is re-weighted in the way that it has the same centrality distribution as the jet triggered data sample.

4.4 Jet Reconstruction

For the measurement presented here, we use the jets reconstructed in the calorimeter using the anti- k_t algorithm [18] with $R = 0.4$. The underlying event (UE) contribution to jets is subtracted on an event by event basis at the cell level. The details on the jet reconstruction procedure and performance in heavy ion collisions have been described in [32], here we will only shortly summarize the main features of the heavy ion jet reconstruction.

In order to reconstruct jets in heavy ion collisions, a large background from the UE has to be subtracted from each jet. The UE subtraction procedure is done in several iterative steps. First an estimate of the UE average transverse energy density, $\rho_i(\eta)$, is evaluated for each calorimeter layer i in intervals of η of width $\Delta\eta = 0.1$ using all cells in each calorimeter layer, within a given η interval excluding those within $\Delta R < 0.4$ of “seed” jets. In the first subtraction step, the “seed” jets are defined to be jets reconstructed using the anti- k_t algorithm with $R = 0.2$ jets which have at least one tower (a tower is a 0.1x0.1 region of the calorimeter and the energy associated with it is the sum of the energies from all contributing calorimeter layers in that region) with $E_T > 3$ GeV and which have a ratio of the maximum to the mean tower associated with the jet of at least 4. The UE-subtracted cell energies were calculated according to:

$$E_{T,i}(\eta, \phi)^{\text{sub}} = E_{T,i}(\eta, \phi) - A_i \times \rho_i(\eta) \quad (4.6)$$

where $E_{T,i}$, η , ϕ , and A_i represent the E_T , η , ϕ , and area of the cell in the layer i . The $\rho_i(\eta)$ is the energy density per unit area in the layer i . The kinematics for $R = 0.2$ jets generated in this first subtraction step were calculated via a four-vector sum of all (assumed massless) cells contained within the jets using the E_T values obtained from Eq. 4.6.

The second subtraction step starts with the definition of a new set of seeds using a list of $R = 0.2$ calorimeter jets from the first subtraction step, each with $E_T > 4$ GeV. Using this new set of seeds, a new estimate of the UE, $\rho'_i(\eta)$, was calculated excluding cells within $\Delta R < 0.4$ of the new “seed” jets, where $\Delta R = \sqrt{(\eta_{\text{cell}} - \eta_{\text{jet}})^2 + (\phi_{\text{cell}} - \phi_{\text{jet}})^2}$.

The jet energy scale calibration is based on the numerical inversion method and provides calibration constants for all jet collections used in this study [23]. The final jet energy calibration using in-situ studies is applied in the offline analysis and it is described in Sec 4.5.1.

The jet reconstruction performance in 5.02 TeV pp collisions was evaluated using corresponding MC samples with a full detector simulation. The kinematics of the truth jets are reconstructed from primary

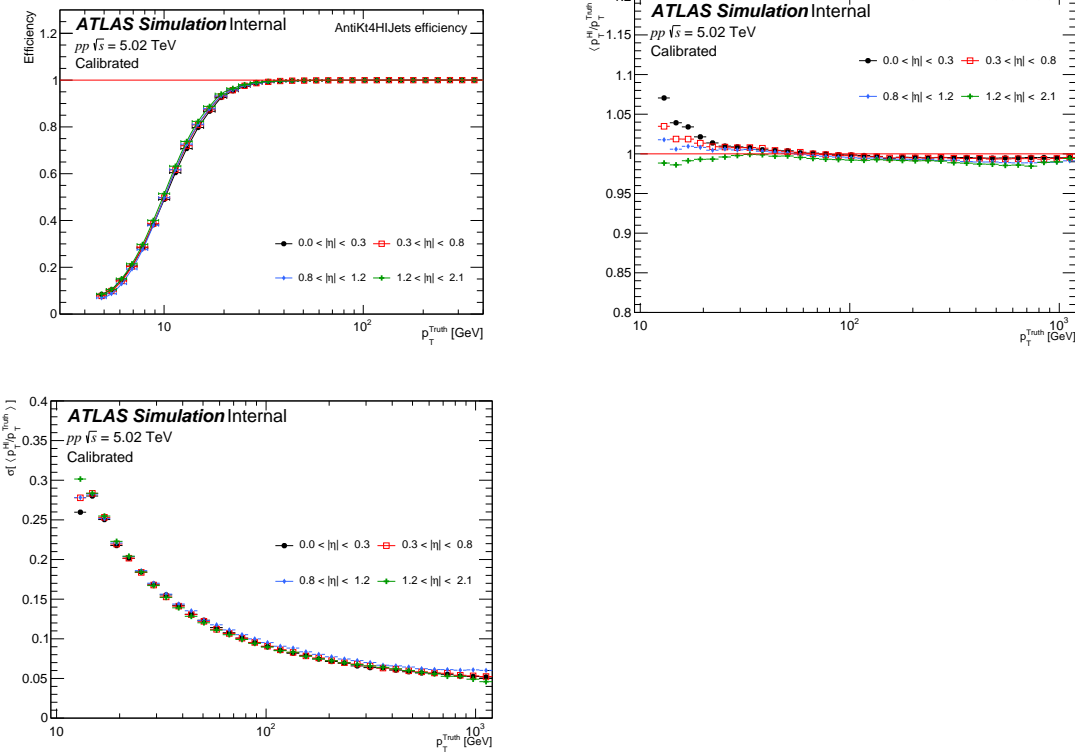


Figure 4.8: Top panels: Jet reconstruction efficiency in 5.02 TeV pp collisions (left) as a function of truth jet p_T and different η bins. Jet energy scale (JES) in 5.02 TeV pp collisions (right) as a function of truth jet p_T and different η bins. Bottom panels: Jet energy resolution (JER) in 5.02 pp collisions as a function of truth jet p_T and different η bins.

particles³ with the anti- k_t algorithm with radius parameter $R = 0.4$. The jet reconstruction efficiency, JES (in this case evaluated as $\langle (E_T^{\text{reco}}) \rangle / E_T^{\text{truth}}$), and JER for pp collisions is shown in Fig. 4.8 for $R = 0.4$ jet. For Pb+Pb collisions the JES is shown in Fig. 4.9 and the JER is shown in Figure 4.10. Further studies of the jet performance in the 2015 Pb+Pb data are found in Ref. [33]. Figures 4.11-4.12 present the jet angular resolution in η and ϕ as a function of jet p_T evaluated in six centrality classes. The angular resolution is improving with the increasing jet p_T and decreasing collision centrality. The angular resolution is found to be significantly better for smaller jets as expected since the smaller jets are less affected by the presence of the UE.

³Primary particles are defined as having a mean lifetime of $\tau > 0.3 \times 10^{-10}$ s, and are produced directly in pp interactions or from decays of particles with shorter lifetimes

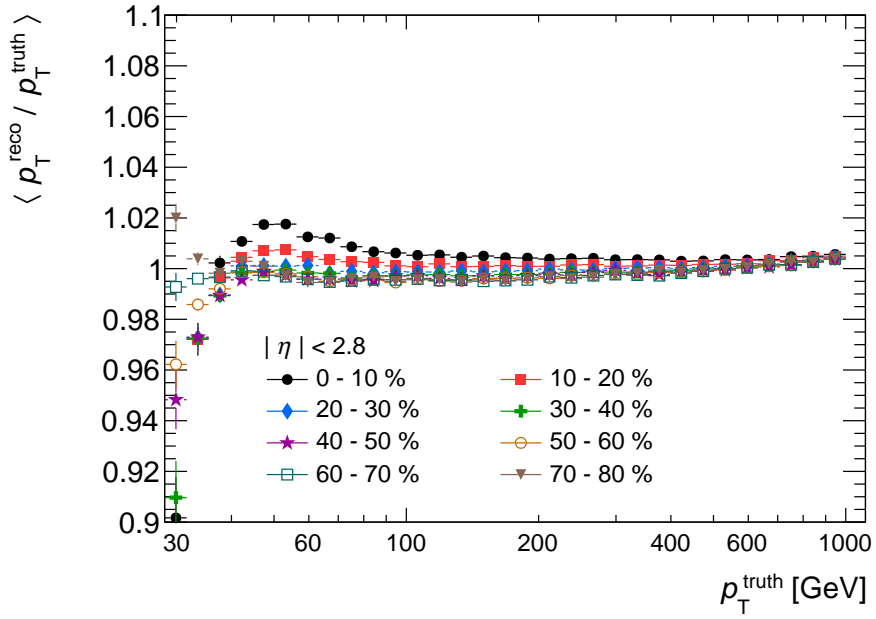


Figure 4.9: JES in Pb+Pb collisions for eight centrality selections. Plot is from Ref. [33].

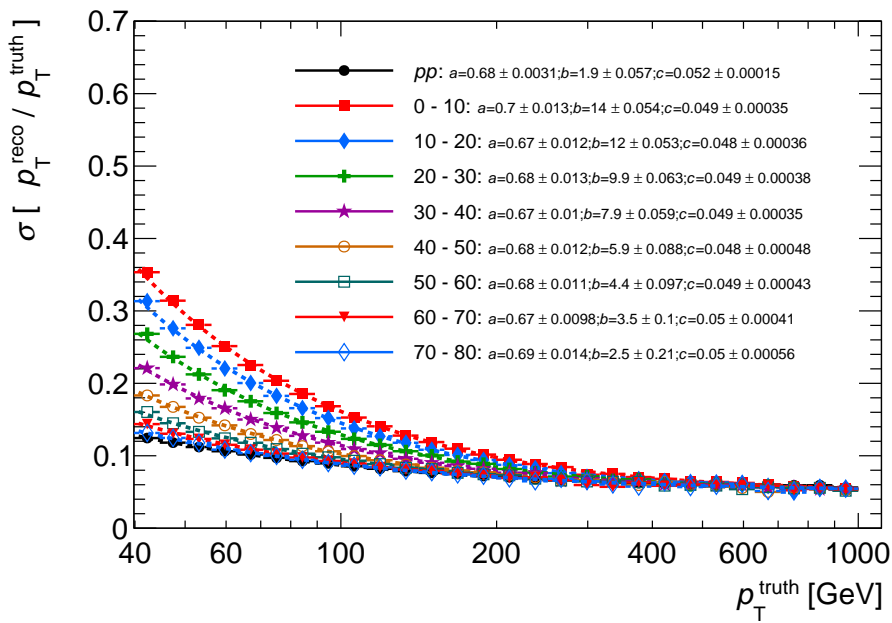


Figure 4.10: JER in Pb+Pb collisions for eight centrality selections. Plot is from Ref. [33]. The points are fit to the standard function that describes the calorimetric resolution.

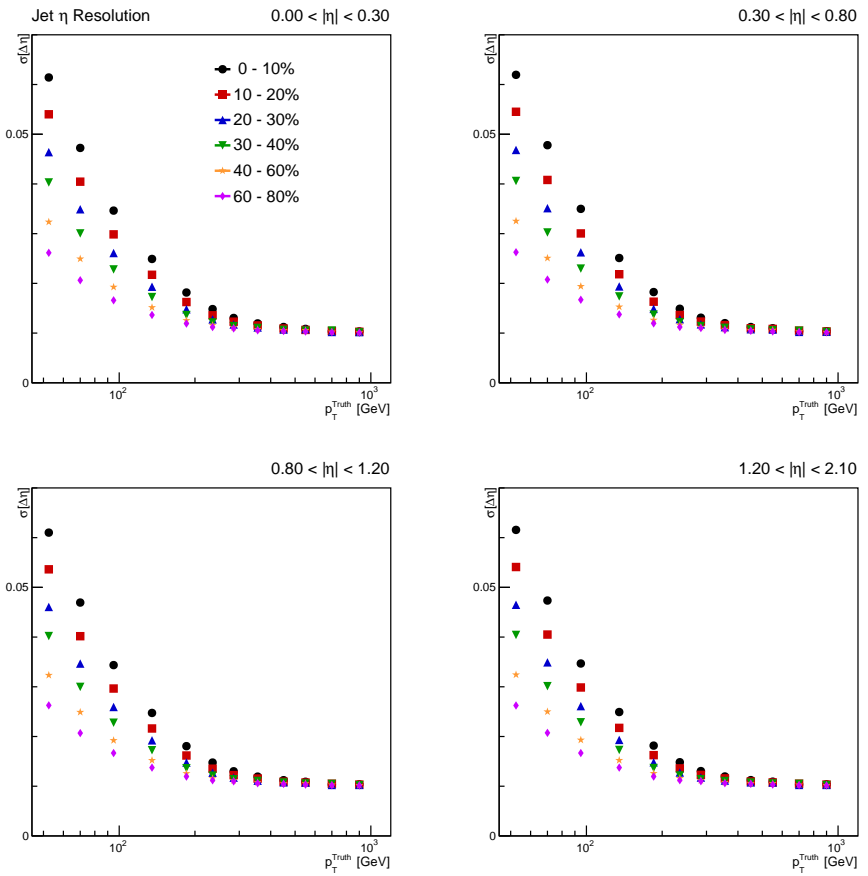


Figure 4.11: Jet angular resolution in η for $R = 0.4$ jets in Pb+Pb collisions as a function of jet p_T for six centrality selections.

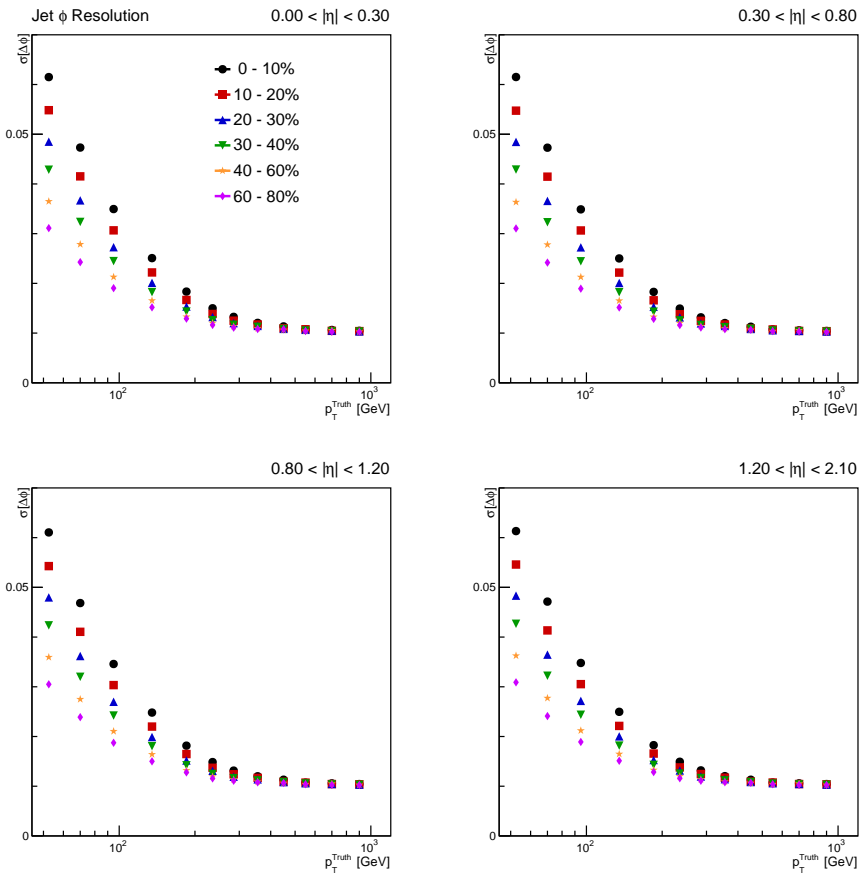


Figure 4.12: Jet angular resolution in ϕ for $R = 0.4$ jets in Pb+Pb collisions as a function of jet p_T for six centrality selections.

4.5 Basic Cuts and Corrections

A description of the analysis procedure to reconstruct the $D(p_T, r)$ distribution, along with the derivation and application of the various corrections is presented in the following sections. The analysis structure is illustrated by the diagram in Fig. 4.2 where each part of the analyses is described in a separate subsection and it can be summarized as follows:

- Jet selection and calibration
- Track selection
- Track momentum correction
- Fake rates
- Tracking efficiency
- Underlying event subtraction of tracks
- Unfolding

4.5.1 Jet Selection and final energy calibration

Since the Inner Detector (ID) covers the $|\eta| < 2.5$, the analysis can only be performed for jets within the pseudorapidity interval of $|\eta| < 1.7$ to have the entire $r = 0.8$ cone under investigation fully covered by the tracking detector. In both collision systems, jets are measured with p_T^{jet} between 126 GeV and 316 GeV in following four successive intervals: 126–158, 158–200, 200–251, and 251–316 GeV. This binning was motivated by the large fake rate below 100 GeV. An underflow bin was also needed for the unfolding procedure, and hence, the measurement starts at 126 GeV. This binning is also used in previous heavy ion jet measurements ([13]). Truth jets were associated with the nearest reconstructed jet using the matching of $\Delta R < 0.2$ for the performance study and to build response matrices for the unfolding procedure. The same ΔR matching criteria were employed in previous ATLAS HI jet analyses and are justified by a detailed performance study [34]. To prevent nearby jets from distorting the measurement of $D(p_T, r)$ distributions, jets are rejected if there is another jet with a higher p_T^{jet} than the considered jet anywhere within a distance of $\Delta R < 1.0$. The isolation cut removes approximately 0.01% of jets (see Figure 4.13), and has almost no impact on the final measurement.

A final calibration, referred to as the cross calibration [35] was applied to the data to account for observed differences in the calorimetric response between data and MC. The cross-calibration factors were estimated

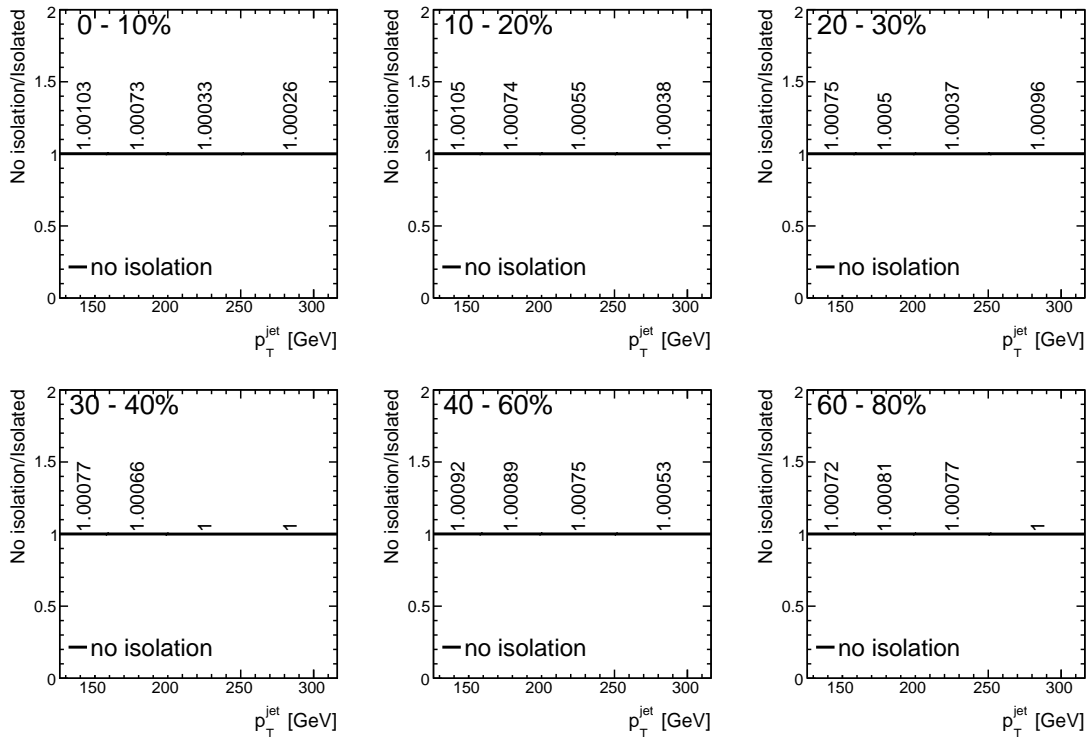


Figure 4.13: The ratios of the jet spectra with no isolation to that with isolation in the kinematic range of interest for Pb+Pb collisions, in all centralities. The isolation requirement rejects less than 0.1% of jets, and has almost no impact on the final measurement

using in-situ calibration studies [22] where jets are measured in events while recoiling against objects for which the energy scale is well known. No correction for the jet reconstruction efficiency is necessary, as the analysis is performed in the jet p_T region where the jet reconstruction is fully efficient [36].

The jet energy measured in the calorimeter can be affected by the presence of dead cells or cells with a bad response, by noise spikes in the hadronic end-cap, by a noise in EM calorimeter and by out-of-time energy deposits from cosmic rays and beam backgrounds. In the pp analysis, the set of recommended cuts of “LooseBad” is used to remove bad jets. The rate of these jets in the kinematic region of interest (100–316 GeV) is less than 0.5%. This cleaning procedure is not applied in Pb+Pb collisions because it is incompatible with the heavy ion jet reconstruction procedure, and also because the low luminosity ensures noise bursts are negligible. This is standard procedure for all heavy ion jet analyses.

4.5.2 Track selection

The track selection cuts used here follow the cuts used in [13]. These provide a low level of fake tracks and a track reconstruction efficiency that is independent of the p_T of the jet the track is associated with. The cuts used here are the “tight” cuts as described in Ref. [37] and were utilized in previous HI jet fragmentation measurements. The default tracking cuts used both in pp and Pb+Pb analysis are:

- track $p_T > 1$ GeV
- track $|\eta| < 2.5$
- tracks should have at least 9 silicon hits in $|\eta| \leq 1.65$
- tracks should have at least 11 silicon hits in $|\eta| > 1.65$
- tracks should have at least 1 hit in IB-layer + B-layer.
- tracks should have a IB-layer hit if it is expected, i.e. if the track passed an active module.
- tracks should have a B-layer hit if it is expected and IB-layer hit is not expected.
- tracks should have less than 3 holes in silicon detectors.
- tracks should have 0 holes in pixel detector.
- impact parameters of track with respect to primary vertex: $|d_0| << 0.47 \times \exp(-0.15 \times p_T) + 0.19 \times \exp(0.00034 \times p_T)$ mm, $|z_0 * \sin \theta| < 1.0$ mm. Recommendation values are $|d_0| < 1.5$ mm for tracks with $p_T < 10$ GeV and $|d_0| < 0.2$ mm for tracks with $p_T > 10$ GeV.

This was chosen to guarantee a smooth behavior of the d_0 parameter as a function of track momentum.

- An additional cut on the track to jet p_T ratio is included. All tracks with

$$p_T^{\text{ch}} > p_T^{\text{jet}} + \sqrt{(3 \times \sigma_{\text{JER}}(p_T^{\text{jet}}))^2 + (3 \times \sigma_{\text{TMR}}(p_T^{\text{ch}}))^2} \quad (4.7)$$

are rejected from the analysis. Where the TMR stands for track momentum resolution. The purpose of this cut is to be consistent with previous fragmentation measurements [13]. It has minimal impact on this analysis because it is restricted to tracks below 63 GeV and jets above 100 GeV.

A tighter tracking selection is used for systematic studies (“tight+” cuts). These cuts include all of the default cuts plus a 3σ cut on the significance of the d_0 and $z_0 \sin \theta$. Figures 4.14-4.16 shows comparisons of the data and MC tracking quantities in pp and Pb+Pb collisions, respectively, for different track p_T intervals. Overall the MC describes the data well. A 20% discrepancy is observed for low impact parameters. The discrepancy is present far from the values of corresponding tracking cuts. A small overall shift of the z_0 distribution is observed in MC samples. This difference is caused by the allowance of a small difference in the z position of the primary vertex in the MC overlay procedure. However this has negligible impact on the analysis as the overall quality requirement on the pointing in the z_0 is 1 mm. Furthermore, Fig. 4.16 shows the same comparison for high p_T tracks. All the comparisons of distributions show the same qualitative features as seen at lower p_T with improving pointing with increasing track p_T . The comparison of the reconstructed p_T^{ch} with the generated kinematics for tracks passing these cuts is shown in Fig. 4.17.

Figure 4.18 presents the impact of individual tracking requirements in terms of the ratio of the number of tracks that pass given cut and the total number of reconstructed tracks in pp MC. The study is presented as a function of track pseudorapidity in two different track p_T intervals and as a function of track p_T in two different pseudorapidity intervals. The highest rejection for low p_T tracks is provided by the cut on d_0 pointing. At high p_T the dominant effect is seen from the requirement on the number of silicon hits. Similarly, Fig. 4.19 presents the impact of individual tracking requirements in Pb+Pb MC. The difference between the impact of individual cuts can be attributed to a different setting of the tracking algorithm and to the overall increase of the track multiplicity as the number of rejected tracks does not linearly scale with the multiplicity that enters the denominator.

The primary particles used in this analysis have a mean lifetime $\tau > 0.3 \times 10^{-10}$ s and are either directly produced in pp interactions or from subsequent decays of particles with a shorter lifetime. They are required to have their barcode in the range 0 – 200000. Of these, particles with barcode < 10000 are coming from Pythia, while the remaining are from HIJING. Particles with barcodes above 200000 are secondaries, and come from weak decays of Λ , K_S , Ξ , Σ , Ω and from particles created in interactions with the material.

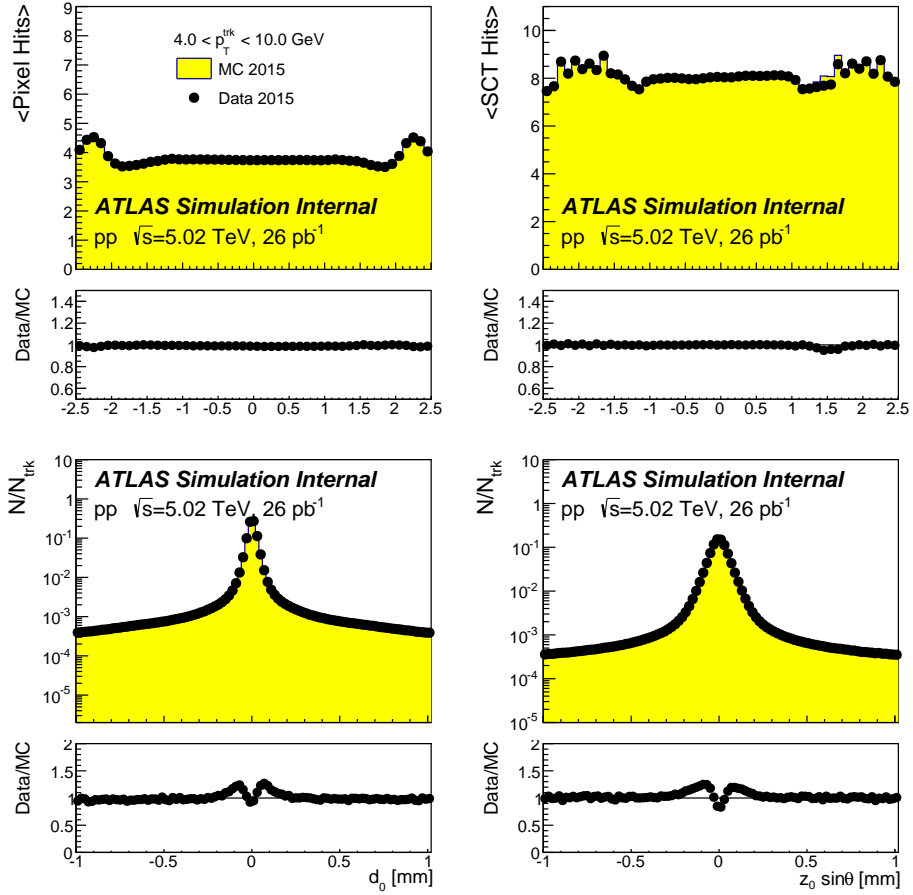


Figure 4.14: Track quantity comparison between data (points) and MC (yellow histogram) in pp collisions. Tracks are selected to have $4.2 < p_T^{\text{ch}} < 10$ GeV. Below each direct data and MC overlay is the corresponding data to MC ratio. The quantities compared are: average number of pixel hits as a function of η^{ch} (top left), average number of SCT hits as a function of η^{ch} (top right), and number of tracks, N_{trk} , normalized d_0 (bottom left), and $z_0 \sin \theta$ distributions (bottom right).

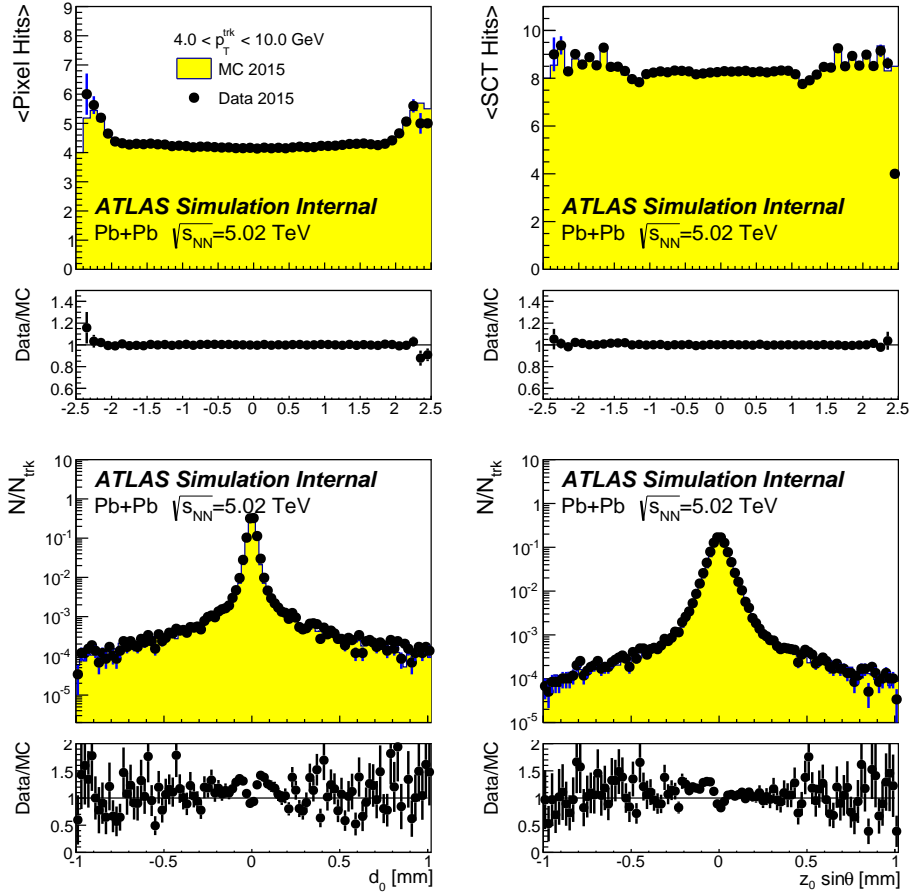


Figure 4.15: Track quantity comparison between data (points) and MC (yellow histogram) in 0-10% central Pb+Pb collisions. Tracks are selected to have $4.2 < p_T^{\text{ch}} < 10 \text{ GeV}$. Below each direct data and MC overlay is the corresponding data to MC ratio. The quantities compared are: average number of pixel hits as a function of η^{ch} (top left), average number of SCT hits as a function of η^{ch} (top right), track d_0 (bottom left), and track $z_0 \sin \theta$ (bottom right).

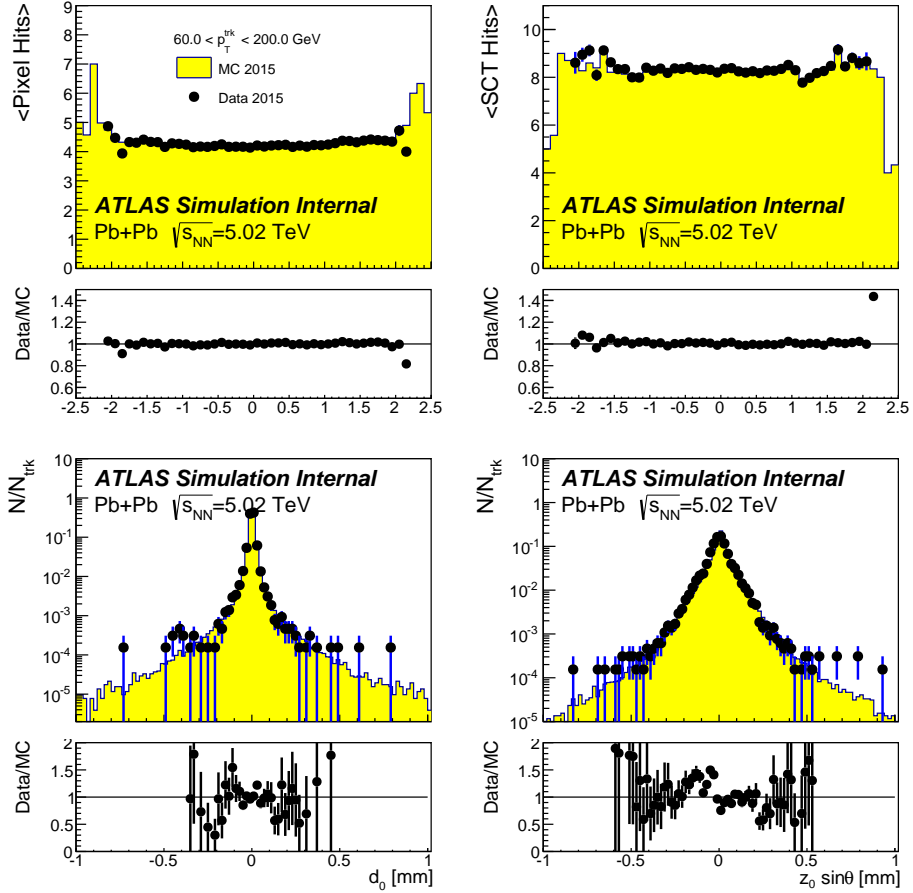


Figure 4.16: Track quantity comparison between data (points) and MC (yellow histogram) in Pb+Pb collisions inclusive in collisions centrality. Tracks are selected to have $60 < p_{\text{T}}^{\text{ch}} < 200 \text{ GeV}$ and to originate from jet with p_{T} in the interval from 251 to 316 GeV. Below each direct data and MC overlay is the corresponding data to MC ratio. The quantities compared are: average number of pixel hits as a function of η^{ch} (top left), average number of SCT hits as a function of η^{ch} (top right), track d_0 (bottom left), and track $z_0 \sin \theta$ (bottom right).

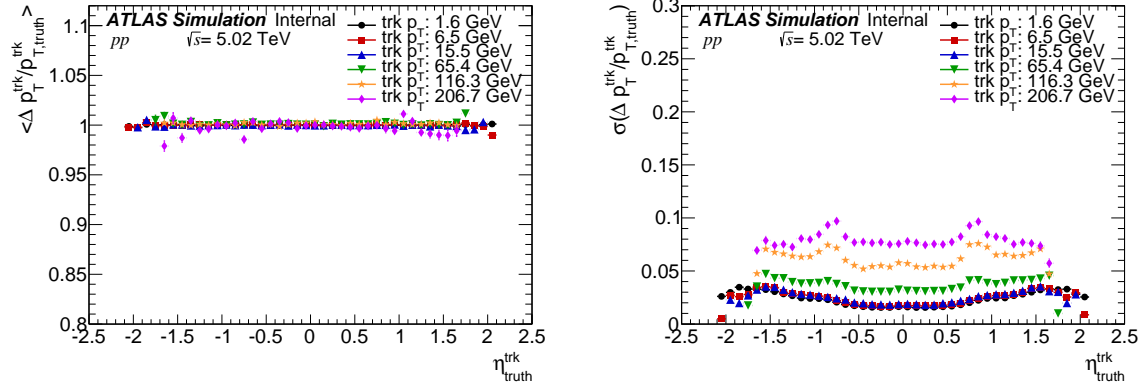


Figure 4.17: (left) Comparison of the generated and reconstructed track p_T as a function of $\eta_{\text{truth}}^{\text{trk}}$ for five track $p_T^{\text{trk},\text{Truth}}$ selections. (right) Track momentum resolution as a function of $\eta_{\text{truth}}^{\text{trk}}$ for five $p_T^{\text{trk},\text{Truth}}$ selections. Both plots are for pp MC. All tracks shown in this plot have passed the 2015 default tracking cuts defined in this section. The p_T in the legend corresponds to the bin centers in the following track p_T bins: 1.3 – 1.8 GeV, 5.6 – 7.5 GeV, 13.3 – 17.7 GeV, 56.1 – 74.8 GeV, 99.7 – 132.9 GeV, 177.2 – 236.2 GeV

Strange baryons are included: Σ^- (PDG ID 3112), Σ^+ (PDG ID 3222), Ξ^- (PDG ID 3312), Ω^- (PDG ID 3334).

4.5.3 Track momentum correction

Specific correction is needed for track momentum in 5 TeV pp and Pb+Pb data to account for miss-alignment introduced in the track reconstruction. The sign charge dependent momentum scale shift was observed in pp data when the transverse momentum of muons reconstructed using muon spectrometer was compared to the transverse momentum of muons from the inner detector. The difference as a function of muon momentum in Pb+Pb data can be seen in Fig.4.20. The correction to track p_T as a function of track η and track ϕ is applied through sagitta bias maps introduced in InDetTrackSystematicsTools-00-00-19 [38].

4.5.4 Track reconstruction efficiency

The track reconstruction efficiencies are evaluated by using MC tracks. The tracking reconstruction efficiency is defined as the ratio between the number of primary truth charged particles that are reconstructed and the total number of primary truth charged particles in the given p_T and η bin. Tracks are required to pass all the tracking cuts imposed on the data.

Matching between the reconstructed and the truth track is done via a cut on mc_{prob} . The mc_{prob} variable

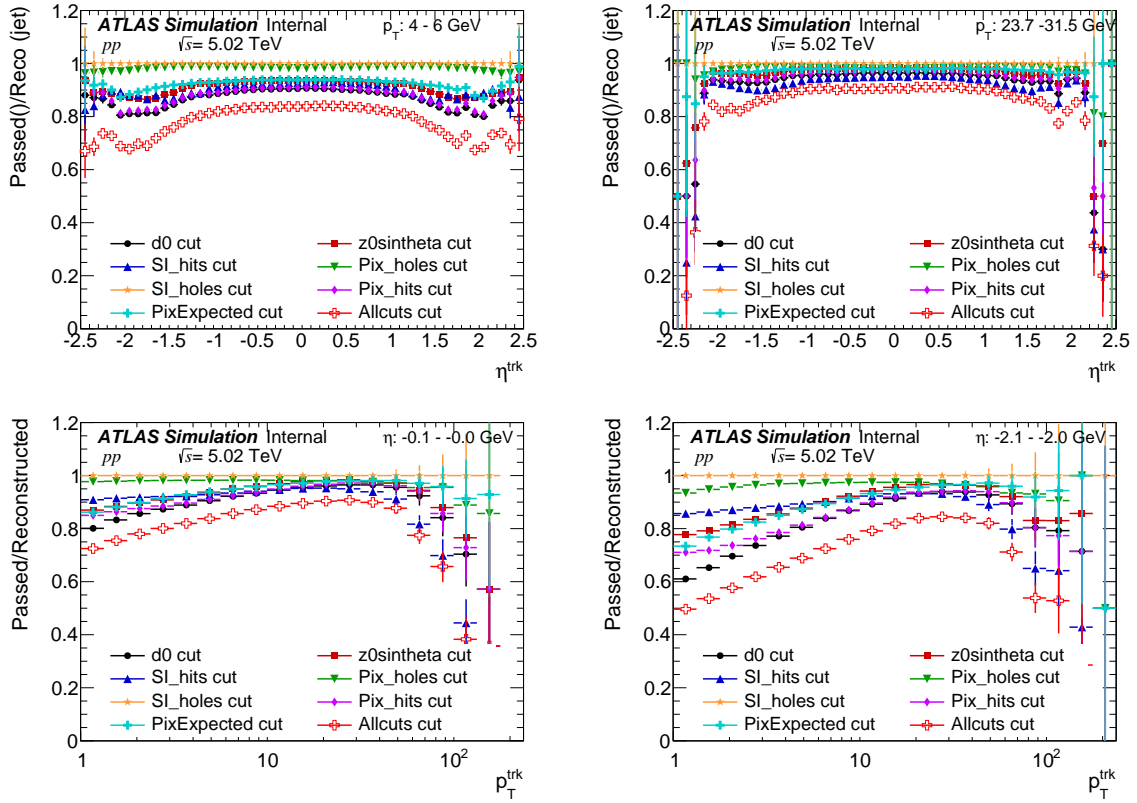


Figure 4.18: The impact of each cut applied individually in the pp MC to the starting collection of tracks, as a function of η^{ch} (top) for $1.3 < p_T^{\text{ch}} < 4.6$ GeV (left) and for $23.7 < p_T^{\text{ch}} < 31.5$ GeV and as a function of track p_T for two different pseudorapidity intervals (bottom). The final combination of all cuts is shown as well.

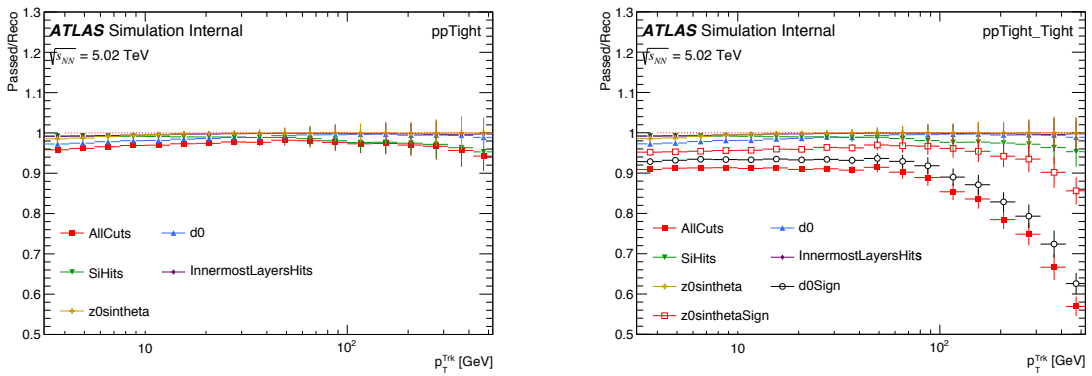


Figure 4.19: The impact of each cut applied individually in the $\text{Pb}+\text{Pb}$ MC to the starting collection of tracks, as a function of the track p_T inclusive in collision centrality for the default and the tight set of tracking requirements. The final combination of all cuts is shown as well.

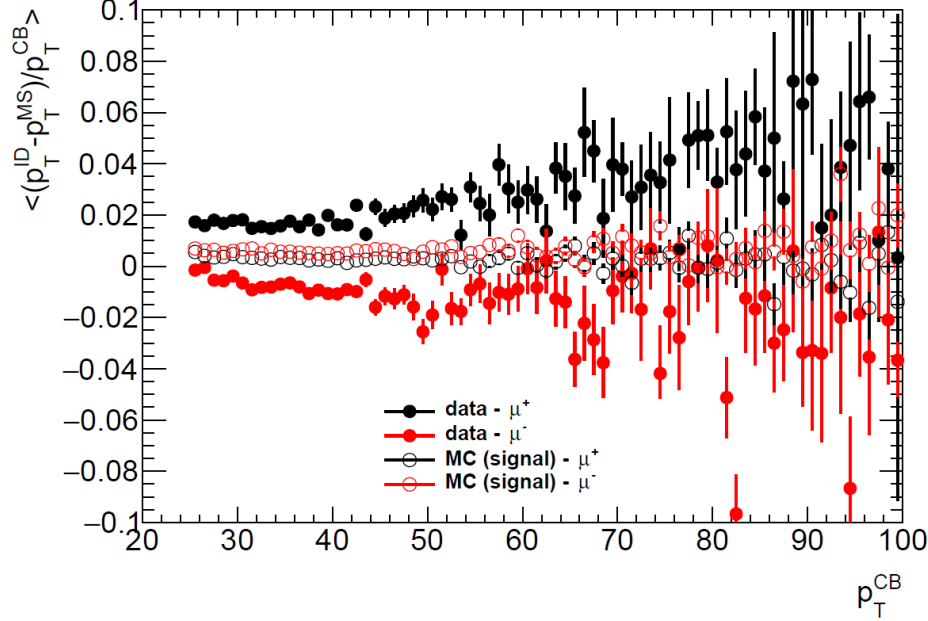


Figure 4.20: Comparisons of track momentum scale of positive and negative muons reconstructed using muon spectrometer and inner detector. The muon traverse momentum evaluated from muon spectrometer (MC) is compared by that evaluated using the inner detector (ID) and the relative scale is normalized by the momentum that uses both detectors (CB). [39]

is calculated according to:

$$mc_{prob} = \frac{10N_{pix}^{\text{common}} + 5N_{\text{SCT}}^{\text{common}} + N_{\text{TRT}}^{\text{common}}}{10N_{pix}^{\text{track}} + 5N_{\text{SCT}}^{\text{track}} + N_{\text{TRT}}^{\text{track}}} \quad (4.8)$$

where N_X^{common} are the number of hits in detector X in common between the truth and reconstructed track. N_X^{track} is the number of total hits in the reconstructed track. Tracks with a mc_{prob} greater than 0.3 are associated with the truth track and those with a lower value are not and are classified as fake tracks. The choice of the mc_{prob} cut of 0.3 is based on the recommendation from the tracking group and was used in [14]. The sensitivity of the measurement on the value of the mc_{prob} cut is included in the systematic uncertainties.

In MC samples, the “track barcode” classifies reconstructed tracks to different classes based on the origin (primary, secondary, pileup, beam halo, fake...). We require $0 < \text{barcode} < 200000$ in evaluation of the tracking efficiency to remove pileup, beam halo, secondary particles, and fake particles. Reconstructed tracks which do not have a matched truth track with given mc_{prob} are labeled all together as fake tracks. The tracking cuts need to provide both good efficiency for generator level tracks and to adequately reject fakes.

The final efficiency corrections applied were determined and applied as a function track p_T and track η , and can be seen in Figures 4.21-4.22 for pp and Pb+Pb collisions. No significant dependence on the collision centrality is observed. The efficiency exhibits a small, but monotonic increase with the track p_T . Only a

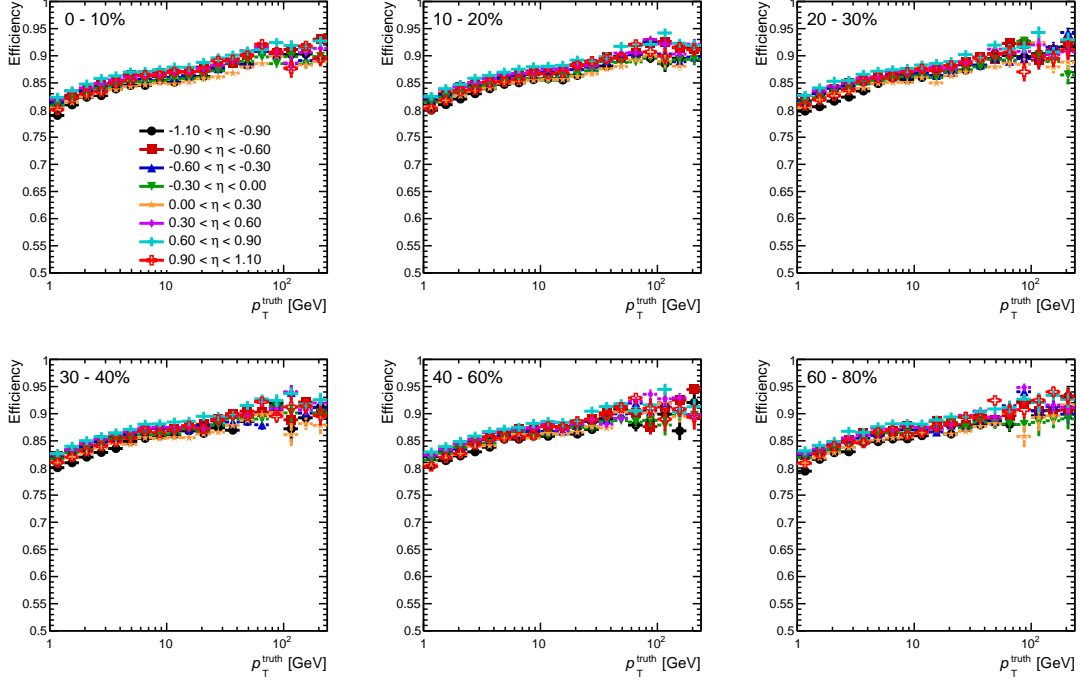


Figure 4.21: Efficiency for reconstructing tracks evaluated using the default tracking selections in different track η bins in the data overlay Pb+Pb MC samples. Each panel is a different centrality bin.

small variation with the track η is observed in the region $|\eta| < 1.1$. The efficiency correction is applied on a track-by-track basis, assuming $p_T^{\text{ch}} = p_T^{\text{truth}}$. While that assumption is not strictly valid, the efficiency varies sufficiently slowly with p_T^{truth} that the error introduced by this assumption is negligible, up to 1%. The tracking efficiency determined in Ref. [13] was not seen to be dependent on p_T^{jet} for $p_T^{\text{ch}} \lesssim 40$ GeV as can be seen in Fig. 4.23-4.25. The small depletion of the efficiency for tracks with $p_T \sim 10 - 40$ GeV was attributed to the convolution of how jet fragments and with the performance of the track reconstruction in the dense core of the jet [13].

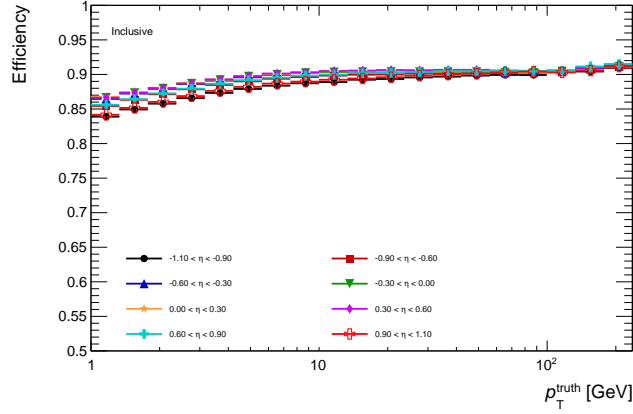


Figure 4.22: Efficiency for reconstructing tracks evaluated using the default tracking selections in different track η bins in the pp MC samples.

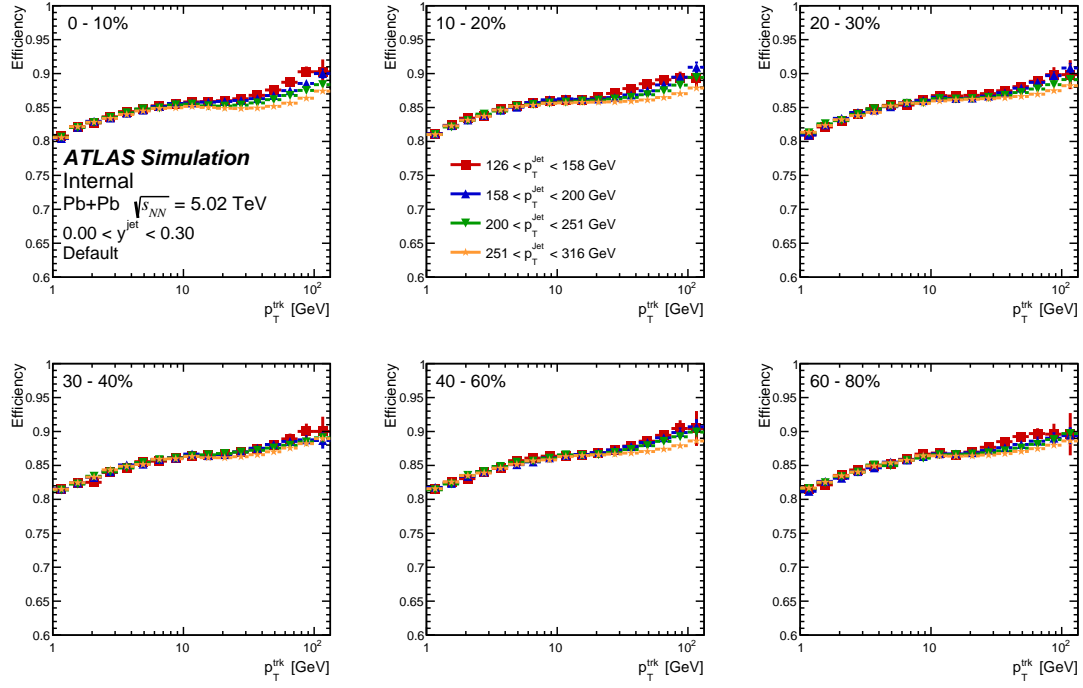


Figure 4.23: Efficiency for reconstructing tracks evaluated using the default tracking selections in different jet p_T bins and jet rapidity interval $|y| < 0.3$ in the data overlay Pb+Pb MC samples. Each panel is a different centrality bin..

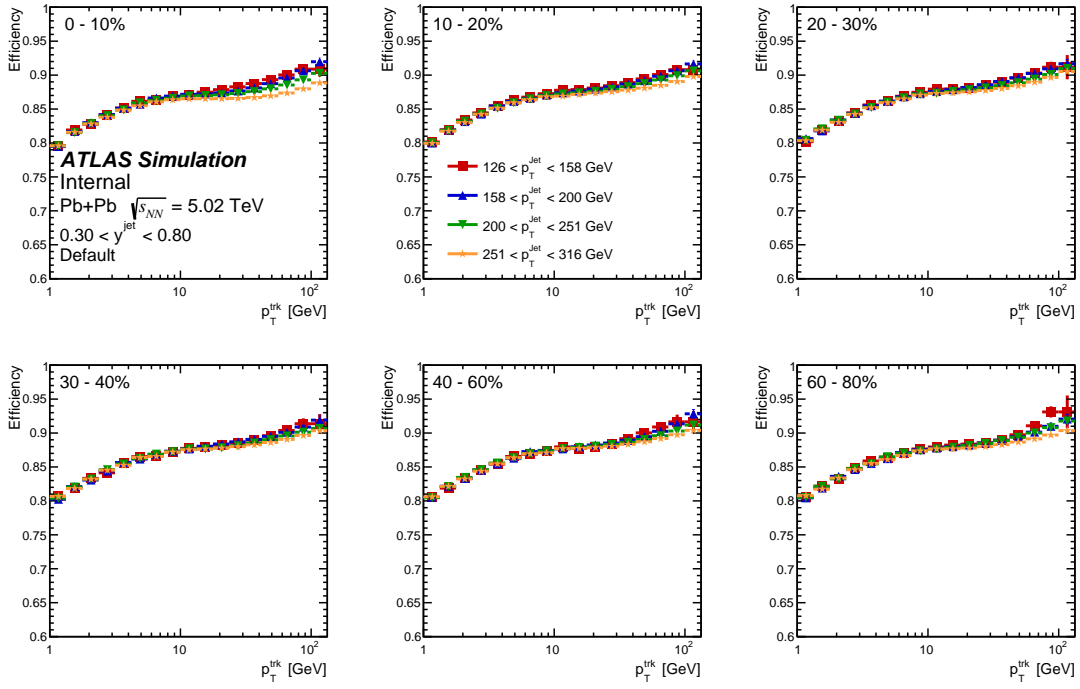


Figure 4.24: Efficiency for reconstructing tracks evaluated using the default tracking selections in different jet p_T bins and jet rapidity interval $0.3 < |y| < 0.8$ in the data overlay Pb+Pb MC samples. Each panel is a different centrality bin..

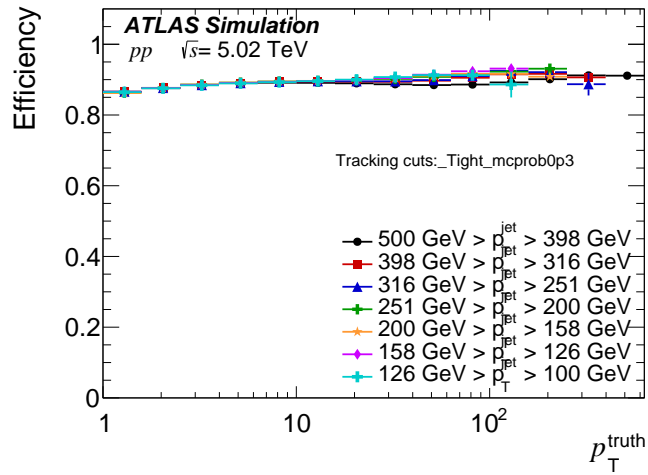


Figure 4.25: Efficiency for reconstructing tracks evaluated using the default tracking selections in different jet p_T bins, in the pp MC samples.

4.5.5 Fake rates

Reconstructed tracks that cannot be matched to a primary particle in the MC samples or are matched to a secondary particle are considered to be “fake” tracks. The rate of these tracks was evaluated and extensively studied in Ref. [13] in the pp , Pb+Pb HIJING MC, and in Pb+Pb MC+overlay samples. The MC overlay sample is used to crosscheck the fake rate at higher p_T , but is not used for any corrections. It was shown that as the p_T^{ch} approaches the p_T^{jet} the fraction of fake tracks increases due to the steeply falling spectra of generator level tracks. Figures 4.26 and 4.27 show the fraction of tracks that are identified as fakes, secondaries, or part of UE in case of Pb+Pb collisions as a function of p_T^{ch} for selections in p_T^{jet} in pp and Pb+Pb collisions, respectively. The rate decreases with p_T^{ch} up to approximately 10 GeV and then remains constant until p_T^{ch} approaches p_T^{jet} where the rate increases again. In Pb+Pb collisions, the “fake” rate also includes tracks which are from the underlying event from the real collisions into which the jet is overlaid. The rate of these underlying event tracks increases with decreasing p_T^{ch} and increasing collision centrality. The contribution from UE is negligible for tracks with p_T above 10 GeV as no centrality dependence is seen. The Fig. 4.27 excludes the very low p_T region where the distribution would be completely dominated by the UE. The size of the UE is then presented further in Fig. 4.39-4.40. To separate the contribution of UE tracks (see section 4.5.6) from the fake tracks in Pb+Pb collisions and cross-check the centrality dependence of the fake rate, 0.2M MB Pb+Pb fully reconstructed HIJING MC [40] events was used. The HIJING MC generator is capable of simulating global properties of HI collisions. The estimated fake rate of tracks associated with jets with $p_T > 40$ GeV is at the level of 1% and it exhibits similar behavior as observed in Fig. 4.27. No significant dependence of the fake rate on the collision centrality was found [13].

To correct for the contribution from fake and secondary particles, charged particle distributions are estimated using reconstructed tracks that do not have a truth match as defined by criteria described in previous paragraphs. These distributions are then subtracted from the measured distributions both in the data and MC. This procedure is applied for tracks above 10 GeV in Pb+Pb collisions and for tracks above 1 GeV in pp collisions. The correction also removes any residual UE above 10 GeV in case of Pb+Pb. The choice of the 10 GeV cut is based on the centrality dependence of the rate of truth-unmatched tracks in MC overlay samples shown in Fig. 4.27. The correction for UE, fake and secondary tracks below 10 GeV in Pb+Pb collisions is discussed in the next section.

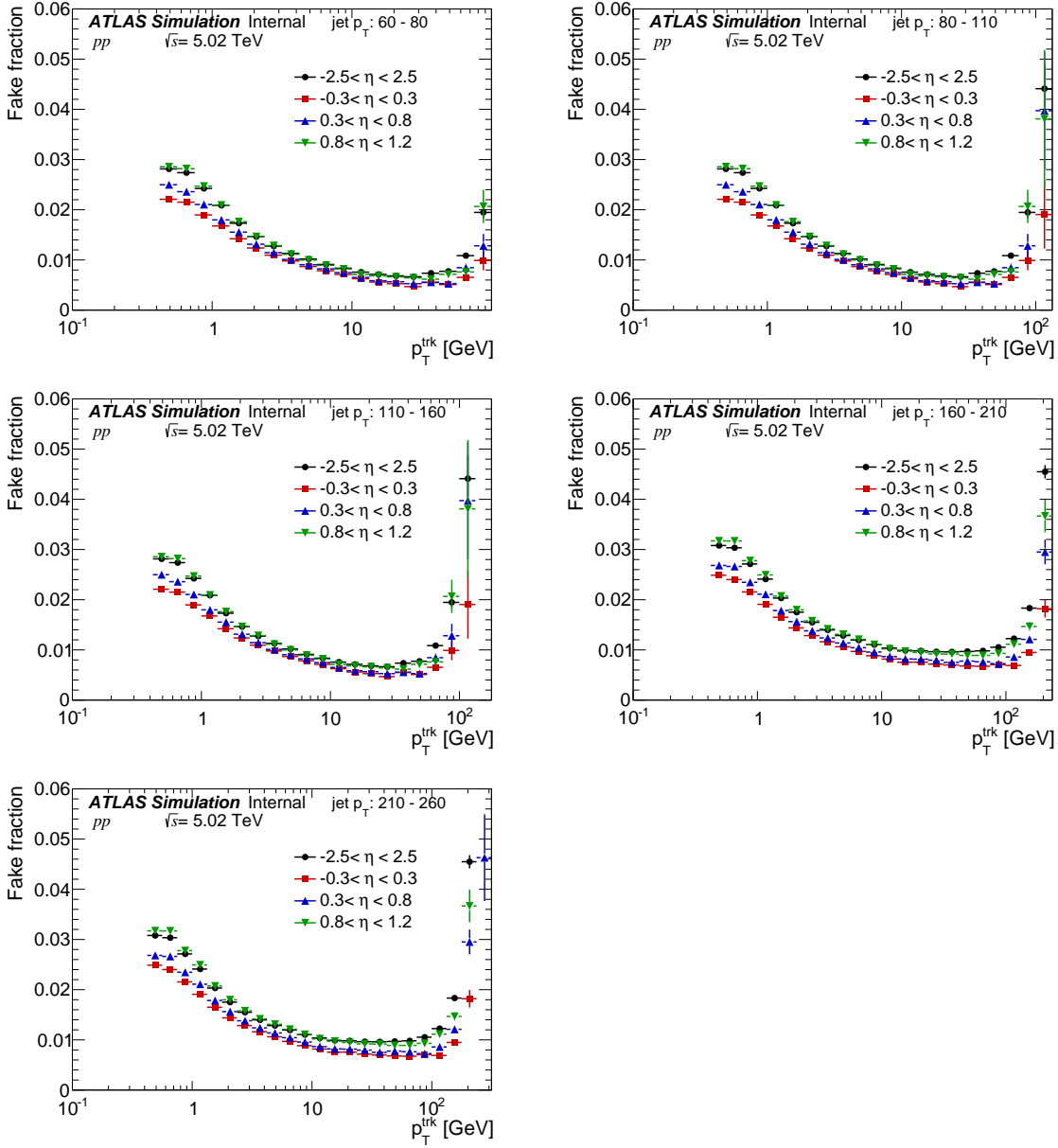


Figure 4.26: Fake rate for five different p_T^{jet} selections in 5.02 TeV pp collisions and four pseudorapidity intervals. The fake rate is evaluated for default value of MC_{prob} cut of 0.3 used in 2015 analysis.

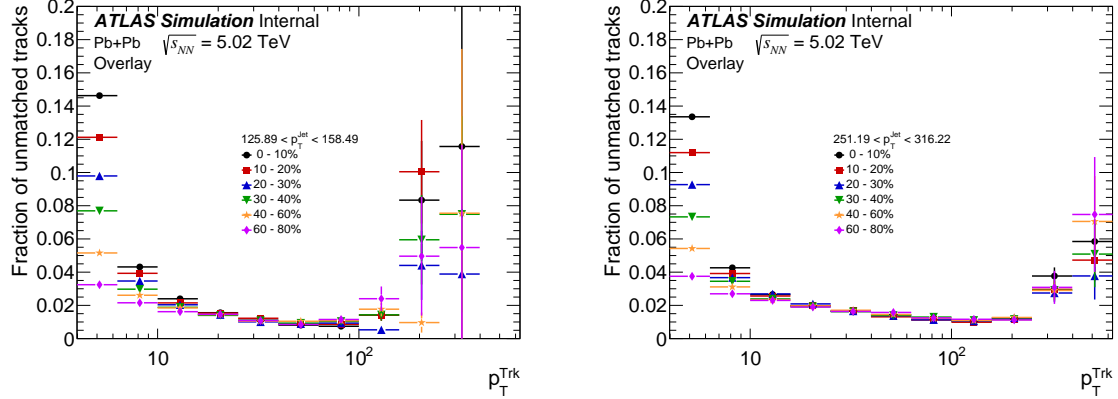


Figure 4.27: Rate of tracks unmatched to truth tracks in Pb+Pb collisions for different centrality selections as indicated on the plot as a function of p_T^{ch} . The unmatched tracks include both fake tracks and tracks from the underlying event. The panels show two p_T^{jet} selections: 126–158 GeV (left) and 251–316 GeV (right). The low p_T part is omitted as it is dominated by the contribution from the UE.

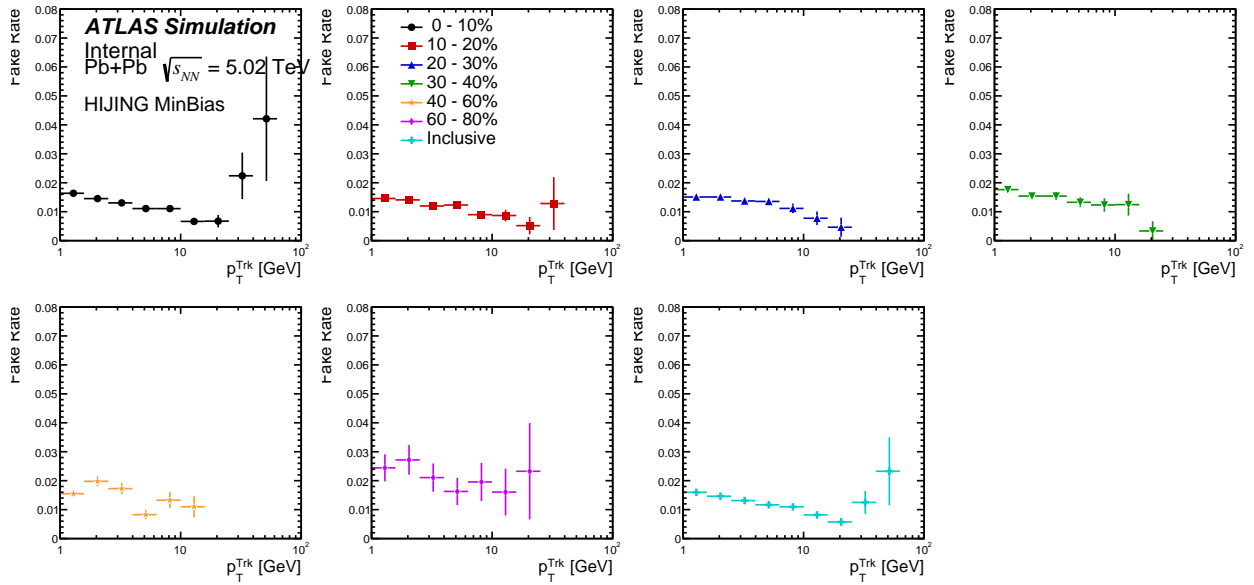


Figure 4.28: Fake rate for six different centrality intervals in 5.02 TeV Pb+Pb HIJING MC collisions. The fake rate is evaluated for default value of $\text{MC}_{\text{Probcut}} = 0.3$ used in 2015 analysis.

4.5.6 Underlying event subtraction of tracks

The underlying event subtraction performed on the calorimetric jet energy is described in Sec. 4.4. Charged particles from the nucleon-nucleon scatterings that are not associated with the hard scattering in question constitute a background to the $D(p_T, r)$ distributions that needs to be subtracted from the measured distributions. This background strongly depends on the collisions centrality and on the charged particle p_T . In the measurement of the inclusive jet fragmentation functions it was found that the UE contribution is negligible for charged particles with $p_T > 10$ GeV [13]. This can be seen in the centrality dependence of the combined rate of fake and underlying event charged particles shown in Fig. 4.27 where no significant centrality dependence is observed for track above 10 GeV.

In pp collisions, the UE is not subtracted. The pileup contribution is negligible and subtracting the intrinsic UE from the hard scattering processes would also necessitate a similar subtraction in the particle level fragmentation functions in Pb+Pb that would be generator dependent and make comparisons between pp and Pb+Pb non-trivial.

In Pb+Pb collisions, the UE from the soft processes is estimated using two methods. The nominal “Map method”, and the alternative “Cone method” to provide a systematic uncertainty. The former uses charged particle distributions of $dN_{ch}/d\phi d\eta(\text{cent}, p_T, d\Psi_{ch})$ in MC overlay events, while the latter evaluates the underlying event on an event-by-event basis using a grid of cones.

Map Method

In the ”Map Method”, $\eta - \phi$ maps of the average number of UE charged particles in a given annulus around a jet ($n_{ch}^{\text{UE Map}}$) are determined in MC overlay events using tracks without a truth match. The maps are filled as a function of the distance from the jet, p_T^{jet} , η^{jet} , ϕ^{jet} , angle of the jet to the reaction plane⁴ $d\Psi_{ch}$, p_T and centrality. Examples of the these distributions for three different annuli (0–0.05, 0.25 – 0.30, 0.60–0.70), in the $d\Psi$ interval of 0.80 – 1.00, for six collision centrality classes and for 1–1.6 GeV particles in 126 – 158 GeV jets are shown in Fig. 4.29. The number of UE particles associated with a jet decreases with size of the annulus, decreasing centrality, increasing track p_T and increasing distance to the reaction plane.

The underlying event in MC is determined by applying the map method to MC. This is achieved by convoluting the $n_{ch}^{\text{UE Map}}$ distributions with the η_{jet} , ϕ_{jet} , and $d\Psi_{jet}$ distributions of jets. The UE estimated by this method in MC consists of tracks without a truth match, and hence is the “true” underlying event by definition. This UE^{MC} can then be used to correct any correlations between the underlying event as determined by the cone method and the JER (discussed in later sections). The UE normalized to unit area,

⁴The reaction plane angle Ψ is determined on an event-by-event basis by a standard method using the ϕ variation of transverse energy in the forward calorimeter

as a function of ΔR with respect to the jet axis is shown in Fig.4.30 for the lowest track p_T interval where the UE contribution is the largest. The two distributions are the UE with and without secondary particles. The UE strongly decreases for more peripheral collisions and for increasing track p_T . Little radial dependence is seen when the secondaries are not included. A small effect is expected because there is an enhancement in the number of jets at mid rapidity, along with a decrease in the UE yield as a function of η . Since the secondaries are generated by primary PYTHIA particles, the enhancement is expected towards the jet core, where there is a higher multiplicity of primary particles.

The map method is then applied to data to measure the UE charged particle contribution to the measured $D(p_T, r)$ distributions. Since this method uses real MB Pb+Pb collisions (from the MC overlay samples that have been reweighed to match the centrality distribution in data), the underlying event distribution is the same as in the data. This method does not require a correction for the correlation between the underlying event and the JER because it is based on tracks without a truth match.

Cone Method

The cone method uses a regular grid of 9 cones of size $R = 0.8$ covering the full inner detector region (shown in Fig.4.31). The size of the cone corresponds to the radial phase space being investigated (0.8 in this case). Cones within a distance of $dR = 1.6$ to a reconstructed jet are excluded if $p_T^{\text{jet}} > 90$ GeV. They are also excluded if they contain a track with $p_T > 10$ GeV. The 10 GeV was cut was chosen based on the small centrality dependence of the combined rate of fake and underlying event tracks above 10 GeV as shown in Fig.4.28. The fraction of events as a function of number of cones used in each centrality bin is shown in Fig.4.32. It can be seen that in the MC the number of cones used is consistent with there being no jet quenching. Moreover, quenching in central Pb+Pb data leads to only one jet causing exclusions, consistent with most events using 7 cones. For more peripheral Pb+Pb collisions, the cone distribution tends to look like the distribution with no quenching for more peripheral collisions.

The resulting UE charged particle yields $dn_{\text{ch}}^{\text{UECone}}/dp_T^{\text{ch}}$ are evaluated over the 1 – 10 GeV range as a function of p_T^{jet} centrality, and r , and then averaged over all cones according to.

$$\frac{dn_{\text{ch}}^{\text{UECone}}}{dp_T^{\text{ch}}} = \frac{1}{N_{\text{cones}}} \frac{1}{\varepsilon} \frac{\Delta N_{\text{ch}}^{\text{cone}}(p_T^{\text{ch}}, p_T^{\text{jet}}, \eta^{\text{jet}})}{\Delta p_T^{\text{ch}}} \quad (4.9)$$

Here N_{cones} is the number of background cones associated with a given jet with p_T^{jet} . $\Delta N_{\text{ch}}^{\text{cone}}$ is the number of charged particles summed across all background cones associated to the jet in question. The cone method estimates the UE yields only from events containing jets included in the analysis, ensuring that the

background automatically had the correct distribution of centralities within a given centrality bin. The UE contribution as measured using the cone method in data needs to be further corrected for three effects:

Correction for η -dependence: To account for differences in the yields of UE particles at the position of the jet and at the position of the track for the random cone entering the UE estimate, the η distribution of charged particles from MC overlay events is used to appropriately weigh the UE tracks. The correction is then the ratio of the value of the $dn_{ch}/d\eta$ at the position of the jet and the track. The impact of the correction in 0-10% Pb+Pb collisions is shown in Fig.4.33

Correction for flow: Elliptic flow is the characteristic sinusoidal modulation of the yields of particles along the azimuth in heavy ion collisions. The maximum amplitude of the modulation determines the reaction plane, with more momenta being measured in plane than out of plane. Ref [41] provides a basic measurement of the magnitude of the elliptic flow, and its p_T dependence. The correction for this effect was based on a parametrization of the p_T^{ch} and centrality dependence of previously measured elliptic flow coefficients, v_2 [41]. The reaction plane angle Ψ is estimated on an event-by-event basis by using the ϕ variation of transverse energy in the forward calorimeter. The correction factor is evaluated as a function of the distance of the jet from the reaction plane $\cos 2(\phi^{\text{jet}} - \Psi)$. The correction is less (greater) than unity for jets in a direction perpendicular (parallel) to the reaction plane. Jets perpendicular (parallel) to the plane typically have a lower (higher) UE, and a cone at a random position in the ID is corrected down (up). The size of the correction is at the level of a few percent, and decreases with increasing track p_T , as is shown in Fig.4.34

UE and JER correlation: The interplay between the UE and the JER will be described here is discussed in detail in Ref. [42]. Due to the steeply falling nature of the jet p_T spectra, the smearing due to jet energy resolution leads to a net migration of jets from lower p_T to higher p_T values (hereafter referred to as “up-feeding”) such that a jet reconstructed with a given p_T^{rec} will correspond, on average, to a lower truth jet p_T , $\langle p_T^{\text{truth}} \rangle$. The up-feeding was observed to induce in the MC a difference between the UE yields determined using the MC overlay events and the actual UE contribution to reconstructed jets. The magnitude of this difference was found to be centrality dependent and exhibited a weak p_T dependence. That difference was found to result from intrinsic correlations between the UE contribution to the yield of particles measured inside the jet and the MC p_T shift, $\Delta p_T^{\text{jet}} = p_T^{\text{rec}} - p_T^{\text{truth}}$. In particular, jets with positive (negative) Δp_T^{jet} were found to have an UE contribution larger (smaller) than jets with $\Delta p_T^{\text{jet}} \sim 0$.

To correct for this effect, the centrality-, p_T -, r - and p_T^{ch} -dependent multiplicative correction factors were applied on $dn_{ch}^{\text{UE,Cone}}/dp_T^{ch}$ distributions. These multiplicative factors, w_{UE} , were estimated as a ratio of UE

distributions calculated in MC samples using the "Map method", $D(p_T, r)_f$, and the "Cone Method".

$$w_{\text{UE}}(p_T) = \frac{dn_{\text{ch}}^{\text{UE Map}}/dp_T^{\text{ch}}}{dn_{\text{ch}}^{\text{UE Cone}}/dp_T^{\text{ch}}} \Big|_{\text{MC}} \quad (4.10)$$

Examples of these factors are shown in Fig 4.35-4.36. The correction by construction corrects also for fakes and secondary contribution in the track p_T region 1-10 GeV in Pb+Pb collisions. These factors are also shown in Figure 4.38, as a function of r for different track p_T bins, for $126 < p_T^{\text{jet}} < 158 \text{ GeV}$. The size of these corrections integrated over $r = 0.4$ is comparable to the UE-JER correction done in [13].

A comparison between the cone method and the map method is shown in Fig.4.37. The difference between the methods varies slowly with p_T^{jet} and track p_T , with a small centrality dependence coming from fact that the underlying event strongly depends on the centrality.

Outside that region and in pp system fake contribution is corrected as described at the beginning of Section 4.5.4. The corrected UE distributions, $d\tilde{n}_{\text{ch}}^{\text{UE+fake}}/dp_T^{\text{ch}}$ are then subtracted from measured distributions as follows

$$\frac{dn_{\text{ch}}^{\text{sub}}}{dp_T^{\text{ch}}} = \frac{dn_{\text{ch}}^{\text{meas}}}{dp_T^{\text{ch}}} - w_{\text{UE}}(p_T) \left(\frac{dn_{\text{ch}}^{\text{UE Cone}}}{dp_T^{\text{ch}}} \Big|_{\text{Data}} \right) = \frac{dn_{\text{ch}}^{\text{meas}}}{dp_T^{\text{ch}}} - \frac{d\tilde{n}_{\text{ch}}^{\text{UE+fake}}}{dp_T^{\text{ch}}} \quad (4.11)$$

The absolute magnitude of the correction increases towards the higher track p_T in the jet core where the UE is smaller. This behavior originates from 1) the intrinsic correlations between the UE contribution to the yield of particles measured inside the jet and the MC p_T shift as it was discussed earlier; 2) the correlation of production of secondary particles with the jet. The production of secondary particles is associated with presence of primary particles. Thus, the production of secondary particles is enhanced in the jet due to the higher density of primary particles compared to the regions outside a jet. This is shown in Fig. 4.30 where the UE evaluated in term of particles without matching to truth particles in MC with and without the contribution from secondary particles is presented and where the yield of secondary particles is significant only at smaller dR , i.e. within a jet. Fig. 4.30 also shows that the relative yield of secondary particles to the yield of the UE particles is increasing with decreasing collisions centrality. Furthermore, the relative contribution of secondary particles to the UE increases with the track p_T as the fraction of the secondary particles decreases only slowly with the increasing track p_T (Figs.4.27), however, the UE decreases strongly with the increasing track p_T (Fig.4.39-4.40). This results in lower UE contribution estimated using the MB collisions where tracks are not associated to a jet.

The impact of the underlying event and fake track subtraction on the $D(p_T, r)$ distributions is shown in Figure 4.39-4.41. The magnitude of this correction is the largest for low track p_T in central Pb+Pb collisions

and the largest annulus. In the most extreme case the S/B ratios can be as low as 1/100. The size of the correction decreases rapidly with increasing track p_T , decreasing centrality and towards the core of the jet. In pp collisions the magnitude of the fake track subtraction is always much less than 5%.

The basic performance of the UE subtraction has been tested in the MC overlay dataset. The closure test was performed using the MC overlay sample that has the same UE as in the data and will be discussed in the next subsection. The truth $R_{D(p_T,r)}$ distributions were compared to fully corrected $R_{D(p_T,r)}$ distributions where the UE contribution is subtracted by the same method as used in the data (see Fig. 4.61). From the above mentioned tests we have concluded that the UE subtraction procedure is correct and works well. The UE estimate is subjected to variation as part of the systematic uncertainties. For the pp data, we have not performed any UE subtraction.

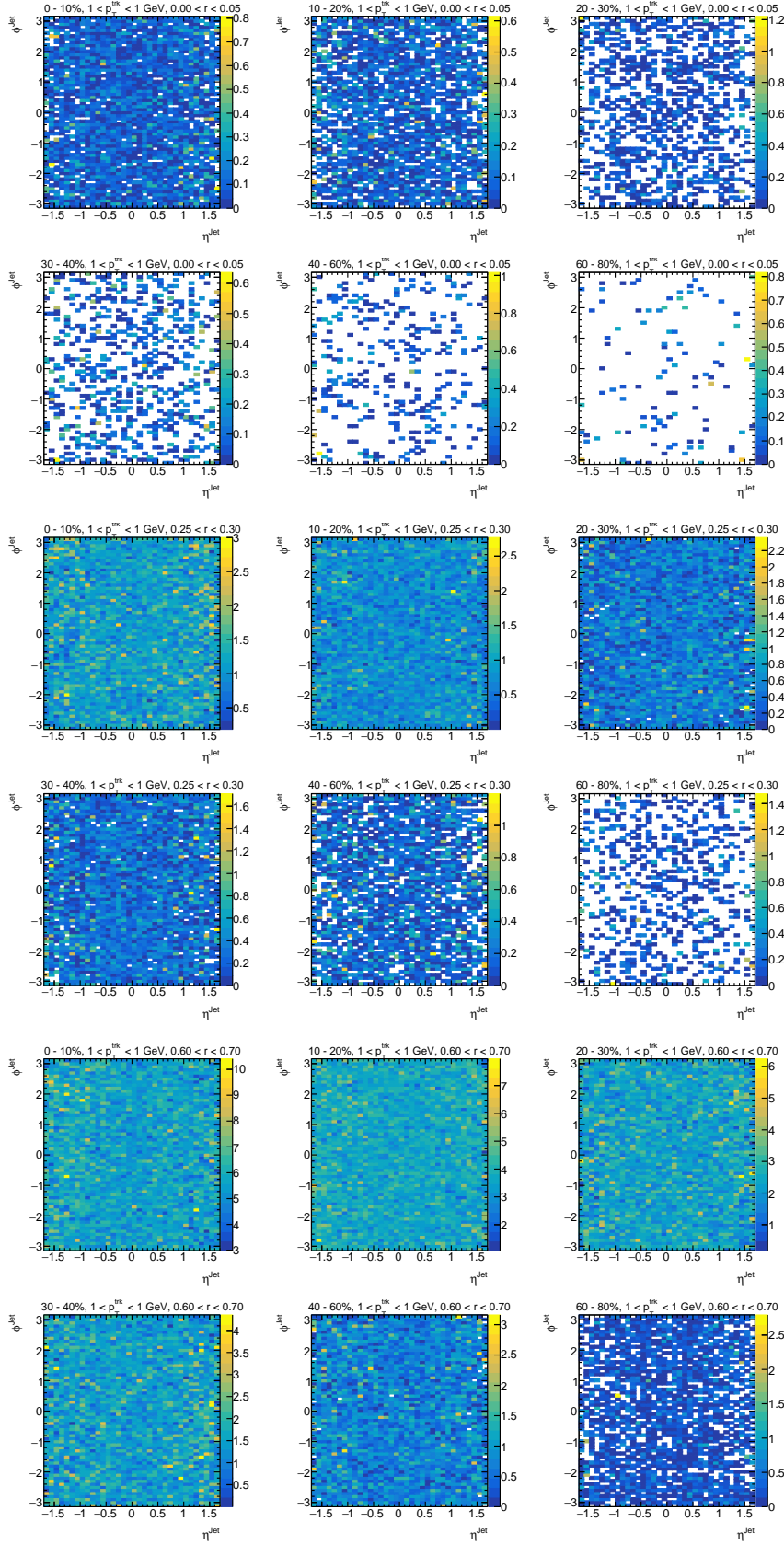


Figure 4.29: Per jet $n_{\text{ch}}^{\text{UEMap}}$ distributions of charged particles evaluated in the jet core, near the jet edge, and far from the jet, for $d\Psi$ in the interval $0.8-1.00$ for six centralities, 1–1.6 GeV tracks, and 126–158 GeV jets.

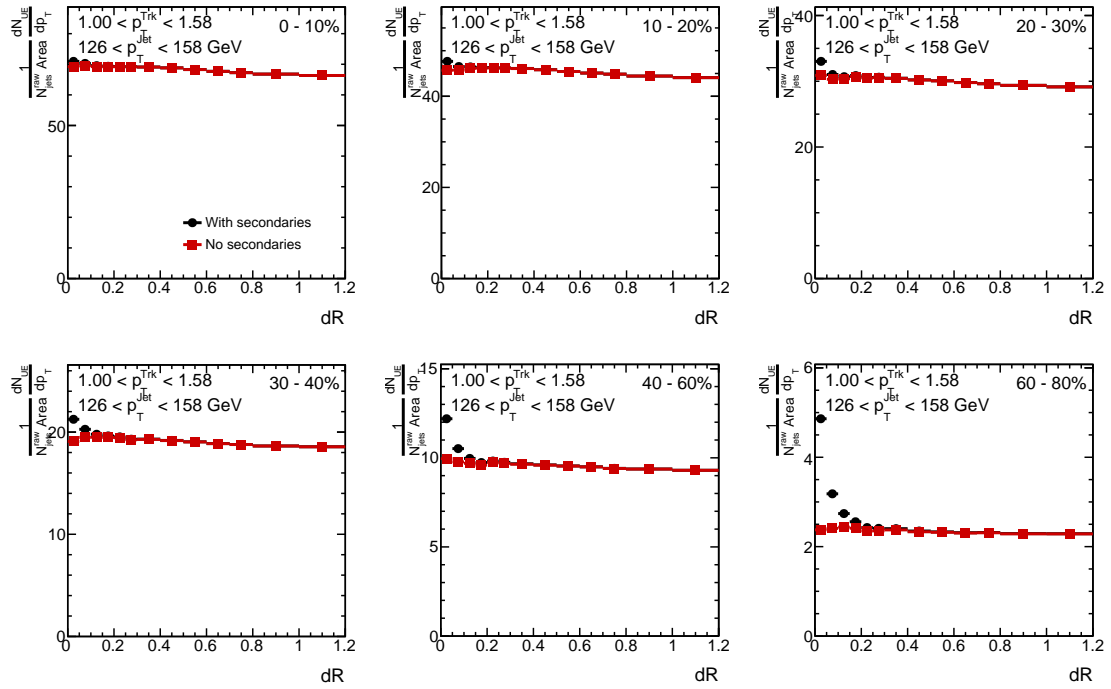


Figure 4.30: UE estimated from tracks which do not have an associated truth particle in jet with p_T from 126 to 158 GeV and for the lowest track p_T interval (1–1.58 GeV). The two different distribution shows the UE with and without the contribution from the secondary particles.

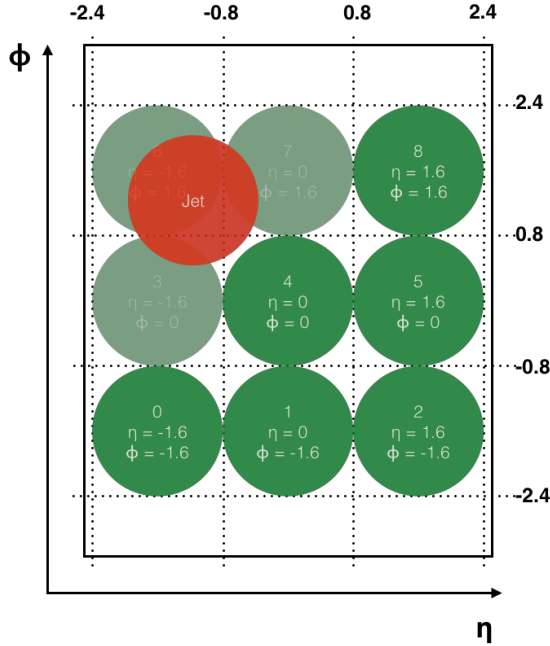


Figure 4.31: Illustration of the cone method to estimate the underlying event. Cones numbered 3, 6, and 7 are excluded based on the jet shown in red.

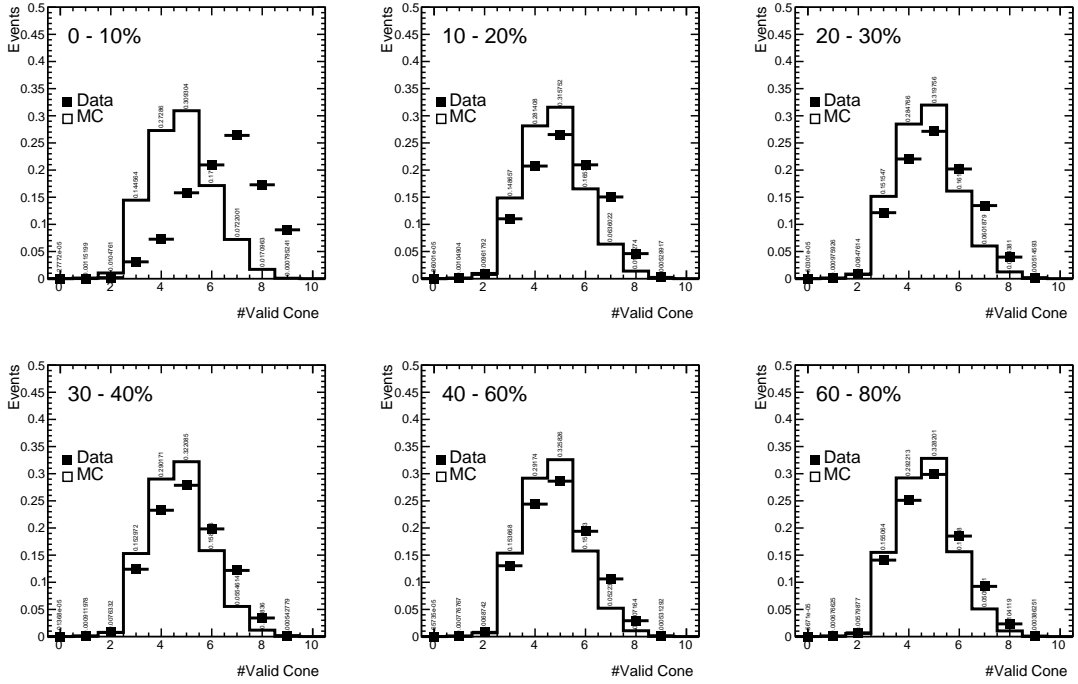


Figure 4.32: Fraction of events as a function of the number of cones used for the estimation of the underlying event.

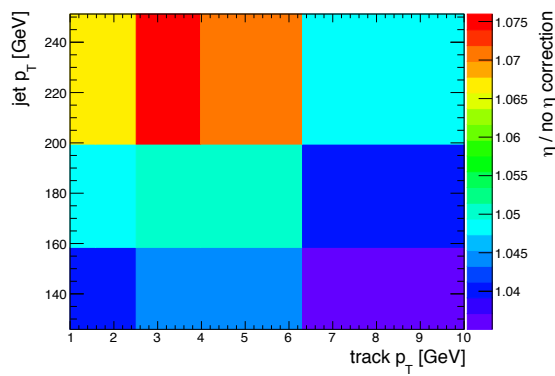


Figure 4.33: Ratio of the $N_{\text{ch}}^{\text{UE}}$ distributions with and without the correction for η dependence in the most central 0-10% Pb+Pb collisions, evaluated with a subset of the data (70k events).

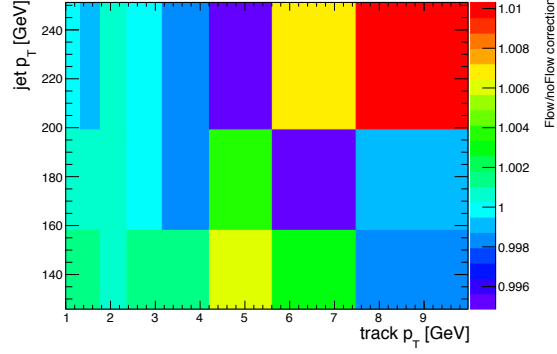


Figure 4.34: Ratio of the $N_{\text{ch}}^{\text{UE}}$ cone distributions with and without the correction for elliptic flow in the most central 0-10% Pb+Pb collisions, evaluated with a subset of the data (70k events).

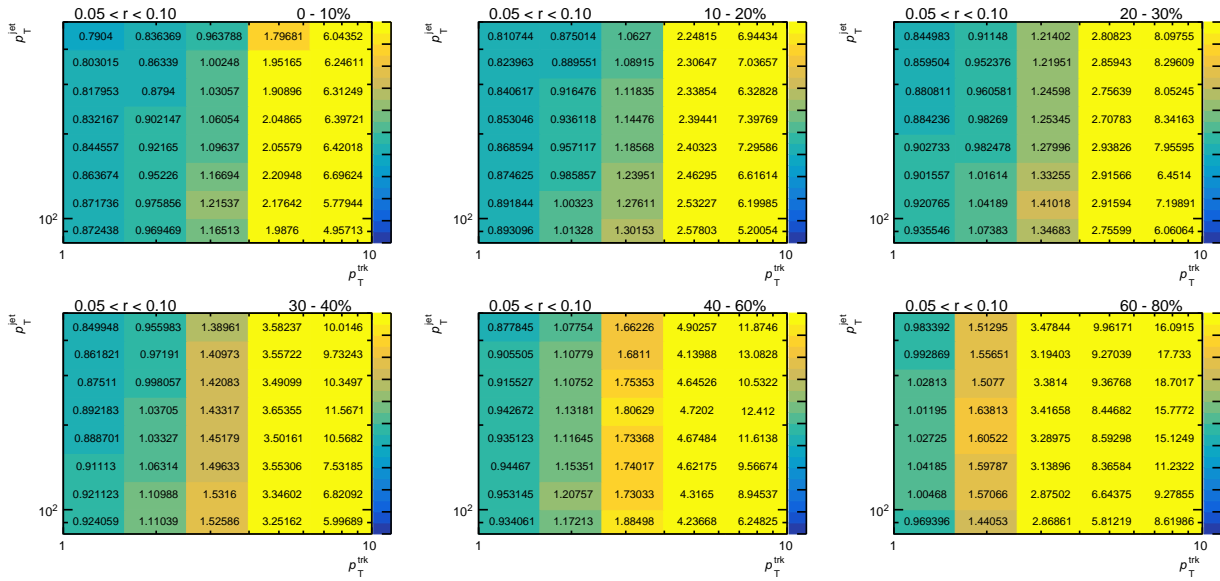


Figure 4.35: The multiplicative correction factors that correct for the correlation between the UE and the JER, fake and secondary particles in different centrality classes and $0.05 < r < 0.10$.

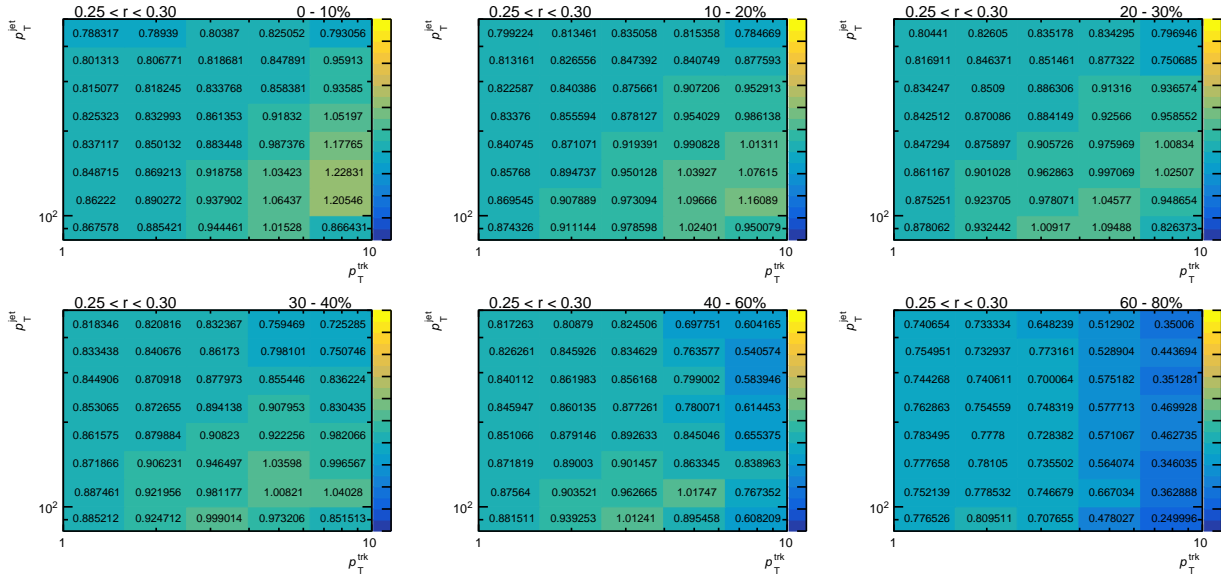


Figure 4.36: The multiplicative correction factors that correct for the correlation between the UE and the JER, fake and secondary particles in different centrality classes and $0.25 < r < 0.30$.

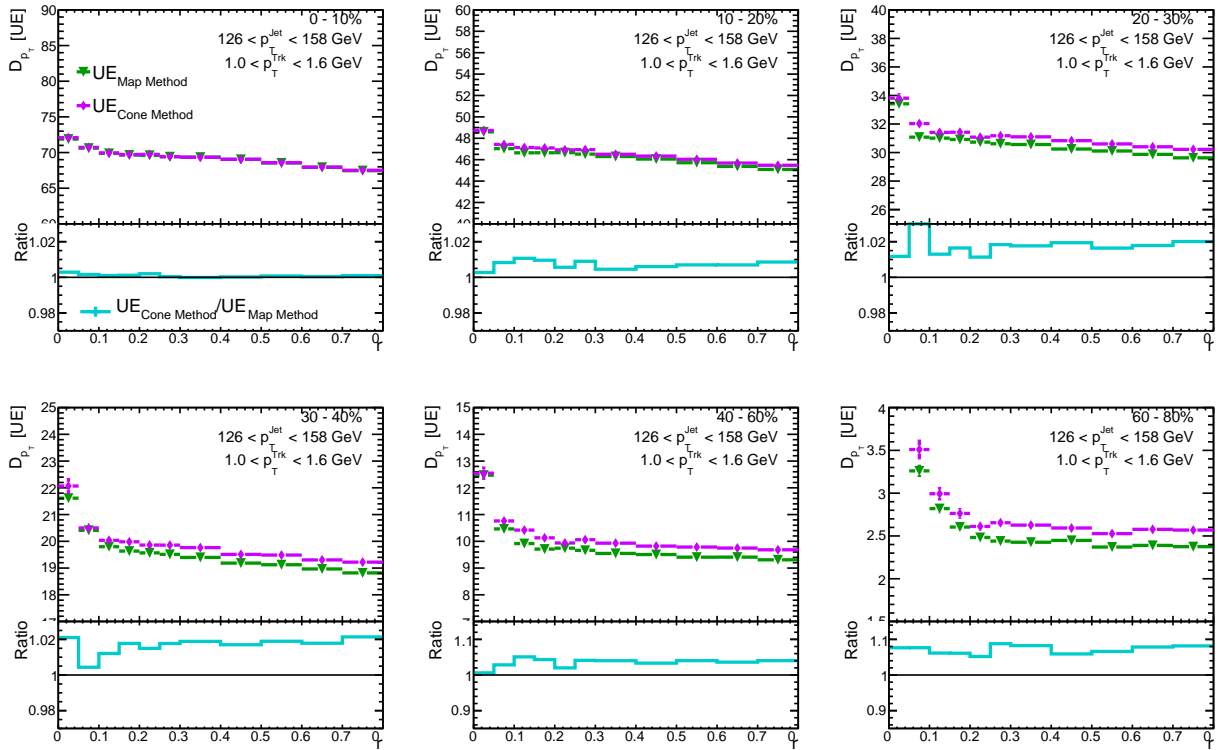


Figure 4.37: The difference between the cone method and the map method as a function for r for 0-10% Pb+Pb collisions, in 126-158 GeV jets, 1-1.6 GeV tracks.

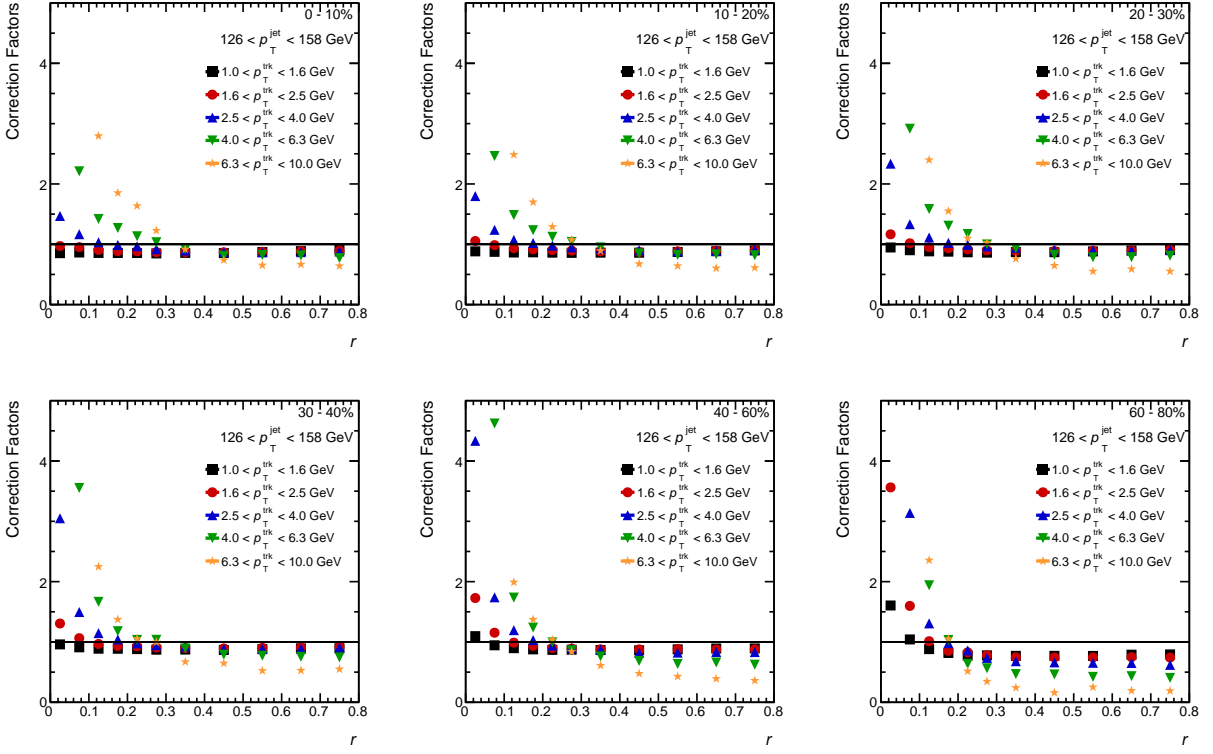


Figure 4.38: The multiplicative correction factors that correct for the correlation between the UE and the JER, fake and secondary particles in different centrality classes, as a function of r for $126 < p_T^{\text{jet}} < 158 \text{ GeV}$.

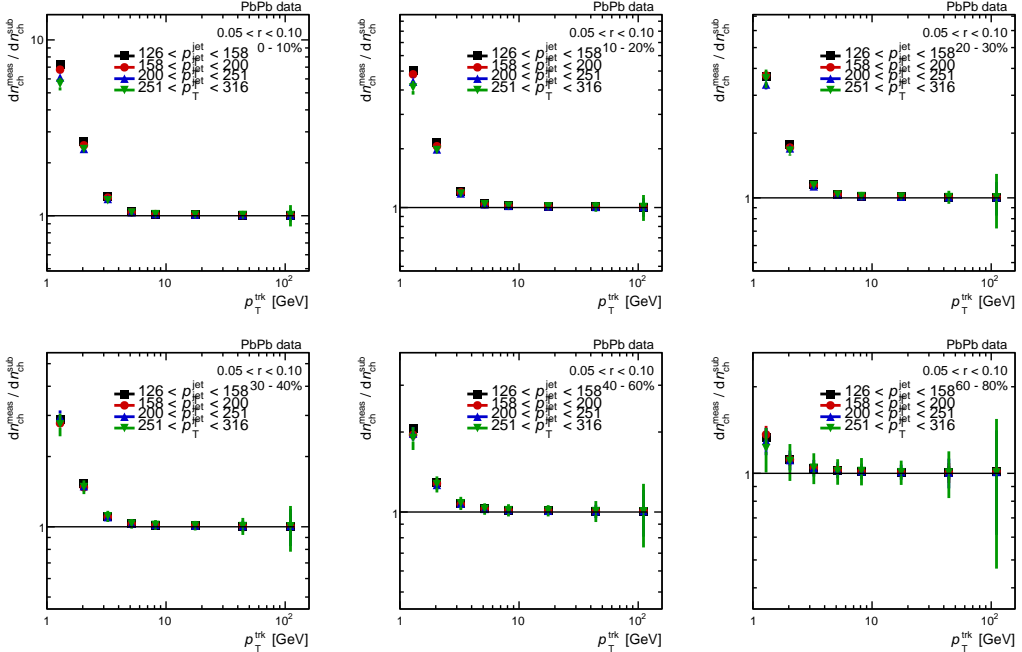


Figure 4.39: Ratio between the raw $D(p_T, r)$ distributions before and after the UE subtraction in different centrality classes and different jet p_T intervals for $0.05 < r < 0.10$.

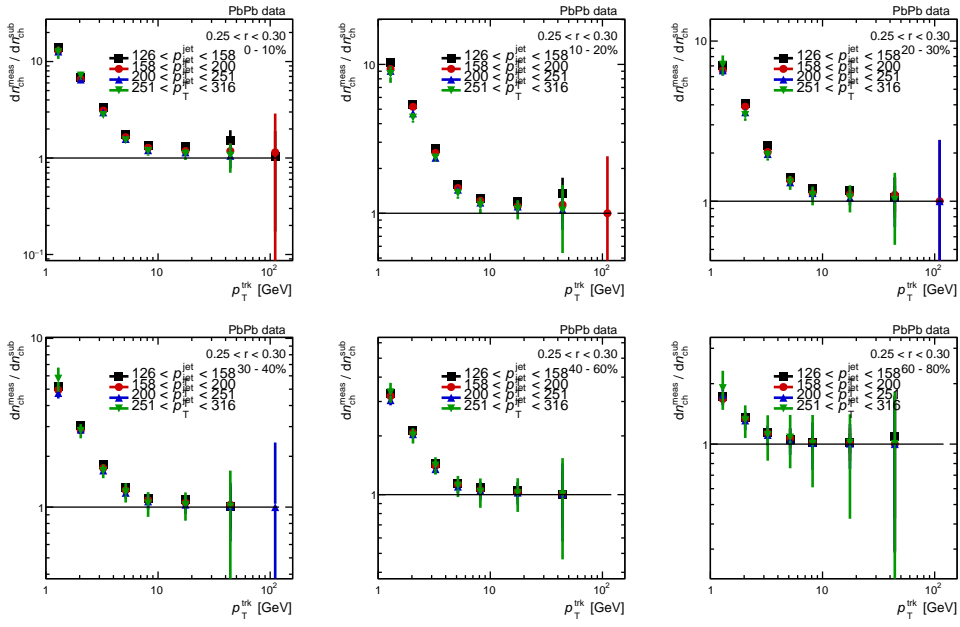


Figure 4.40: Ratio between the raw $D(p_T, r)$ distributions before and after the UE subtraction in different centrality classes and different jet p_T intervals for $0.25 < r < 0.30$.

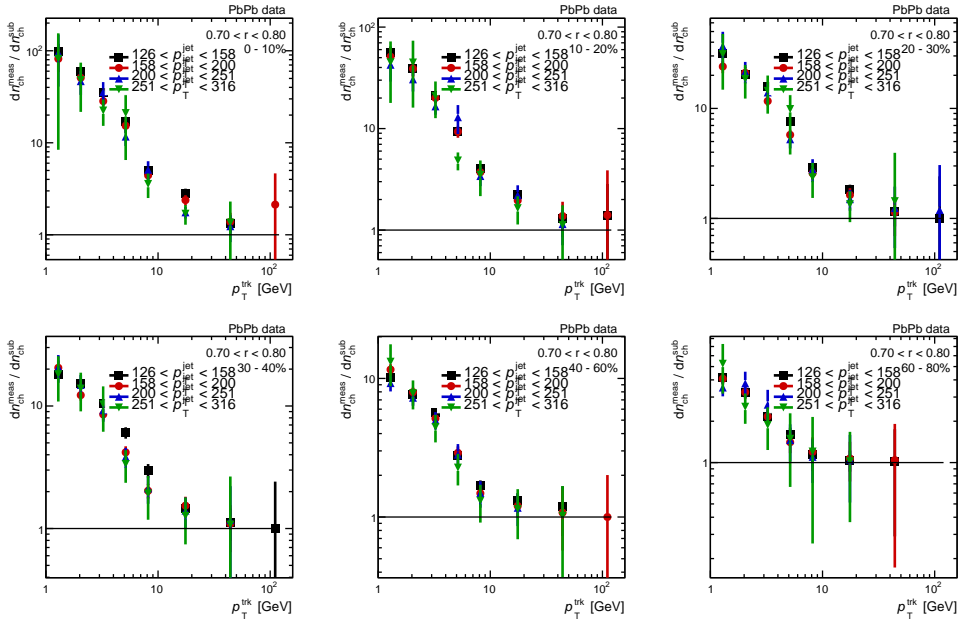


Figure 4.41: Ratio between the raw $D(p_T, r)$ distributions before and after the UE subtraction in different centrality classes and different jet p_T intervals for $0.70 < r < 0.80$.

4.5.7 Unfolding

Instrumental effects are corrected by an unfolding procedure. This analysis uses three separate unfolding procedures that are discussed in this section.

- One dimensional unfolding for the p_T^{jet} spectra for the normalization.
- Two dimensional Bayesian unfolding in p_T^{ch} and p_T^{jet} for jet p_T dependent yields of charged particles.
- Bin by bin correction for the jet and track position resolution.

To achieve better correspondence with the data, the response matrices for both the one and two dimensional unfolding are reweighed so that the distributions match the shapes in the reconstructed data.

One Dimensional Unfolding for Jet Spectra

The charged particle spectra need to be normalized by the number of jets in given jet p_T interval. Thus, the jet spectra needs to be corrected for bin migration due to the finite JER by unfolding procedure. The unfolding is done via a one dimensional Bayesian unfolding procedure with 4 iterations implemented as part of the RooUnfold [43] package. The pp and Pb+Pb MC samples are used to construct two dimensional response matrices in terms of $p_T^{\text{jet},\text{truth}}$ and $p_T^{\text{jet},\text{reco}}$. These matrices can be seen in Fig:4.42-4.43 and are evaluated separately for pp and in different centrality intervals for Pb+Pb collisions. The technical closure of this unfolding procedure (done using unreweighed response matrices to unfold the reconstructed jet spectra) is shown in Fig:4.44-4.45, as a function of p_T^{jet} for jets in the $|y| < 1.7$ region. A good recovery of the truth distribution is seen for both 1% for Pb+Pb and pp MC samples.

Two Dimensional Unfolding for Charged Particle Spectra

Observed correlation between the jet response in the detector and the jet fragmentation necessitates a two dimensional unfolding [13]. For example, gluon jets, which have in general a softer fragmentation function, are observed to have a lower energy response than quark jets [9]. The Global Sequential Calibration to the pp jet collections [44], reduces the fragmentation dependence to the JES, but these calibrations are not available for the HI jet collections used in this analysis.

We use the RooUnfold [43] implementation of the two dimensional iterative Bayesian unfolding [45] with 4 iterations. The MC Pb+Pb and pp samples are used to construct a 4-dimensional response matrix in $p_T^{\text{trk,Truth}}$, $p_T^{\text{jet,truth}}$, $p_T^{\text{trk,reco}}$, and $p_T^{\text{jet,reco}}$, shown in Fig:4.46-4.47. The response matrix A_{ijkl} describes the

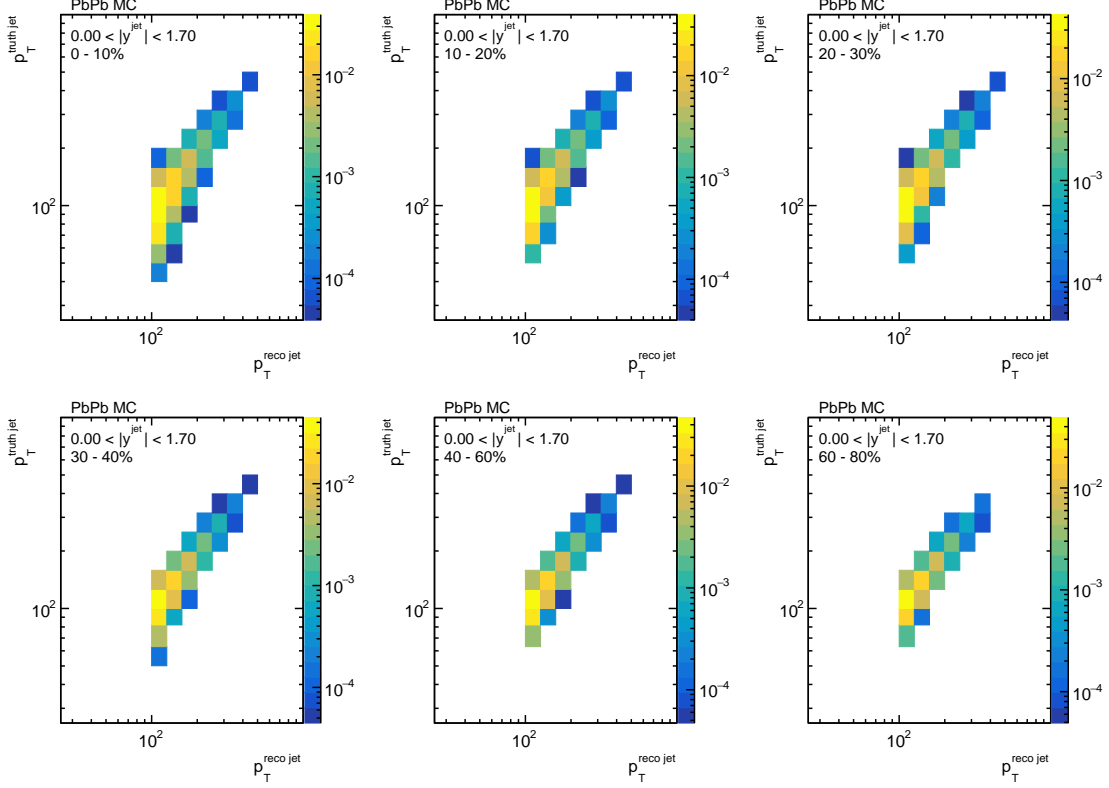


Figure 4.42: The response matrices in terms of $p_T^{\text{jet},\text{reco}}$ and $p_T^{\text{jet},\text{truth}}$ in the jet $|y| < 1.7$ region, in data overlay Pb+Pb MC samples. Each panel is a different centrality bin.

probability that event from the truth track p_T bin j and truth jet p_T bin l is found in reconstructed bin i,k :

$$\mu_{jl} = \sum_{i,k} A_{ijkl} x_{jl}^{\text{truth}}. \quad (4.12)$$

Bin-by-bin correction for Angular resolution

There is an additional unfolding procedure applied in this analysis to correct for the jet and the track position resolution that results in the migration in angular distance r . The migration is dominated by the poor jet angular resolution (Fig.4.11-4.12), since the track angular resolution (Fig.4.48-4.49) is very good.

The correction factors are derived using response matrices that correlate the reconstructed and truth angular distance r . These matrices are evaluated for different jet and track p_T in different centrality classes. Examples of the response matrices are shown in Fig 4.50 and Fig. 4.51 for Pb+Pb and pp MC samples. The bin-by-bin correction procedure is applied to $D(p_T, r)$ distribution unfolded to the particle level in terms of track and jet p_T by the two unfolding procedures discussed above. Thus, the correction factors for angular

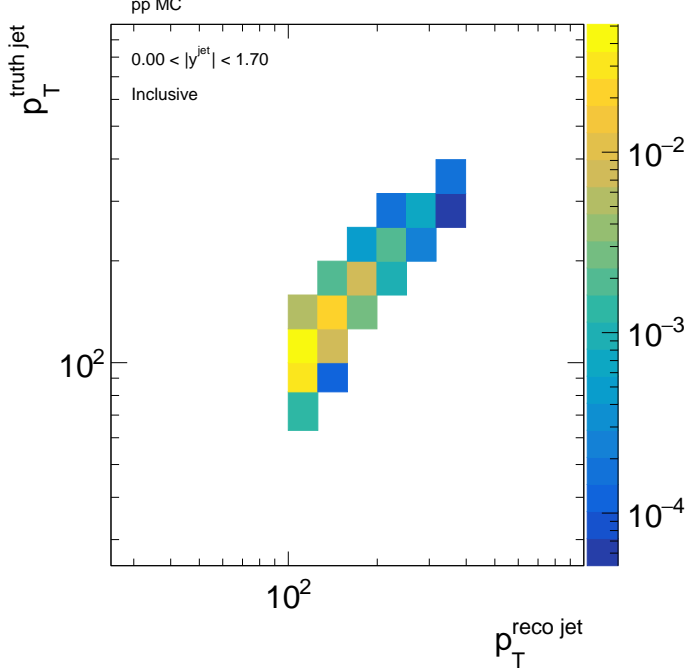


Figure 4.43: The response matrices in terms of $p_T^{\text{jet},\text{reco}}$ and $p_T^{\text{jet},\text{truth}}$ in the jet $y < 1.7$ region, in pp MC samples.

resolution were derived using the the reconstructed jets and tracks where the reconstructed jet and track p_T is replaced by the corresponding truth p_T . The bin-by-bin factors are then estimated as ratio of projections from the response matrices on the truth and reconstructed axis. These correction factors are shown in Fig. 4.52 and Fig. 4.53 for Pb+Pb and pp collisions as a function of r . The efficiency and purity of the unfolding procedure can be seen in the Fig.4.54-4.55.

The robustness of this correction can be validated by constructing $D(p_T, r)$ distributions using a coarser p_T binning (entire analysis chain is re-done) and comparing them to a summation of the individually unfolded narrow bins. This comparison can be seen in Fig.4.56, for $1 < p_T < 4$ GeV, $126 < p_T^{\text{jet}} < 158$ GeV, for 0-10% central Pb+Pb and pp collisions, and is seen to be unity.

It can be seen that these corrections become large at the edges of the jet cone for tracks that carry a significant fraction of the jet momentum. This is an artifact of the jet reconstruction algorithm, where a truth track near the edge of a truth jet will pull the reconstructed jet towards itself, causing a depletion of high p_T particles at the edge of the jet cone. This depletion can be seen in the distribution of truth charged particles in truth jets shown in Fig.4.57 and was also seen in [46]. These large factors result in a large non-closure near the jet edge for tracks carrying a significant momentum fraction of the jet. To exclude these effects, the results are only shown for tracks that show a closure of less than 5%.

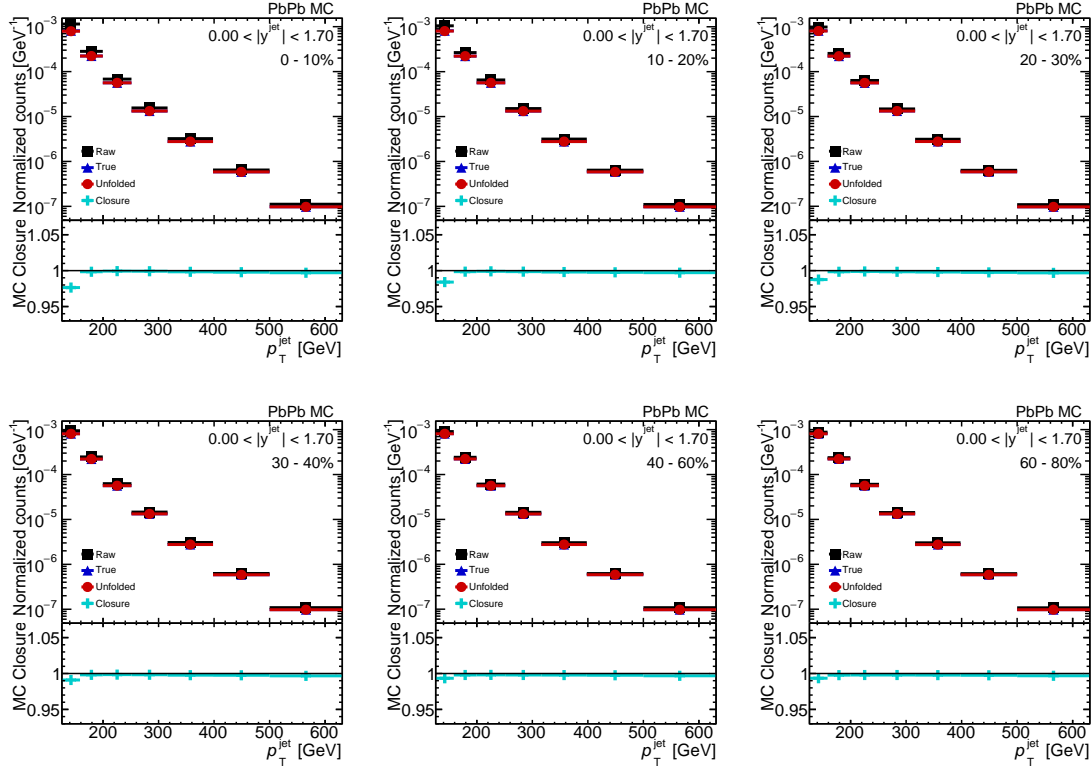


Figure 4.44: The jet spectra and MC closure as a function of p_T^{jet} in the jet $|y| < 1.7$ region, in data overlay Pb+Pb MC samples. The closure is seen to be well within 1%. Each panel is a different centrality bin.

The $D(p_T, r)$ distributions at various stages of the analysis in pp MC and data (Fig:4.58), and Pb+Pb MC and data (Fig:4.59-4.60) are also shown.

The MC closure of the charged particle spectra as a function of p_T in pp and data overlay Pb+Pb MC samples can be seen in Fig:4.61-4.62, and is well within 1% for low p_T particles.

4.6 Systematic Uncertainties

This section gives an overview of the sources of systematic uncertainties on the pp and Pb+Pb charged particle spectra associated with jet. The sources of systematic uncertainties in the measurement are the following and are further described below:

- Jet energy scale
- Jet energy resolution
- Track selection

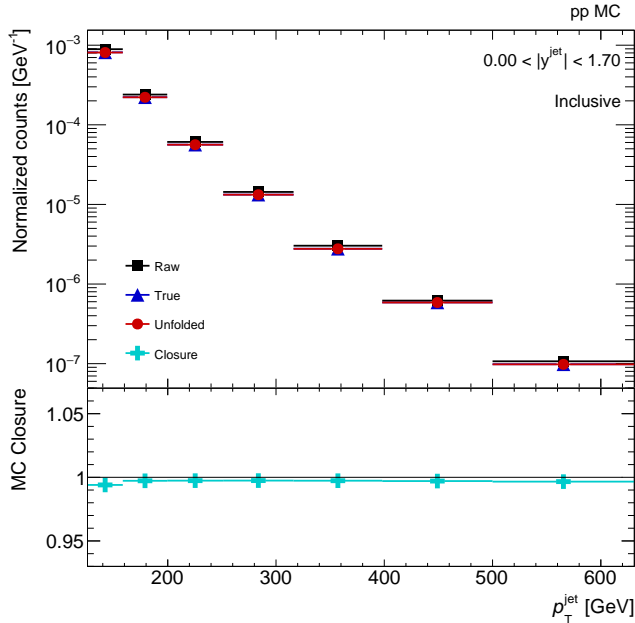


Figure 4.45: The jet spectra and MC closure as a function of p_T^{jet} in the jet $|\eta| < 1.7$ region, in pp MC samples. The closure is seen to be well within 1%.

- Truth track definition
- Detector material description in simulation
- Tracking in dense environments
- Fake track subtraction
- Track momentum
- Unfolding
- Underlying event contribution
- MC non-closure

The systematic uncertainties are evaluated separately for $D(p_T, r)$ distributions and for their ratios as a function of jet p_T for pp and $\text{Pb}+\text{Pb}$ collisions. For each systematic variation, the entire analysis procedure is repeated (including the 2D unfolding of the fragmentation functions as a function of p_T^{jet} , the 1D unfolding of the single p_T^{jet} spectrum and the bin-by-bin correction for position resolution). This is necessary because the jets are in both the 2D and the 1D unfolding procedures and must be treated in a consistent manner

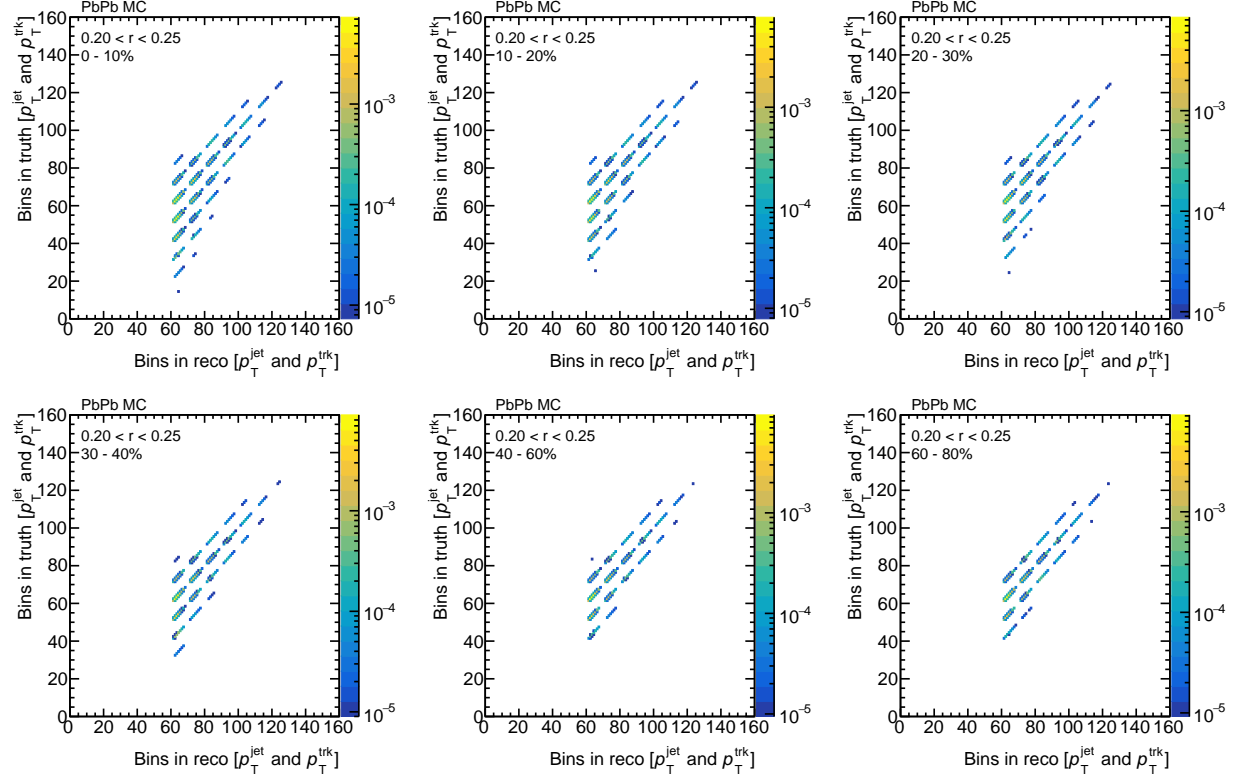


Figure 4.46: The response matrices in terms of $p_T^{\text{jet},\text{reco}}$, $p_T^{\text{jet},\text{truth}}$, $p_T^{\text{trk},\text{reco}}$, and $p_T^{\text{trk},\text{Truth}}$, for reconstructed track - reconstructed jet pairs, that have $0.20 < r < 0.25$, in data overlay Pb+Pb MC samples. Each panel is a different centrality bin.

throughout the analysis (e.g. a shift in the JES should shift jets in the fragmentation functions as a function of p_T^{jet} in the same manner that the single jet spectrum itself is shifted).

The systematic uncertainties on the $R_D(p_{T,r})$ distributions for a selection of track p_T ranges (1.0–1.6 GeV, 2.5–4.0 GeV, 6.3–10 GeV) in jets with p_T in the 126–158 GeV range are shown in Figure 4.63–4.64. The systematic uncertainties for other jet p_T interval as show in appendix ??.

4.6.1 Jet energy scale uncertainty

The uncertainty on the JES for heavy ion jets has two parts. The first is taken from pp JES uncertainties for EMTopo jets while the second is specific to the heavy ion jets and collision energies (for flavor related uncertainties). For the pp part we use the strongly reduced set of 4 nuisance parameters (in Scenario 1) as described in Ref. [47]. Nuisance parameters that are not applicable for HI jet collections (pileup, b-jets, flavor and MC non closure) are removed or replaced (flavor uncertainties). The heavy ion specific components are from the cross calibration [35] and the jet flavor uncertainties at 5.02 TeV [36]. For each component of the

variation the response matrices are regenerated with the shifted p_T^{jet} :

$$p_T^{*,\text{reco}} = p_T^{\text{reco}}(1 \pm U^{\text{JES}}(p_T, \eta)). \quad (4.13)$$

The data is then re-unfolded with these response matrices and the variation in the fragmentation functions is taken as the systematic uncertainty.

The centrality dependent uncertainty on the JES was evaluated by shifting the jet p_T of all measured jets up and down by shift between 0% and 0.5%. The magnitude of the shift depends on the centrality in the way that the uncertainty on the jet p_T is 0.5% in 1% most central collisions and than linearly decreases to 0% in 60% peripheral bin. The size of the shift reflects the uncertainty on the JES evaluated as using the r -track study where the sum of p_T of the tracks associated to a reconstructed jet is compared to the reconstructed jet p_T in ratio that is than compared between PbPb data and MC [22, 33].

4.6.2 Jet energy resolution

To account for systematic uncertainties due to disagreement between the jet energy resolution in data and MC, the unfolding procedure was repeated with a modified response matrix. The matrix was generated by repeating the MC study with modifications to the Δp_T for each matched truth-reconstructed jet pair.

The procedure to generate modified migration matrices follows the standard procedure applied in p+p jet measurements and is used for both the pp and Pb+Pb collisions. The `JetEnergyResolutionProvider` tool [48] was used to retrieve uncertainty on the fractional resolution, $\sigma_{\text{JER}}^{\text{syst}}$ as a function of jet p_T and η . An additional HI jet specific uncertainty from the cross calibration of the HI jet collections [35] is applied to jets in both pp and Pb+Pb collisions. The full JER uncertainty on 2015 pp data is shown also in Ref. [49]

The jet p_T^{reco} was then smeared by

$$p_T^{*,\text{reco}} = p_T^{\text{reco}} \times \mathcal{N}(1, \sigma_{\text{JER}}^{\text{eff}}), \quad (4.14)$$

where $\mathcal{N}(1, \sigma_{\text{JER}}^{\text{eff}})$ is the normal distribution with the effective resolution $\sigma_{\text{JER}}^{\text{eff}} = \sqrt{(\sigma_{\text{JER}} + \sigma_{\text{JER}}^{\text{syst}})^2 - \sigma_{\text{JER}}^2}$.

4.6.3 Track selection and efficiency

Track selection This uncertainty was estimated by tightening the tracking cuts by adding the cuts on the significance of d_0 and z_0 as described in the Section 4.5.2. The entire analysis is redone with these track selections (including re-deriving the tracking efficiencies and the $\eta - \phi$ maps for the UE estimation) and the difference from the nominal analysis is taken as the systematic uncertainty.

Truth track definition This uncertainty quantifies robustness of the matching of reconstructed to truth particles. The uncertainty is taken as a difference in the final results obtained with $MCprob > 0.3$ and results obtained with $MCprob > 0.5$. This systematic included a re-derivation of the $\eta - \phi$ maps for UE estimation. The change in tracking efficiency is negligible.

Detector material description in simulation The uncertainty on the inner detector material varies with p_T^{ch} and η^{ch} from 0.5% to 2.0% [37] on the efficiency correction. This systematic also included a re-derivation of the $\eta - \phi$ maps for UE estimation.

Tracking in dense environments There is a 0.4% uncertainty on the efficiency due to tracking in dense environments (the core of the jet) [37]. This systematic also included a re-derivation of the $\eta - \phi$ maps for UE estimation.

Fake rate and secondaries The uncertainty on the rate of fake tracks and secondaries is taken to be 30% independent of p_T^{ch} and η^{ch} [37, 50]. This uncertainty is conservatively symmetrized.

Uncertainty on the track momentum To account for a possible miss-alignment in pp and Pb+Pb data, the reconstructed p_T of each track (corrected first as described in section 4.5.3) was changed according to [38]:

$$p_T \rightarrow p_T \times (1 + q \times p_T \delta_{\text{sagitta}}(\eta, \phi))^{-1}, \quad (4.15)$$

where q is charge of the track and $\delta_{\text{sagitta}}(\eta, \phi)$ is uncertainty on the track curvature. The uncertainty derived for 5.02 TeV pp and Pb+Pb data is included in InDetTrackSystematicsTools-00-00-19. Due to statistical origin of the uncertainty the resulting systematic uncertainty is symmetrized. This systematic also included a re-derivation of the $\eta - \phi$ maps for UE estimation.

4.6.4 Systematic uncertainty due to unfolding

The systematic uncertainty associated with the unfolding is connected with the sensitivity of the unfolding procedure to the choice of the input distributions. The systematic is evaluated by generating response matrices from the MC distributions without the reweighting factor that is used to match the jet spectrum and $D(p_T, r)$ distributions in data, and then unfolding the data using these response matrices. This has minimal effect on track p_T because of the good track momentum resolution in the kinematic region of interest. The uncertainty is evaluated by comparing the nominal result with the un-reweighted result, and is considered to be uncorrelated between Pb+Pb and pp .

4.6.5 Systematic uncertainty due to the UE event subtraction

The systematic uncertainty associated with the estimation of the UE has two main components: one is the statistical uncertainty on the $\eta - \phi$ maps used in the map method (described in section 4.5.6) , and the other is the comparison of the map method to the alternative cone method (discussed in section 4.5.6. More details on the cone method can be found in Ref. [13]. The contributions of both components to the underlying event uncertainty can be seen in Fig.4.65, with the uncertainty from the map statistic dominating in central collisions (the uncertainty on the underlying event convolutes with the signal to background ratio to produce the uncertainty on the charged particle spectra.)

Uncertainty from map statistic: The $\eta - \phi$ maps used in the estimation of the underlying event are sparsely populated for high track p_T and high p_T^{jet} , and are susceptible to statistical fluctuations. To take this into account, 100 pseudo-experiments are conducted to re-estimate the set of maps, with a bin-by-bin gaussian variation where the mean and standard deviation were taken to be the bin content and bin error from the nominal set of maps. The distribution of the relative difference between each estimation of the shifted underlying event and the nominal value ($\delta(\text{UE}) = \text{GausWidth}(\text{UE}_i - \text{UE}_{\text{nominal}}/\text{UE}_{\text{nominal}})$) is fit to a gaussian, and the width is taken to be the systematic uncertainty. This uncertainty is symmetrized to be conservative. A few examples of the distribution of normalized relative differences can be seen in Fig. 4.66. The size of the systematic from this can be seen in Fig.4.67.

Uncertainty from cone method: The difference between the UE from the two methods is discussed in section 4.5.6 and is shown in Fig. 4.37. The effect of the different UE estimation methods on the charged particle spectra is seen in Fig.4.68. This uncertainty is conservatively symmetrized. While the absolute size of the uncertainty on the UE is typically small, the small signal-to-background ratio makes this the dominant systematic uncertainty in central collisions for lowest p_T tracks and large r .

4.6.6 MC non-closure

To make sure that all the sources of systematic uncertainties were covered, the systematic uncertainty from the non closure in the MC was also evaluated. It was calculated using the technical closure (done using non-reweighed response matrices) between the fully corrected and reconstructed charged particle distributions in MC to the charged particle distributions evaluated at the truth level. This uncertainty can be considered a measure of unknowns in the analysis, but it also includes fluctuations due to the finite statistics in the MC which are used to evaluate it (especially in high p_T^{ch} regions of the analysis. The non-closure can be seen in

Fig. 4.69). The systematic uncertainty is taken to be uncorrelated between Pb+Pb and pp

4.6.7 Correlations between the systematic uncertainties in Pb+Pb and pp collisions

Due to the common analysis and reconstruction procedure, and detector conditions, the systematic uncertainties are correlated between the pp and Pb+Pb collisions in most cases. Table 4.4 summarizes correlations between pp and Pb+Pb and also point-to-point correlations of individual distributions. The unfolding uncertainty is uncorrelated between the two systems because it comes from the sensitivity of the unfolding to the starting MC distribution. In Pb+Pb collisions where the fragmentation is modified by the presence of the QGP, this sensitivity could be different than in pp collisions where the fragmentation functions are quite similar to those in PYTHIA8 [14]. The impact of the modification of the fragmentation process in Pb+Pb compared to pp and MC simulations is account for in the HI specific data-driven and centrality dependent uncertainty on the JES.

uncertainty	pp and Pb+Pb correlated	point-to-point correlated	one/two sided or symmetrized
JES (pp)	yes	yes	two sided
JES (HI)	no	yes	two sided
JER	yes	yes	symmetrized
Track selection	yes	yes	one sided
Truth track definition	yes	yes	one sided
Material	yes	yes	one sided
Dense environment	yes	yes	one sided
Fake rate	yes	yes	symmetrized
Track momentum	yes	no	two sided
Unfolding	no	yes	symmetrized
UE subtraction	no	yes	symmetrized
MC non-closure	no	no	symmetrized

Table 4.4: Summary of correlation of different systematic uncertainties.

In the case where the systematic uncertainties are correlated, we evaluate $R_{D(p_T,r)}$ ratios using the systematic variation from the nominal distributions in both pp and Pb+Pb. The variation in the ratio is used as the systematic uncertainty. The variations in the ratios are summed in quadrature to get the total systematic uncertainty on the ratio.

4.7 Results

The $D(p_T, r)$ distributions are studied as a function of p_T^{jet} for pp data and Pb+Pb collisions with different centralities. Ratios and differences between $D(p_T, r)$ distributions in Pb+Pb and pp collisions are evaluated to explore the interplay between the hot and dense matter and the parton shower.

The $D(p_T, r)$ distributions evaluated in pp and Pb+Pb collisions for $126 < p_T^{\text{jet}} < 158$ GeV are shown in Figure 4.70. The distributions exhibit a difference in shape between Pb+Pb and pp collisions, with the Pb+Pb distributions being broader at low p_T ($p_T < 4$ GeV) and narrower at high p_T ($p_T > 4$ GeV) in 0–10% central collisions. This modification is centrality dependent and is smaller for peripheral Pb+Pb collisions.

In order to quantify the differences seen in Figure 4.70, ratios of the $D(p_T, r)$ distributions in Pb+Pb collisions to those measured in pp collisions for $126 < p_T^{\text{jet}} < 158$ GeV and $200 < p_T^{\text{jet}} < 251$ GeV jets are presented in Figure 4.71. They are shown as a function of r for different p_T and centrality selections. In 0–10% central collisions, $R_{D(p_T, r)}$ is greater than unity for $r < 0.7$ for charged particles with p_T less than 4.0 GeV in both jet selections. For these particles, the enhancement of yields in Pb+Pb collisions compared to those in pp collisions grows with increasing r up to approximately $r = 0.3$, with $R_{D(p_T, r)}$ reaching up to two for $1.0 < p_T < 2.5$ GeV. The value of $R_{D(p_T, r)}$ is approximately constant for r in the interval 0.3–0.6 and decreases for $r > 0.6$. For charged particles with $p_T > 4.0$ GeV, $R_{D(p_T, r)}$ shows a depletion outside the jet core for $r > 0.05$. The magnitude of this depletion increases with increasing r up to $r = 0.3$ and is approximately constant thereafter. The observed behavior inside the jet cone, $r < 0.4$, agrees with the measurement of the inclusive jet fragmentation functions [13, 51], where yields of fragments with $p_T < 4$ GeV are observed to be enhanced and yields of charged particles with intermediate p_T are suppressed in Pb+Pb collisions compared to those in pp for collisions. For 30–40% mid-central collisions, the enhancement of particles with $p_T < 4.0$ GeV is similar to that in the most central collisions, however the depletion of particles with $p_T > 4.0$ GeV is not as strong. For 60–80% peripheral collisions, $R_{D(p_T, r)}$ has no significant r dependence and the values of $R_{D(p_T, r)}$ are within approximately 50% of unity.

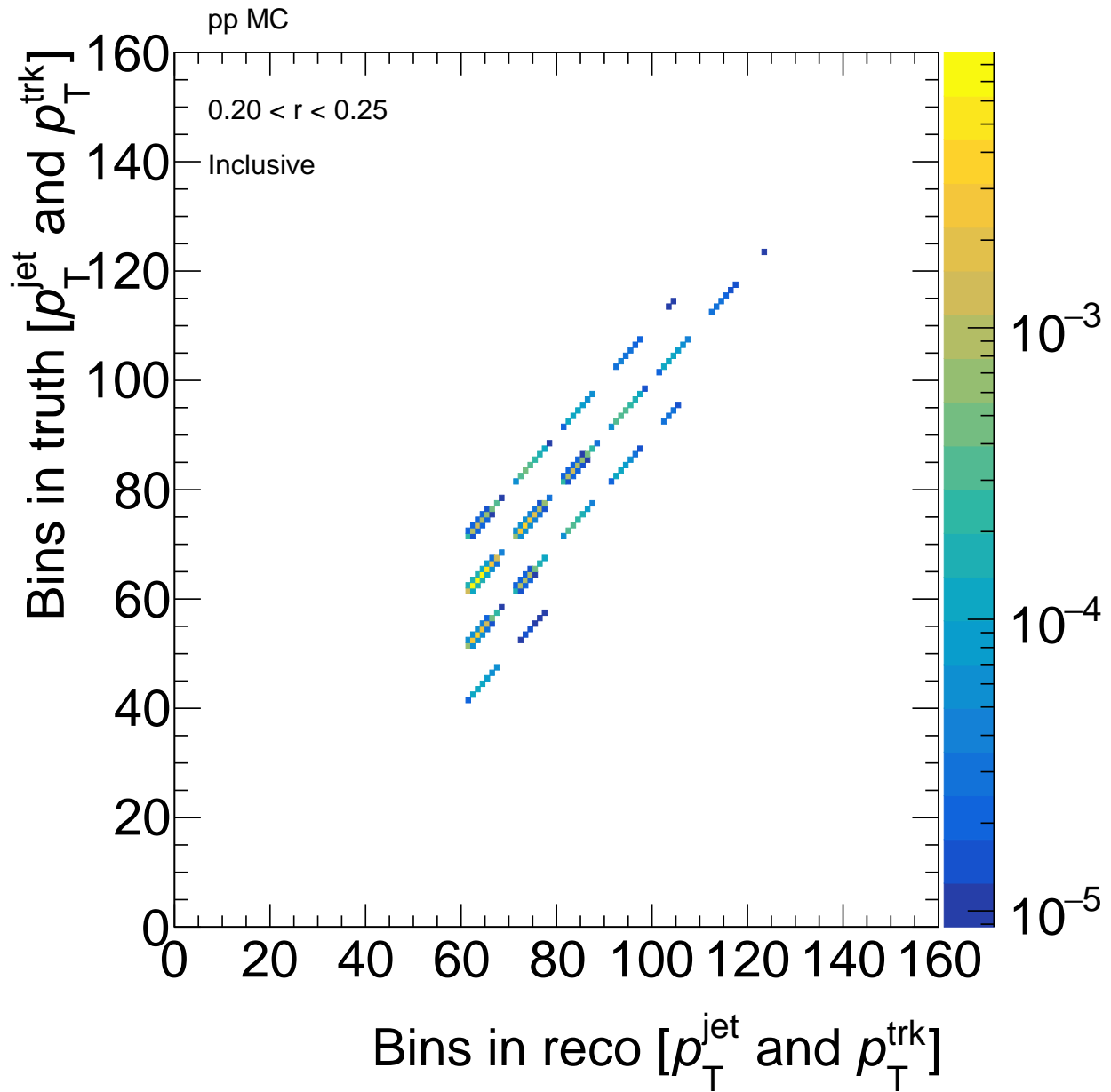


Figure 4.47: The response matrix in terms of $p_T^{\text{jet,reco}}$, $p_T^{\text{jet,truth}}$, $p_T^{\text{trk,reco}}$, and $p_T^{\text{trk,Truth}}$, for reconstructed track - reconstructed jet pairs, that have $0.20 < r < 0.25$, in pp MC samples

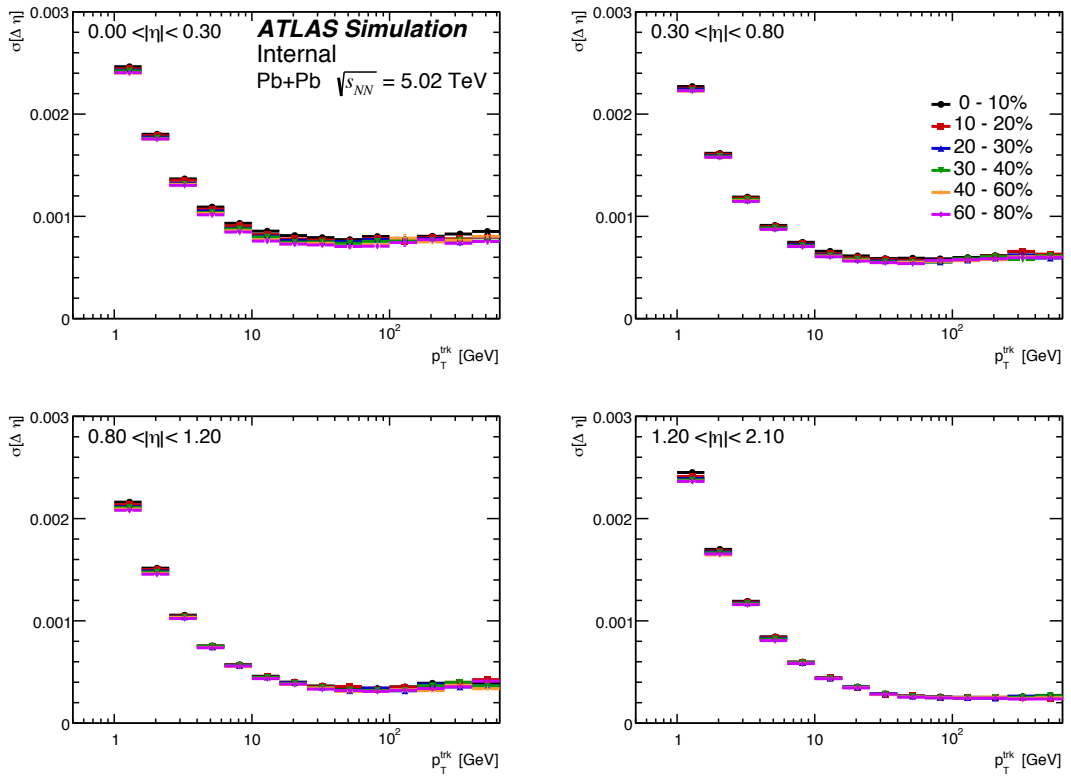


Figure 4.48: The η resolution of the tracker in different η bins for data overlay Pb+Pb MC samples. The different curves are different centralities, and it can be seen that there is no centrality dependence.

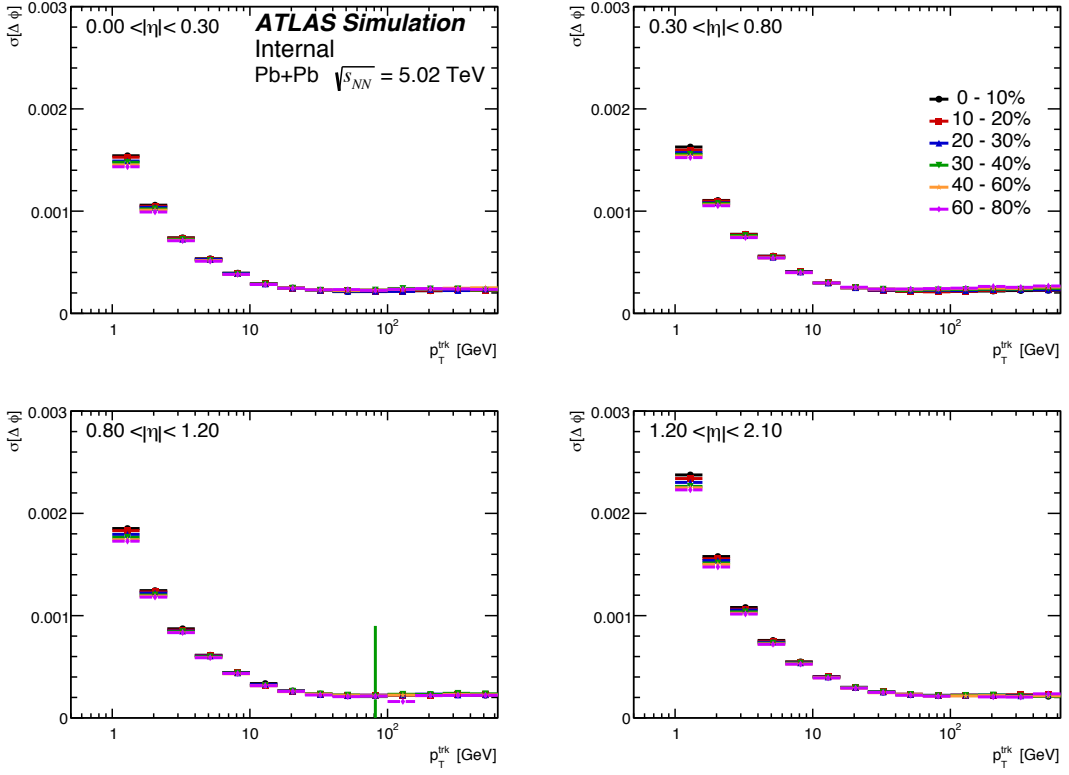


Figure 4.49: The ϕ resolution of the tracker in different ϕ bins for data overlay Pb+Pb MC samples. The different curves are different centralities, and it can be seen that there is no centrality dependence.

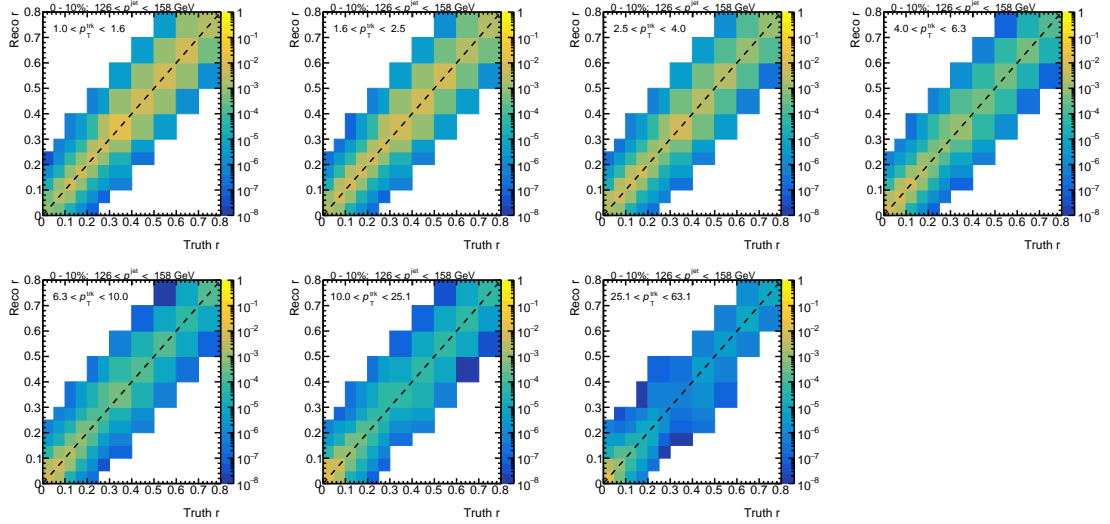


Figure 4.50: The response matrix for the bin by bin correction applied to the unfolded charged particle spectra. This accounts for the jet position resolution. Each panel is a different p_T^{ch} bin, for $126 < p_T^{\text{jet}} < 158$ GeV jets, in central collisions from data overlay Pb+Pb MC samples

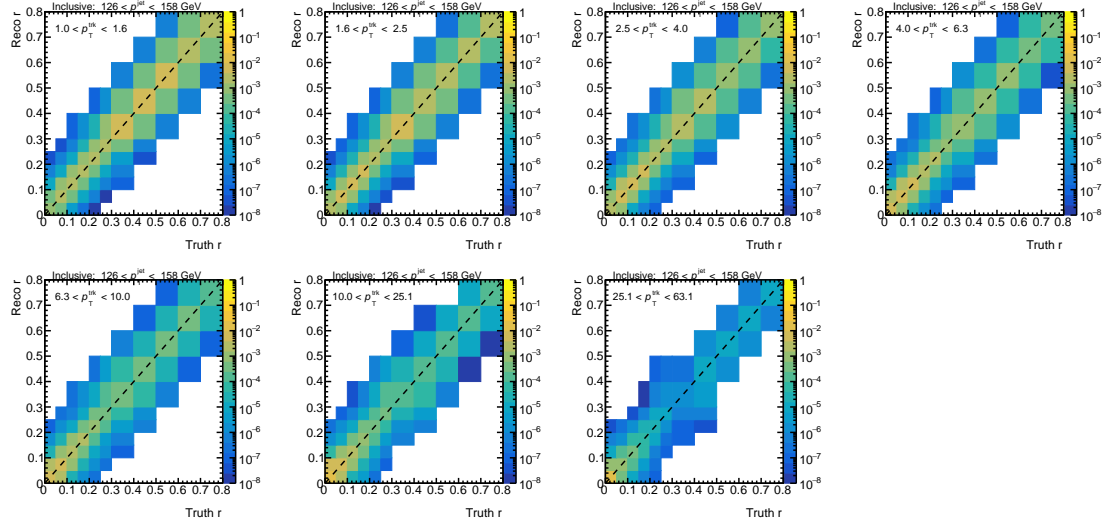


Figure 4.51: The response matrix for the bin by bin correction applied to the unfolded charged particle spectra. This accounts for the jet position resolution. Each panel is a different p_T^{ch} bin, for $126 < p_T^{\text{jet}} < 158$ GeV jets, from pp MC samples

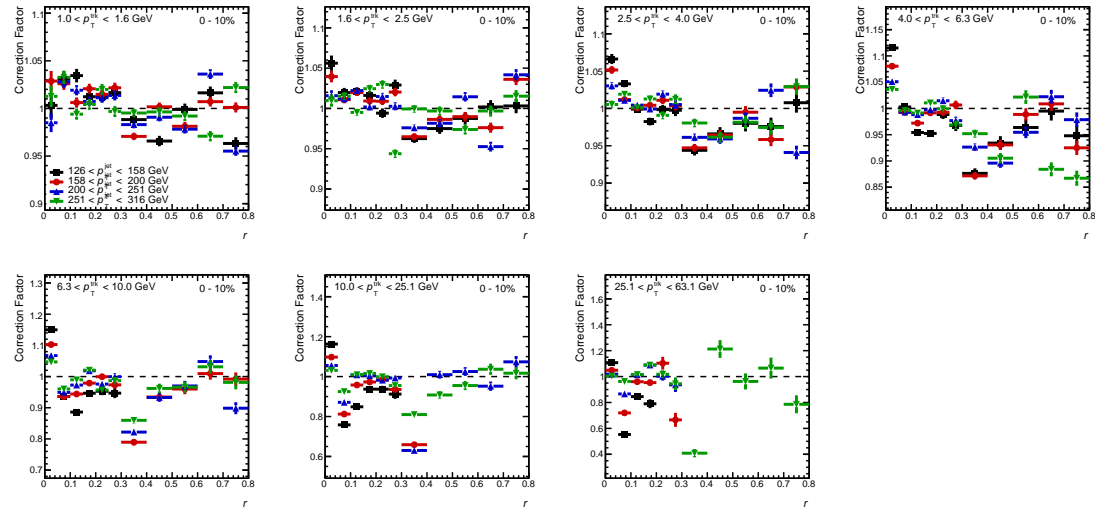


Figure 4.52: The correction factors applied to the unfolded charged particle spectra, shown for the most central Pb+Pb collisions, as a function of r , with each panel showing a different track p_T bin, and each curve showing a different p_T^{jet} range. These factors correct for the jet position resolution in Pb+Pb collisions.

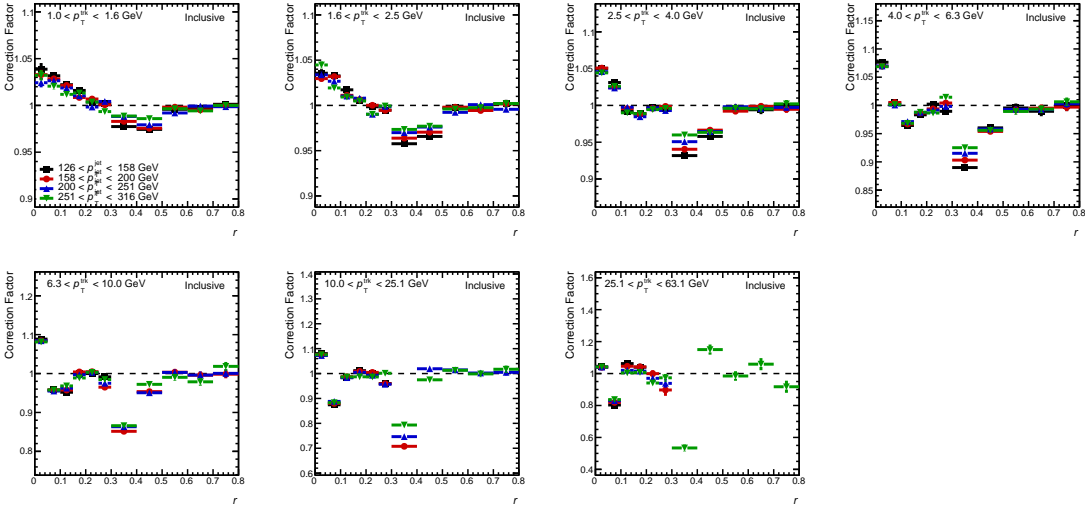


Figure 4.53: The correction factors applied to the unfolded charged particle spectra in pp collisions, as a function of r , with each panel showing a different track p_T bin, and each curve showing a different p_T^{jet} range. These factors correct for the jet position resolution in pp collisions.

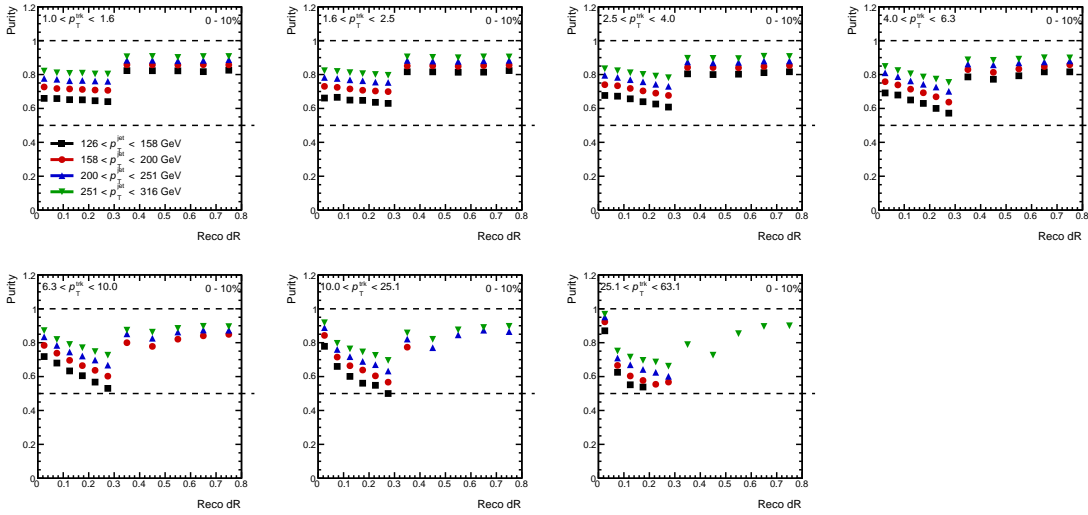


Figure 4.54: The purity of the bin-by-bin unfolding factors used to correct for the angular resolution for different p_T^{ch} ranges tracks (in different panels), shown as a function of r for different p_T^{jet} ranges, in the most central 0–10% $\text{Pb}+\text{Pb}$ collisions.

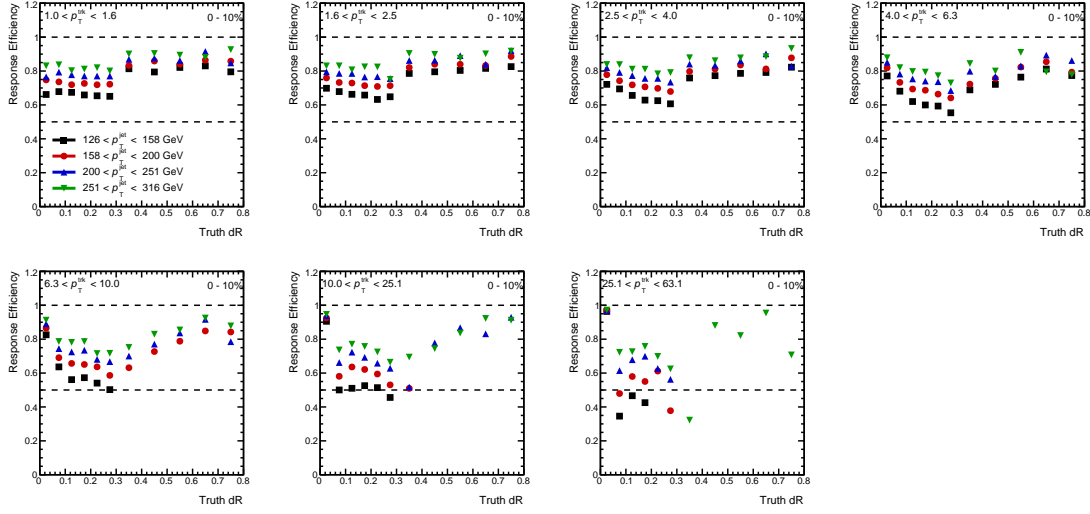


Figure 4.55: The efficiency of the bin-by-bin unfolding factors used to correct for the angular resolution for different p_T^{ch} ranges tracks (in different panels), shown as a function of r for different p_T^{jet} ranges, in the most central 0–10% Pb+Pb collisions.

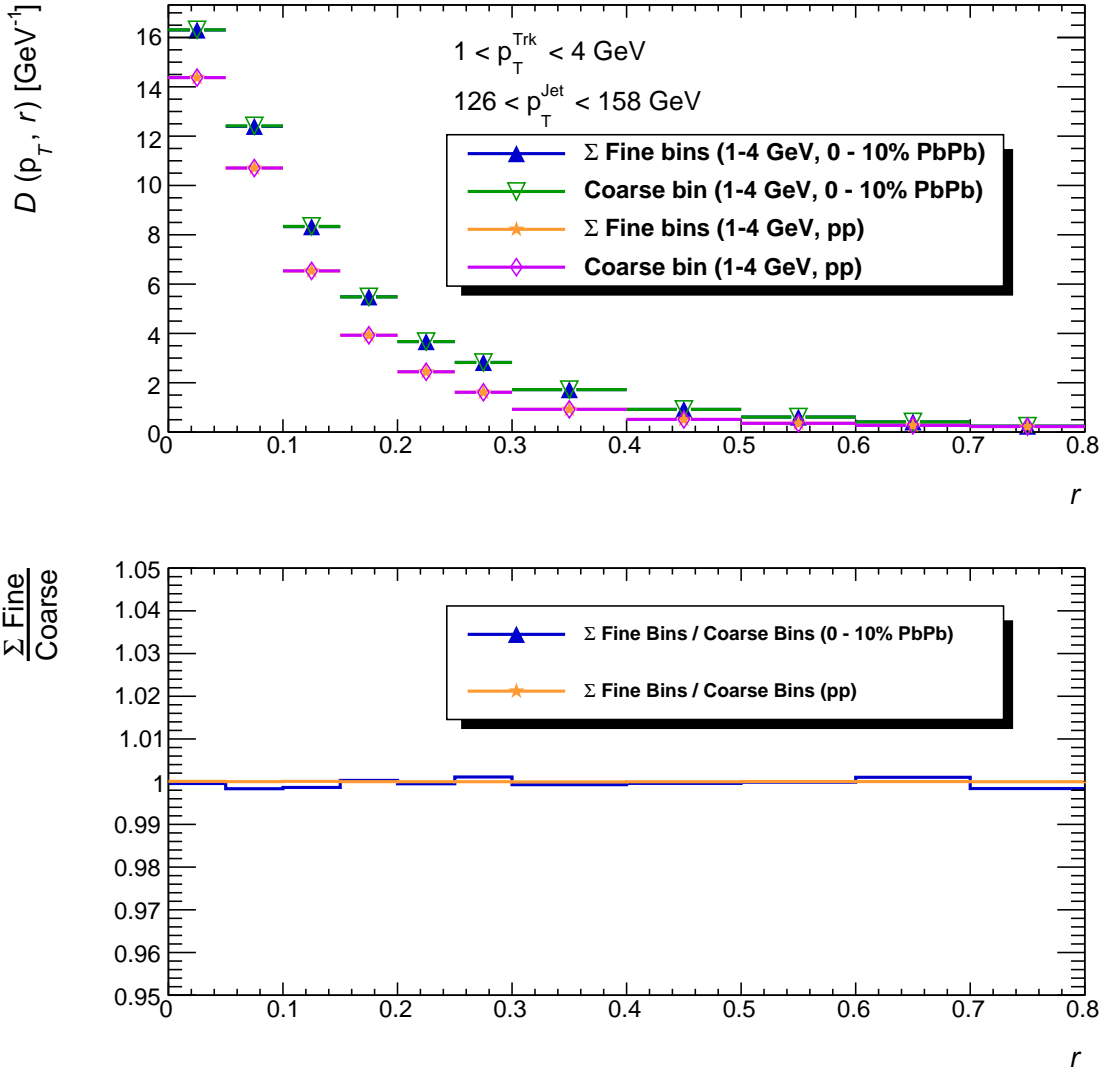


Figure 4.56: The $D(p_T, r)$ distributions in pp and $0-10\%$ central Pb+Pb , constructed using a single bin from $1-4$ GeV (merging the first three p_T bins in this analysis) compared to the $D(p_T, r)$ distributions constructed by adding up the bins individually: $1-1.6$ GeV, $1.6-2.5$ GeV and $2.5-4$ GeV. This comparison tests the robustness of the angular bin by bin correction and its dependence on the width of the p_T bins.

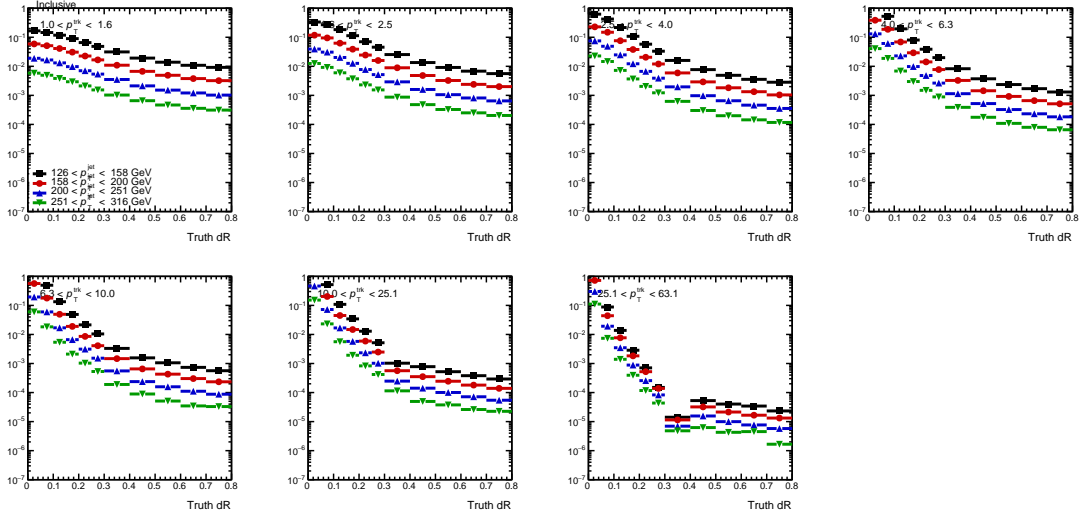


Figure 4.57: The distribution of truth charged particles in truth jets for different track p_T ranges and p_T^{jet} ranges in pp collisions. It can be seen that there is a kink in the distribution at the jet edge for high p_T tracks.

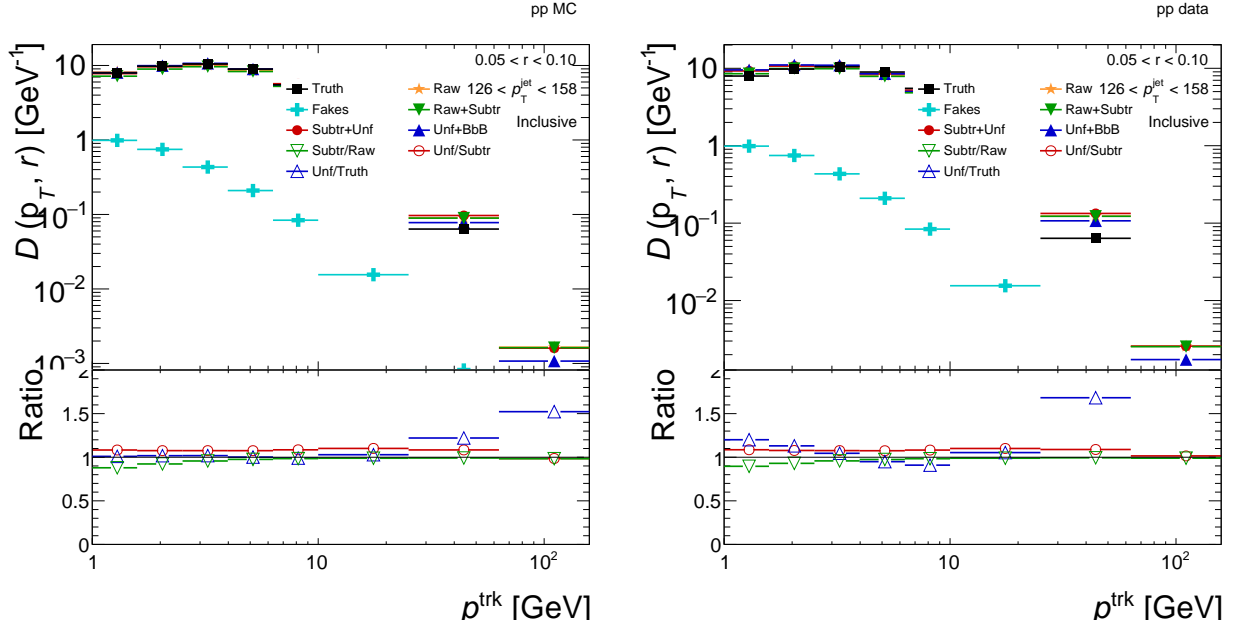


Figure 4.58: The evolution of the $D(p_T, r)$ distributions for pp MC (left) and data (right) as various corrections are applied. The spectra is shown for tracks with $0.05 < \Delta r < 0.10$ away from the jet axis, for $126 < p_T^{\text{jet}} < 158$ GeV. The ratios showing the effect of the unfolding and bin by bin corrections (left and right), as well as the MC closure (left) are shown in the lower half of the panels.

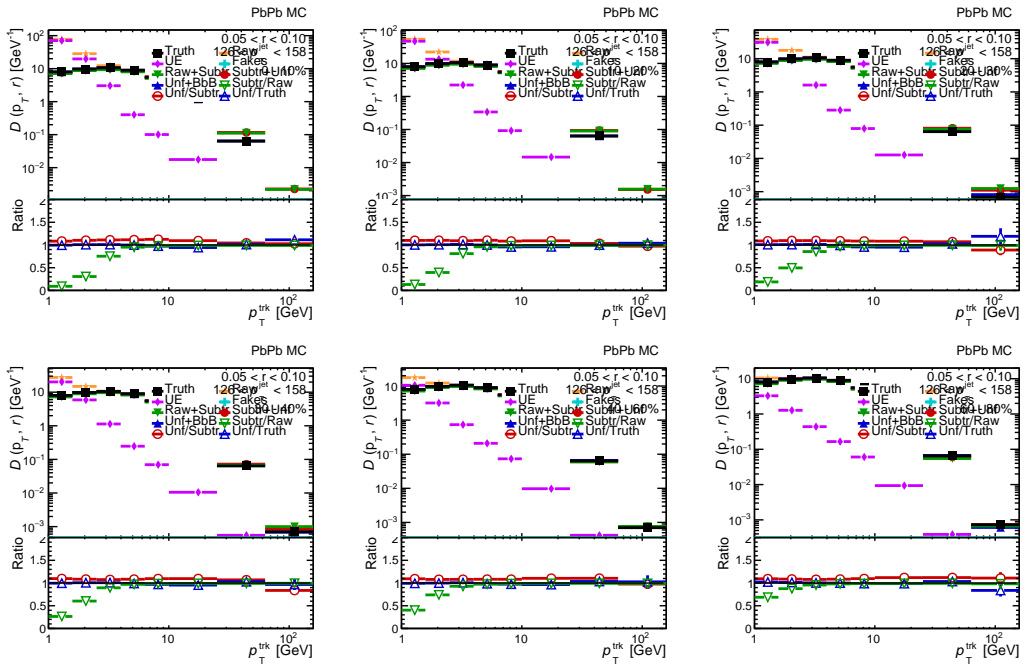


Figure 4.59: The evolution of the $D(p_T, r)$ distributions for Pb+Pb MC as various corrections are applied. The spectra is shown for tracks with $0.05 < \Delta r < 0.10$ away from the jet axis, for $126 < p_T^{\text{jet}} < 158$ GeV. The ratios showing the effect of the subtraction, unfolding and bin by bin correction (left and right), as well as the MC closure (left) are shown in the lower half of the panels. The different panels are different centrality selections.

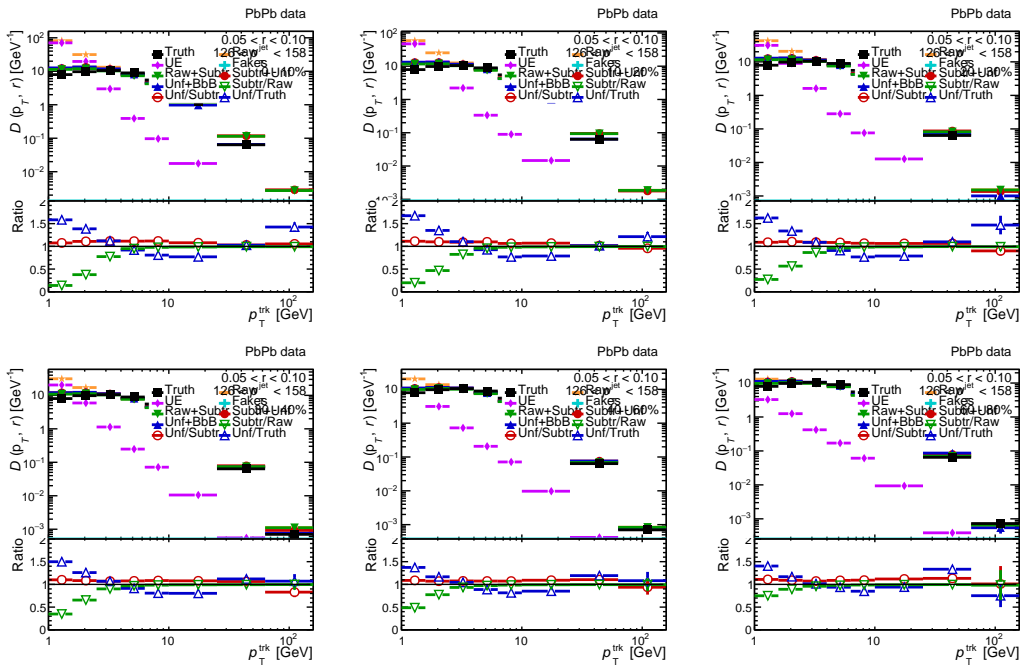


Figure 4.60: The evolution of the $D(p_T, r)$ distributions for Pb+Pb data (bottom six panels) as various corrections are applied. The spectra is shown for tracks with $0.05 < \Delta r < 0.10$ away from the jet axis, for $126 < p_T^{\text{jet}} < 158$ GeV. The ratios showing the effect of the subtraction, unfolding and bin by bin correction (left and right), as well as the MC closure (left) are shown in the lower half of the panels. The different panels are different centrality selections.

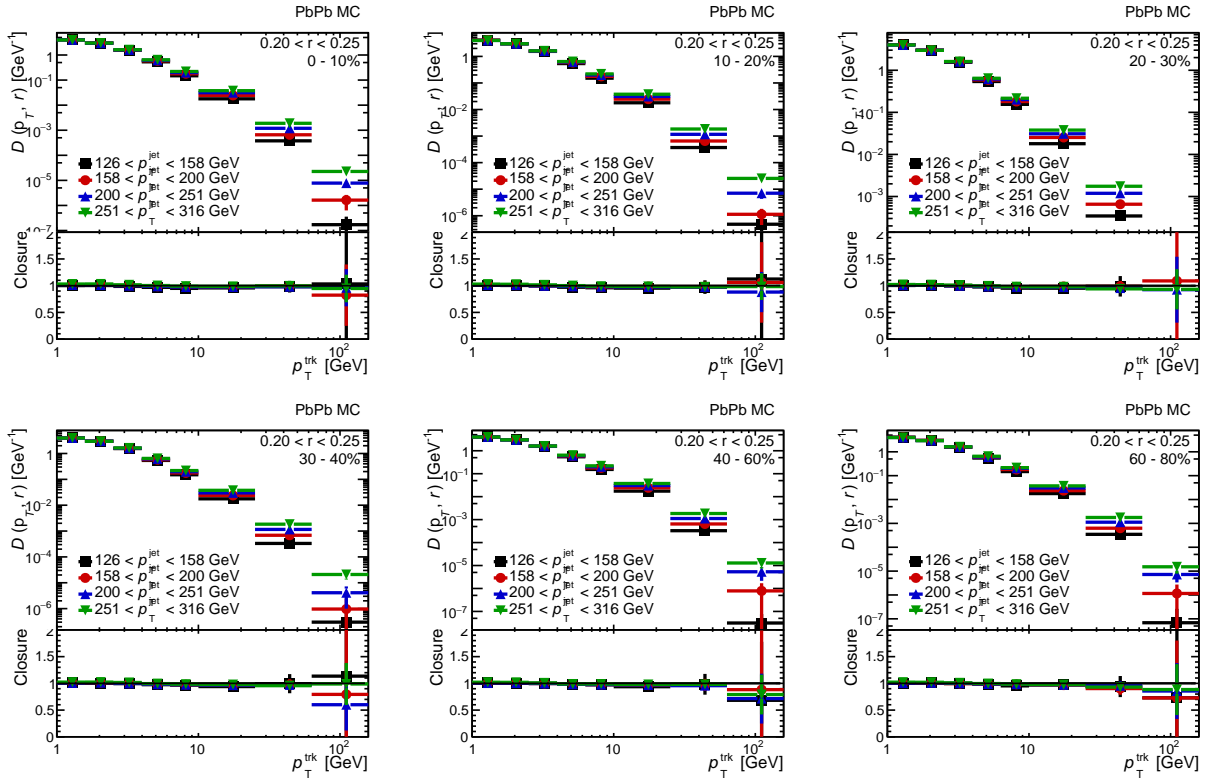


Figure 4.61: The charged particle spectra and MC closure as a function of p_T^{ch} for different p_T^{jet} bins, reconstructed track - reconstructed jet pairs, that have $0.20 < r < 0.25$, in data overlay Pb+Pb MC samples. Each panel is a different centrality bin. The closure is seen to be well within 1%.

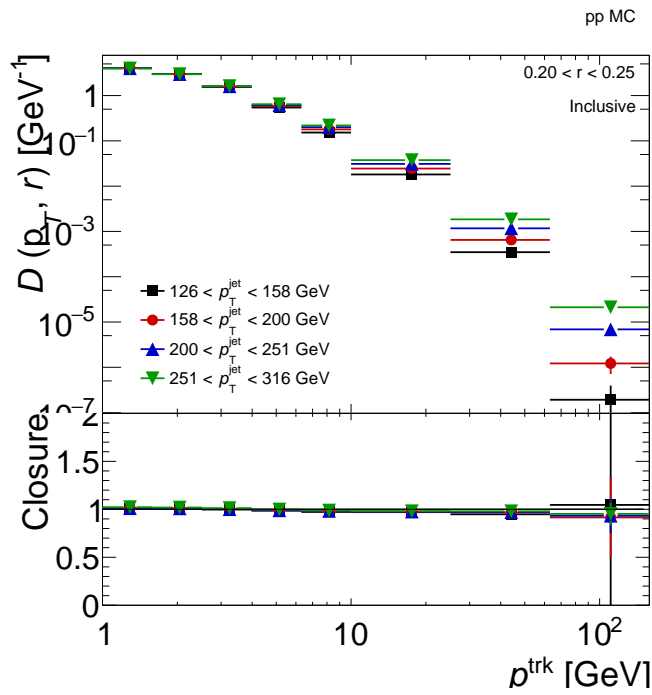


Figure 4.62: The charged particle spectra and MC closure as a function of p_T^{ch} for different p_T^{jet} bins, reconstructed track - reconstructed jet pairs, that have $0.20 < r < 0.25$, in pp MC samples. The closure is seen to be well within 1%

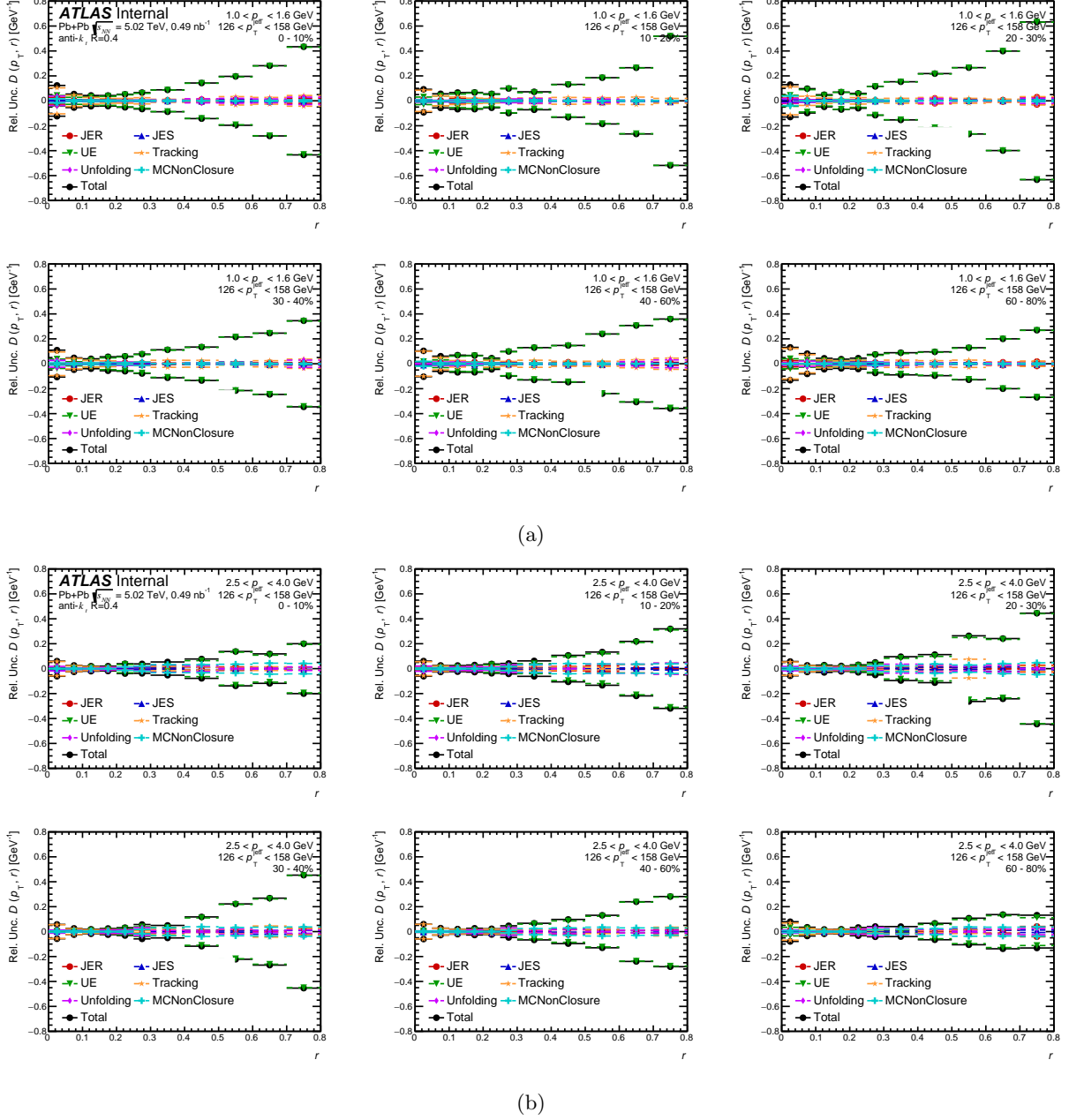


Figure 4.63: A summary of the systematic uncertainties on $R_{D(p_T, r)}$ distributions for different track $1.0 < p_T < 1.6 \text{ GeV}$ (4.63(a)) and $2.5 < p_T < 4.0 \text{ GeV}$ (4.63(b)), for jets with p_T $126\text{--}158 \text{ GeV}$, as a function of r for different centrality bins. Different panels are different centrality bins. The uncertainties from the JES, JER, UE, and Tracking are shown, along with the total systematic uncertainty from all sources.

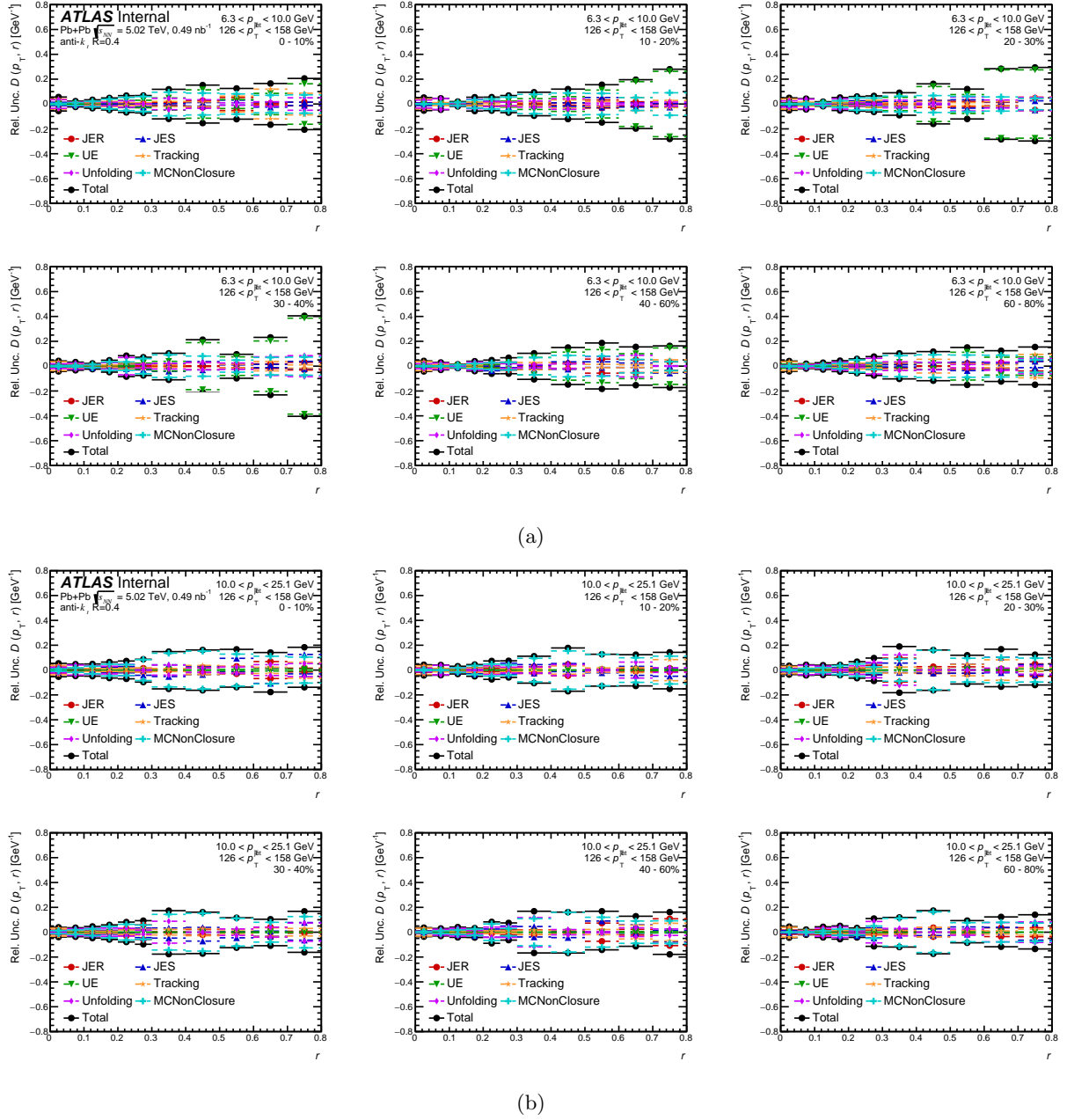


Figure 4.64: A summary of the systematic uncertainties on $R_{D(p_T, r)}$ distributions for different track $6.3 < p_T < 10.0 \text{ GeV}$ (4.64(a)) and $10.0 < p_T < 25.1 \text{ GeV}$ (4.64(b)), for jets with $p_T 126\text{--}158 \text{ GeV}$, as a function of r for different centrality bins. The uncertainties from the JES, JER, UE, and Tracking are shown, along with the total systematic uncertainty from all sources.

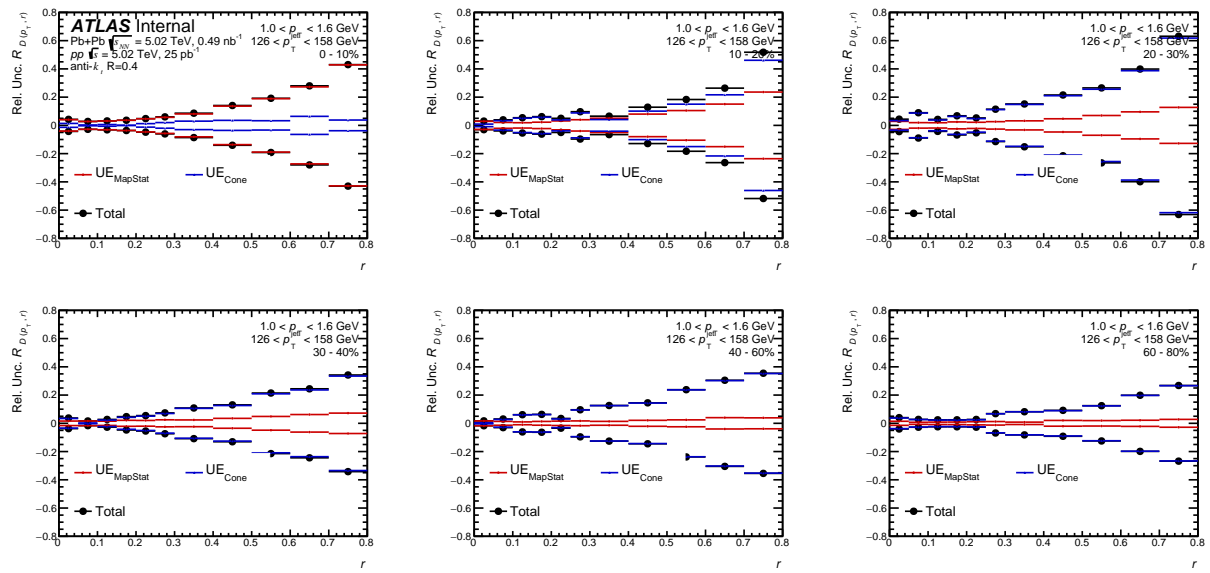


Figure 4.65: Size of the individual contributions to the underlying event systematic uncertainty as a function for r for 0-10% Pb+Pb collisions, in 126-158 GeV jets, 1-1.6 GeV tracks.

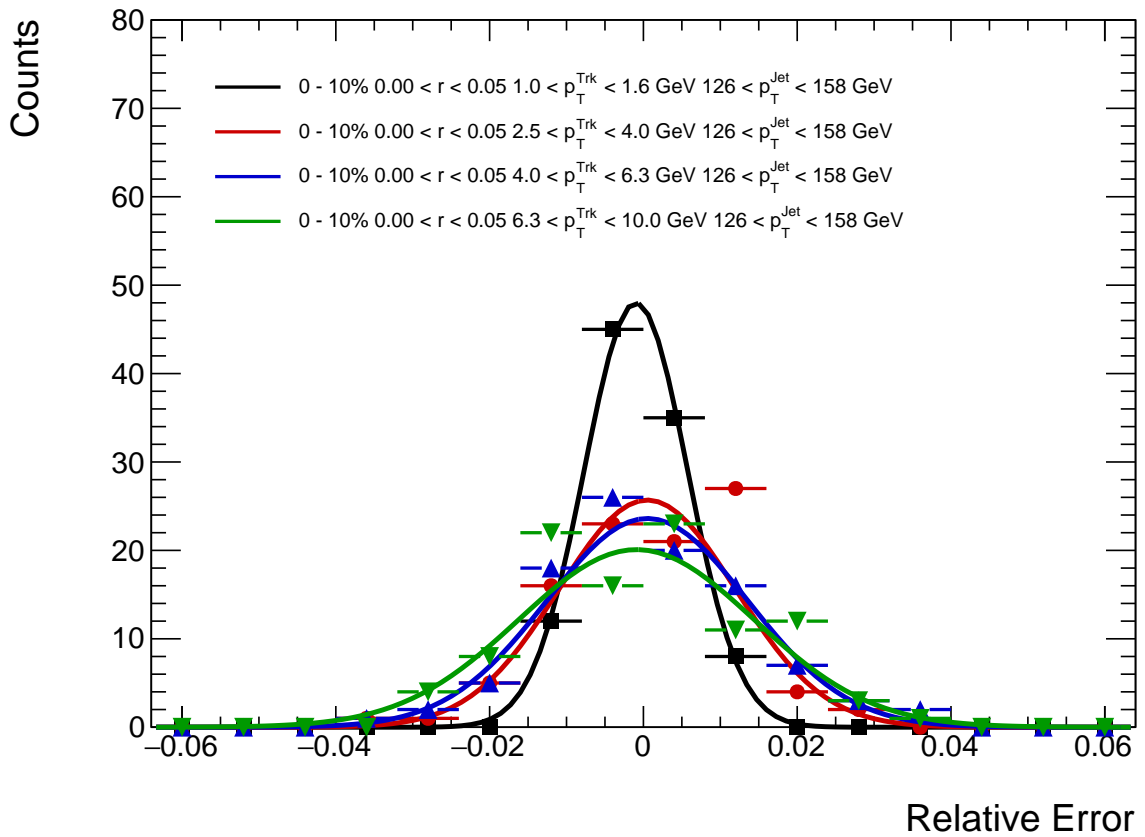


Figure 4.66: Examples of the relative differences between the nominal and shifted values of the underlying event, fit to a gaussian distribution. The width on the gaussian is taken as the systematic uncertainty on the underlying. Wider distributions indicate a larger statistical uncertainty on the bin content in the $\eta - \phi$ map used to estimate the UE.

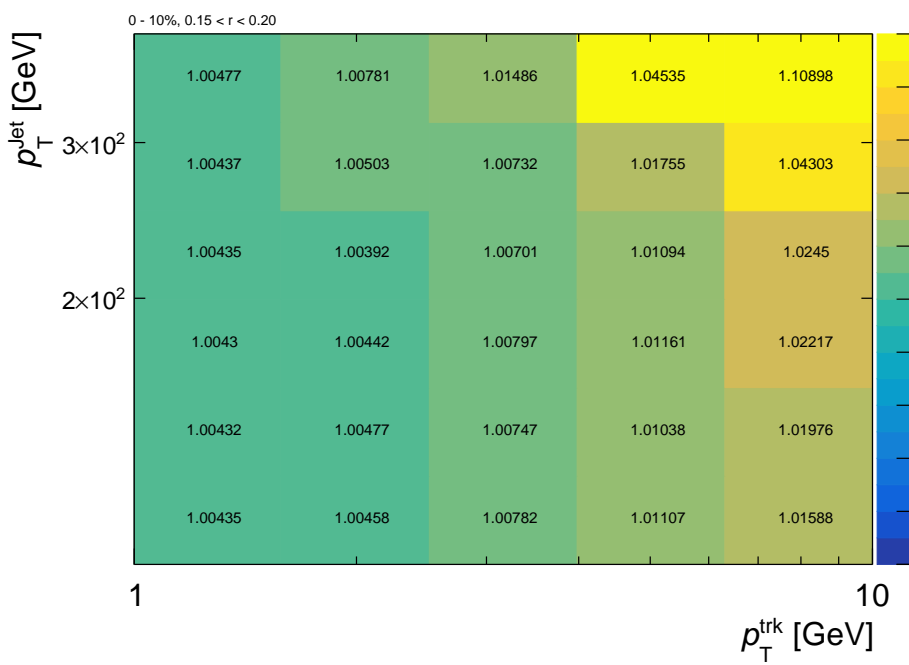


Figure 4.67: Size of the systematic uncertainty from the map statistic component, as a function for p_T^{ch} and p_T^{jet} for 0-10% Pb+Pb collisions, $0.15 < r < 0.20$ away from the jet axis.

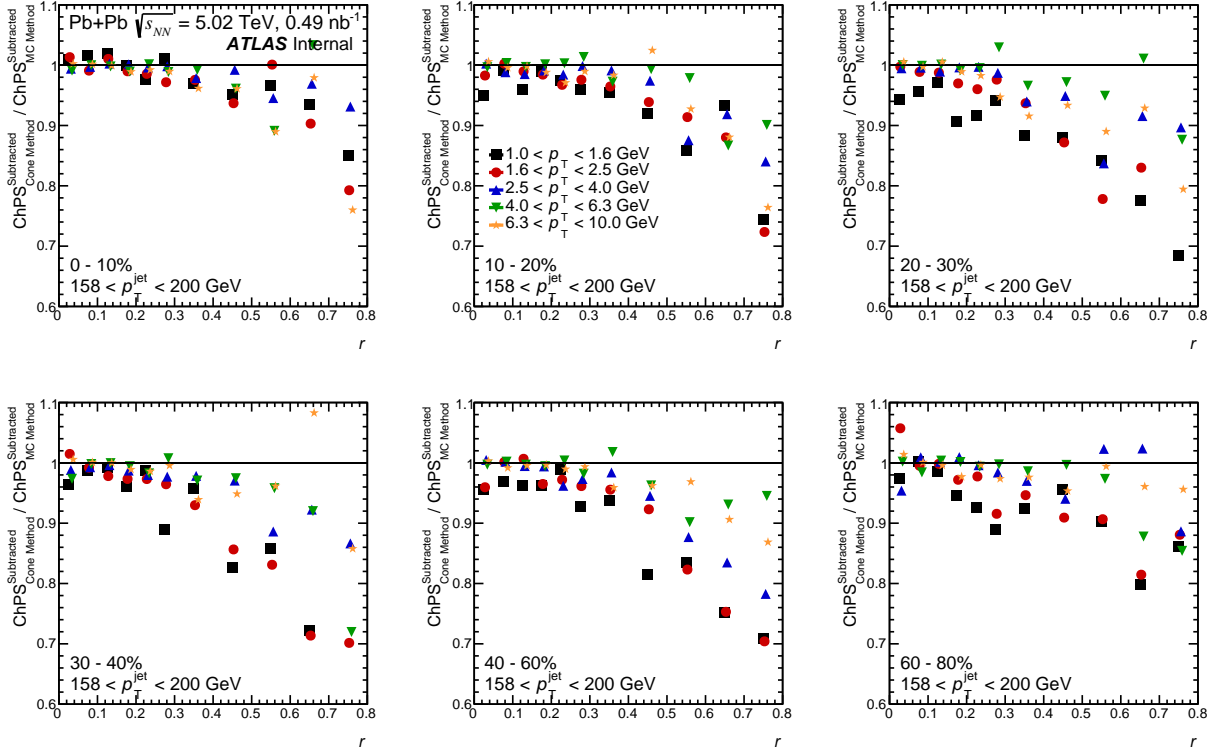


Figure 4.68: Ratio of the charged particle spectra as determined using two different UE estimation methods as a function for r for 0-10% Pb+Pb collisions in 126-158 GeV jets and 1-1.6 GeV tracks. Deviations from unity are a combination of the difference between the two methods and the signal to background ratio. The largest differences between the spectra are seen at large r , where the signal to background is the smallest. Points are offset along the x-axis for ease of viewing.

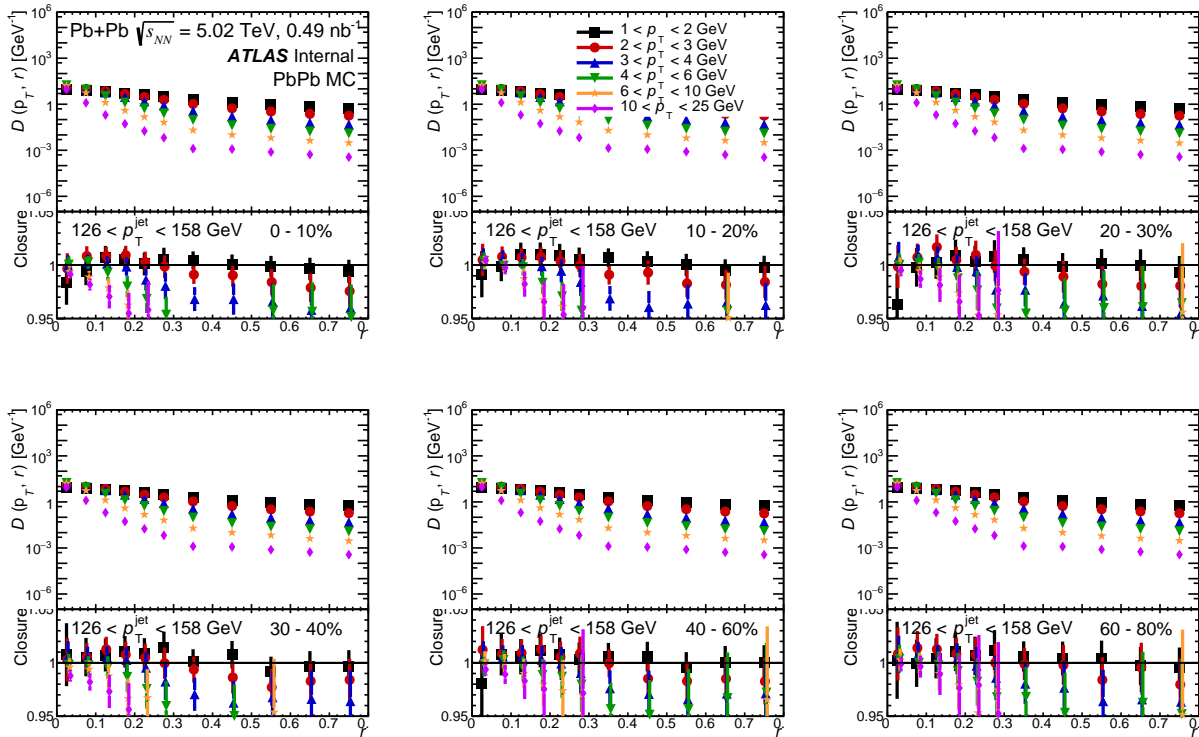


Figure 4.69: Size of the non-closure as a function for r for 0-10% Pb+Pb collisions, in 126-158 GeV jets for different p_T^{ch} ranges. Points in the bottom panel are offset along the x-axis for ease of viewing.

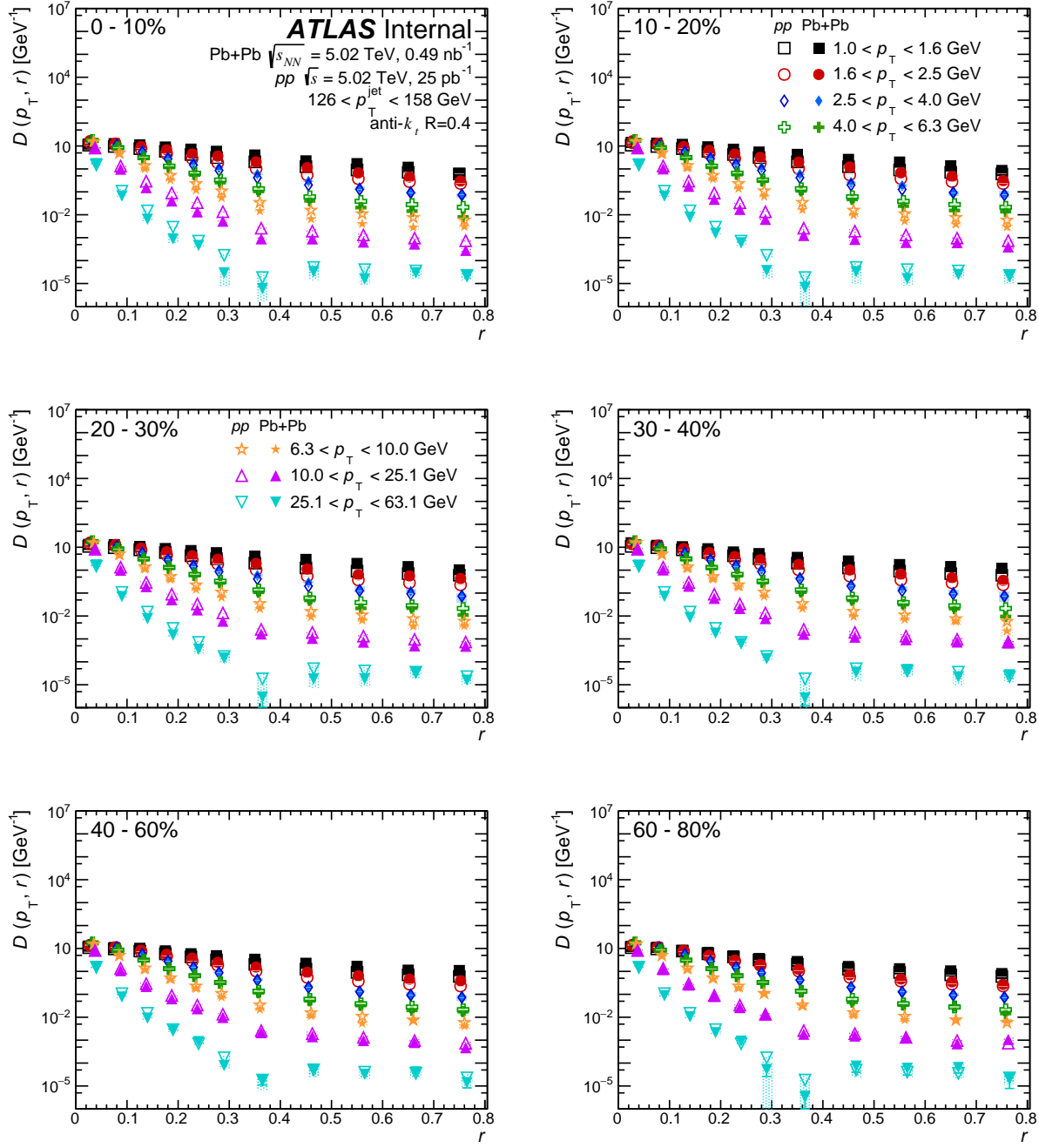


Figure 4.70: The $D(p_T, r)$ distributions in pp (open symbols) and $Pb+Pb$ (closed symbols) as a function of angular distance r for p_{jet}^T of 126 to 158 GeV. The colors represent different track p_T ranges, and each panel is a different centrality selection. The vertical bars on the data points indicate statistical uncertainties while the shaded boxes indicate systematic uncertainties. The widths of the boxes are not indicative of the bin size and the points are shifted horizontally for better visibility.

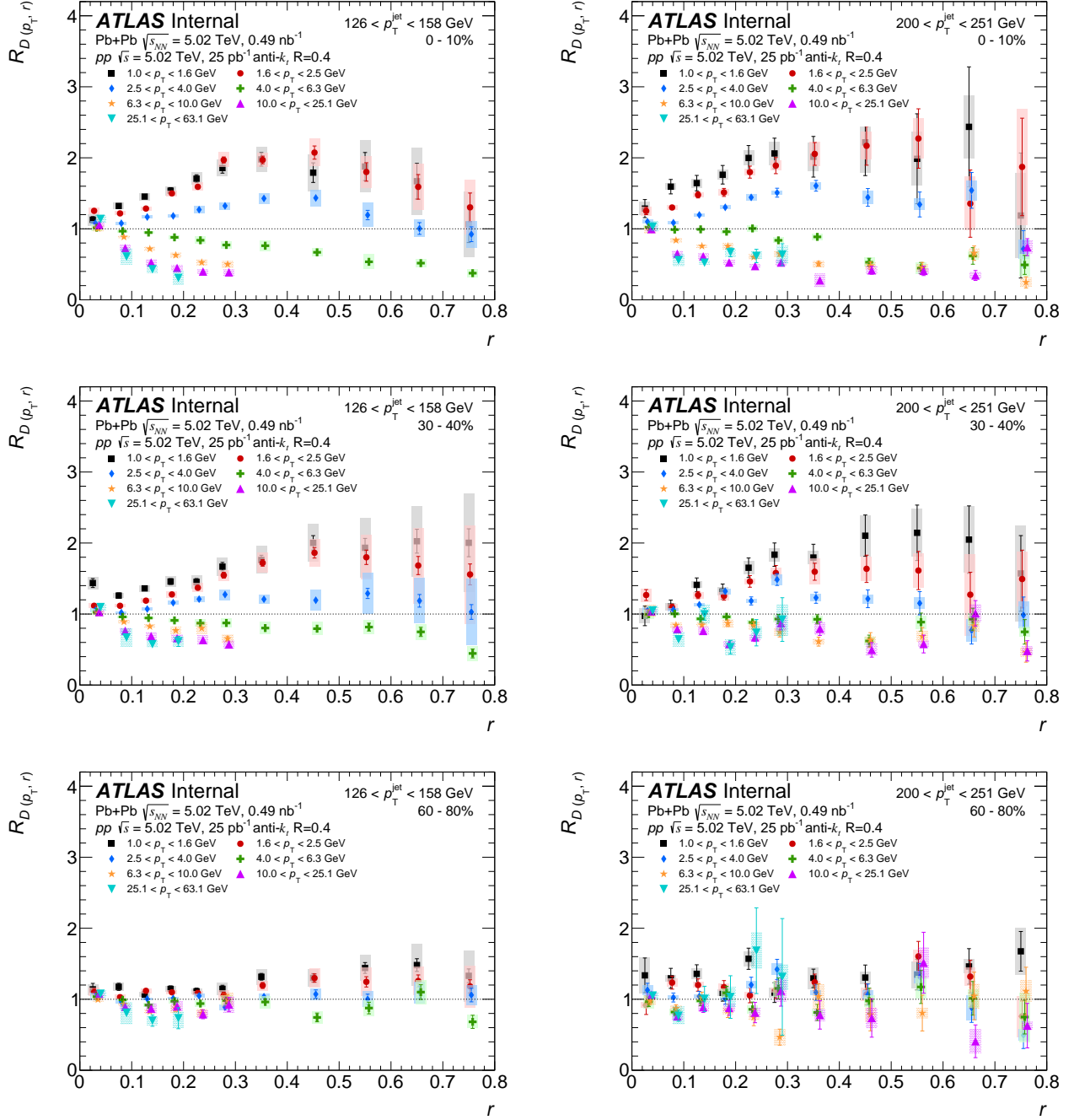


Figure 4.71: Ratios of $D(p_T, r)$ distributions in 0–10% (top), 30–40% (middle), and 60–80% (bottom) Pb+Pb collisions to pp collisions as a function of angular distance r for p_T^{jet} of 126 to 158 GeV (left) and of 200 to 251 GeV (right) for six p_T selections. The vertical bars on the data points indicate statistical uncertainties while the shaded boxes indicate systematic uncertainties. The widths of the boxes are not indicative of the bin size and the points are shifted horizontally for better visibility.

4.8 Discussion

This section further discusses results from the previous section.

4.8.1 $R_{D(p_T,r)}$ distributions

Here the centrality, p_T^{jet} and the charged-particle p_T dependence of the $R_{D(p_T,r)}$ distributions introduced in Section 4.7 are discussed.

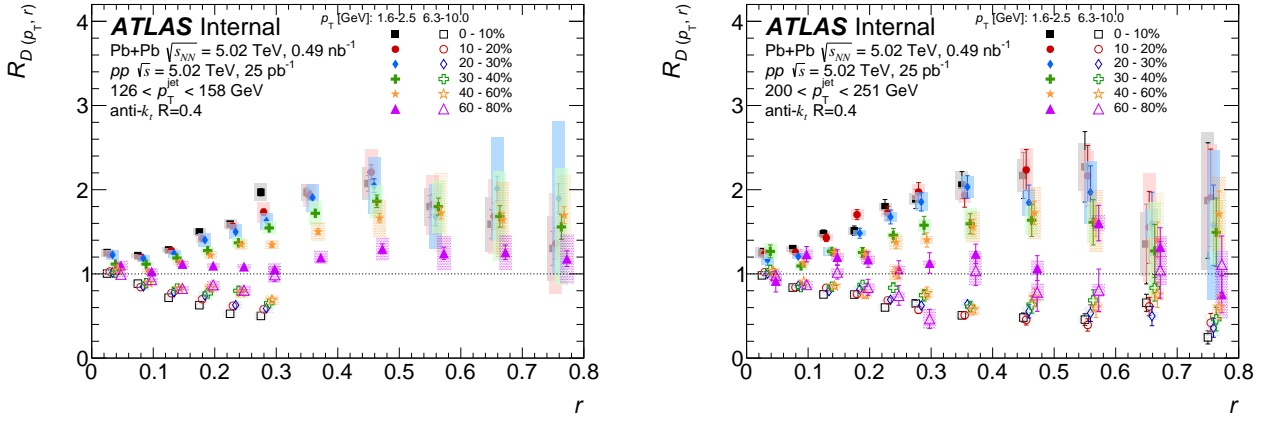


Figure 4.72: The $R_{D(p_T,r)}$ distributions for p_T^{jet} of 126–158 GeV and 200–251 GeV as a function of angular distance r for two p_T selections, 1.6–2.5 GeV (closed symbols) and 6.3–10.0 GeV (open symbols), and six centrality intervals. The vertical bars on the data points indicate statistical uncertainties while the shaded boxes indicate systematic uncertainties. The widths of the boxes are not indicative of the bin size and the points are shifted horizontally for better visibility.

The centrality dependence of $R_{D(p_T,r)}$ for two charged-particle p_T intervals: 1.6–2.5 GeV and 6.3–10.0 GeV, and two different p_T^{jet} ranges: 126–158 GeV and 200–251 GeV, is presented in Figure 4.72. For both p_T^{jet} selections and 1.6–2.5 GeV charged particles, the magnitude of the excess increases with increasing collision centrality and r for $r < 0.3$. The magnitude of the excess is approximately a factor of two in the most central collisions for $r > 0.3$. A continuous centrality dependent suppression of yields of charged-particles with $6.3 < p_T < 10.0$ GeV is observed. The magnitude of the modifications decreases with decreasing collision centrality for both p_T intervals and p_T^{jet} selections.

The p_T^{jet} dependence of the $R_{D(p_T,r)}$ values is directly explored by overlaying p_T^{jet} selections in Figure 4.73. These distributions are for the 0–10% most central collisions, for the same two charged-particle p_T selections shown in Figure 4.72. A trend of increasing $R_{D(p_T,r)}$ with increasing p_T^{jet} is observed for $r < 0.25$ for low p_T charged particles; at larger r values there is no significant dependence of $R_{D(p_T,r)}$ on p_T^{jet} . Furthermore, for the higher- p_T charged particles, no significant dependence on p_T^{jet} is observed.

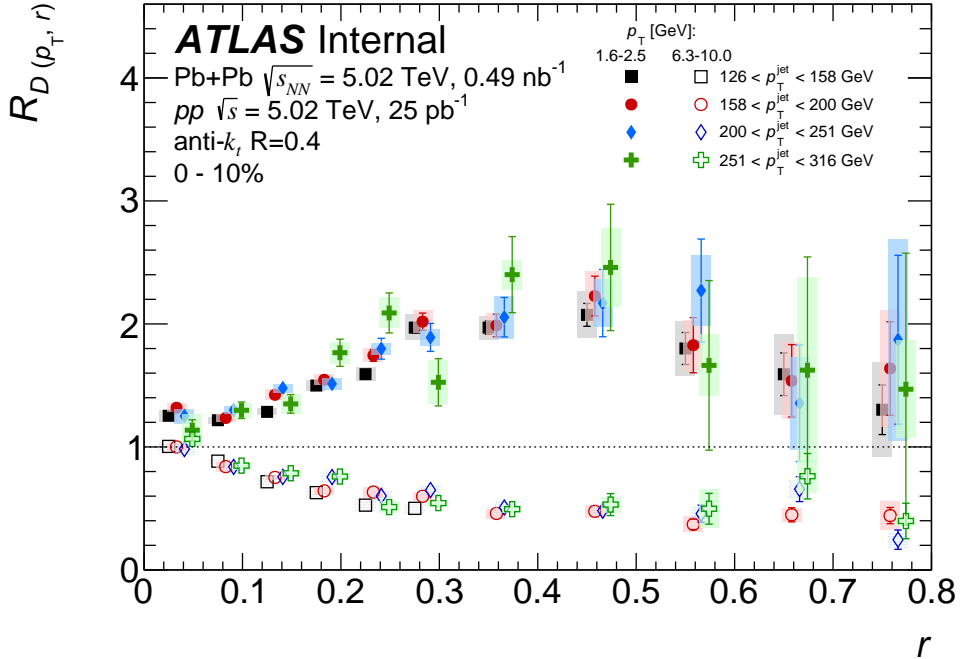


Figure 4.73: $R_{D(p_T, r)}$ as a function of r for 0–10% collisions for charged particles with $1.0 < p_T < 1.6 \text{ GeV}$ (closed symbols) and $6.3 < p_T < 10.0 \text{ GeV}$ (open symbols) for different p_T^{jet} selections. The vertical bars on the data points indicate statistical uncertainties while the shaded boxes indicate systematic uncertainties. The widths of the boxes are not indicative of the bin size and the points are shifted horizontally for better visibility.

In Figure 4.71, it was shown that for central and mid-central collisions, there is an enhancement of charged particles with $p_T < 4.0 \text{ GeV}$ and a suppression of charged particles with $p_T > 4.0 \text{ GeV}$. In Figure 4.74 the p_T dependence for selections in r is directly investigated for 0–10%, 30–40% and 60–80% central collisions for 126–158 and 200–251 GeV jets. Interestingly, at all measured p_T , there is no significant suppression of the yields in Pb+Pb collisions for $r < 0.05$. For larger r values the yields are enhanced for charged-particles with $p_T < 4 \text{ GeV}$ and suppressed for higher p_T charged-particles in both the 0–10% and 30–40% centrality selections and both p_T^{jet} ranges presented here. The magnitude of the enhancement increases for decreasing p_T at low p_T and increases with increasing p_T at high p_T , until about 10 GeV, after which the suppression remains approximately constant. At fixed p_T the magnitude of the deviation from unity is largest for $0.3 < r < 0.4$ and $0.5 < r < 0.6$. In the 60–80% central collisions, the same trend remains true (but with smaller magnitude modifications) for $126 < p_T^{\text{jet}} < 158 \text{ GeV}$; for the higher p_T^{jet} selection the larger uncertainties do not allow a clear conclusion to be drawn for peripheral collisions.

One possible explanation of the modification of the jet fragmentation in this kinematic range [13] is the larger expected energy loss of gluon-initiated jets leading to a relative enhancement of quark jets in Pb+Pb

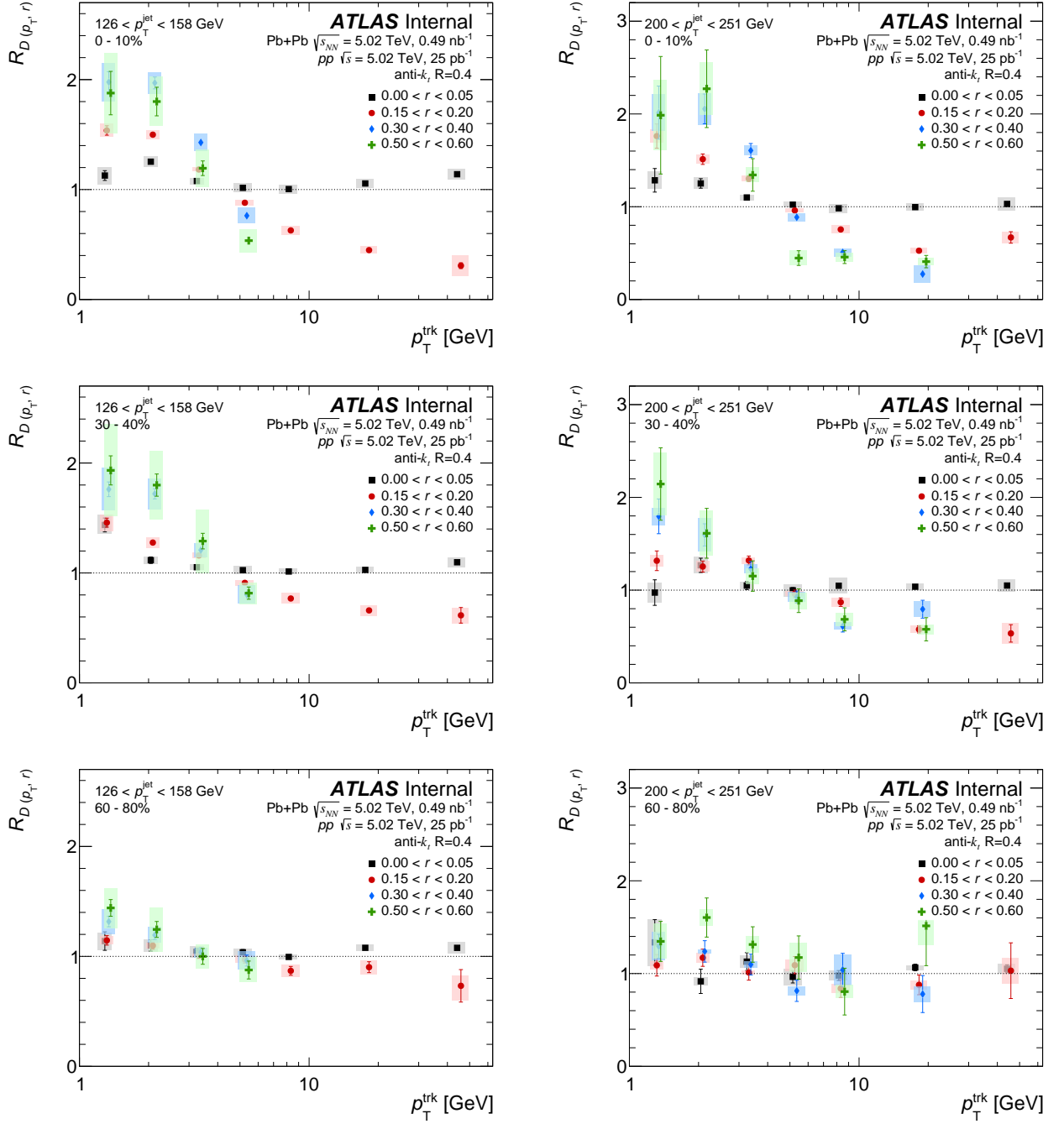


Figure 4.74: $R_{D(p_T, r)}$ as a function of p_T in 0–10% (top), 30–40% (middle), and 60–80% (bottom) Pb+Pb collisions to pp collisions for two different p_T^{jet} selections: 126–158 GeV (left) and 200–251 GeV (right). The different colors indicate different angular distances from the jet axis. The vertical bars on the data points indicate statistical uncertainties while the shaded boxes indicate systematic uncertainties. The widths of the boxes are not indicative of the bin size and the points are shifted horizontally for better visibility.

collisions compared to pp collisions at a given p_T^{jet} value [52]. Since gluon jets have a broader distribution of particle transverse momentum with respect to the jet direction compared to quark-initiated jets [53], such an effect could potentially describe the narrowing of particle distribution around the jet direction for particles with $p_T > 4.0$ GeV observed here, though no calculations of this are available.

4.8.2 Differences of $D(p_T, r)$ distributions

In addition to the ratios of the $D(p_T, r)$ distributions, differences between the charged particle yields are also evaluated to quantify the modification in terms of the particle density. These are given as:

$$\Delta D(p_T, r) = D(p_T, r)_{\text{Pb+Pb}} - D(p_T, r)_{pp} \quad (4.16)$$

These differences are presented as a function of r for different p_T selections in 0–10% central collisions in Figure 4.75. These distributions show an excess in the charged-particle yield density for Pb+Pb collisions compared to pp collisions for charged particles with $p_T < 4.0$ GeV. This excess ranges from 0.5 to 4 particles per unit area at 1 GeV in 126–158 GeV jets for 0–10% central Pb+Pb collisions and increases with increasing p_T^{jet} . The largest excesses for charged particles with $p_T < 4.0$ GeV is within the jet cone. For large r values, the density decreases, but remains positive. A depletion for higher p_T particles of approximately 0.5 particles per unit area is seen for 126–158 GeV jets in 0–10% central Pb+Pb collisions. The magnitude of this depletion increases for higher p_T^{jet} . There is a minimum in the $\Delta D(p_T, r)$ distributions of charged particles with $4.0 < p_T < 25.1$ GeV at $0.05 < r < 0.10$ that is seen at many p_T^{jet} ranges under investigation. The magnitudes of the excesses and deficits discussed here are dependent on the sizes of the charged-particle p_T selections chosen. In order to remove that dependence, Section 4.8.3 provides similar quantities in which a wider charged-particle p_T range is integrated over.

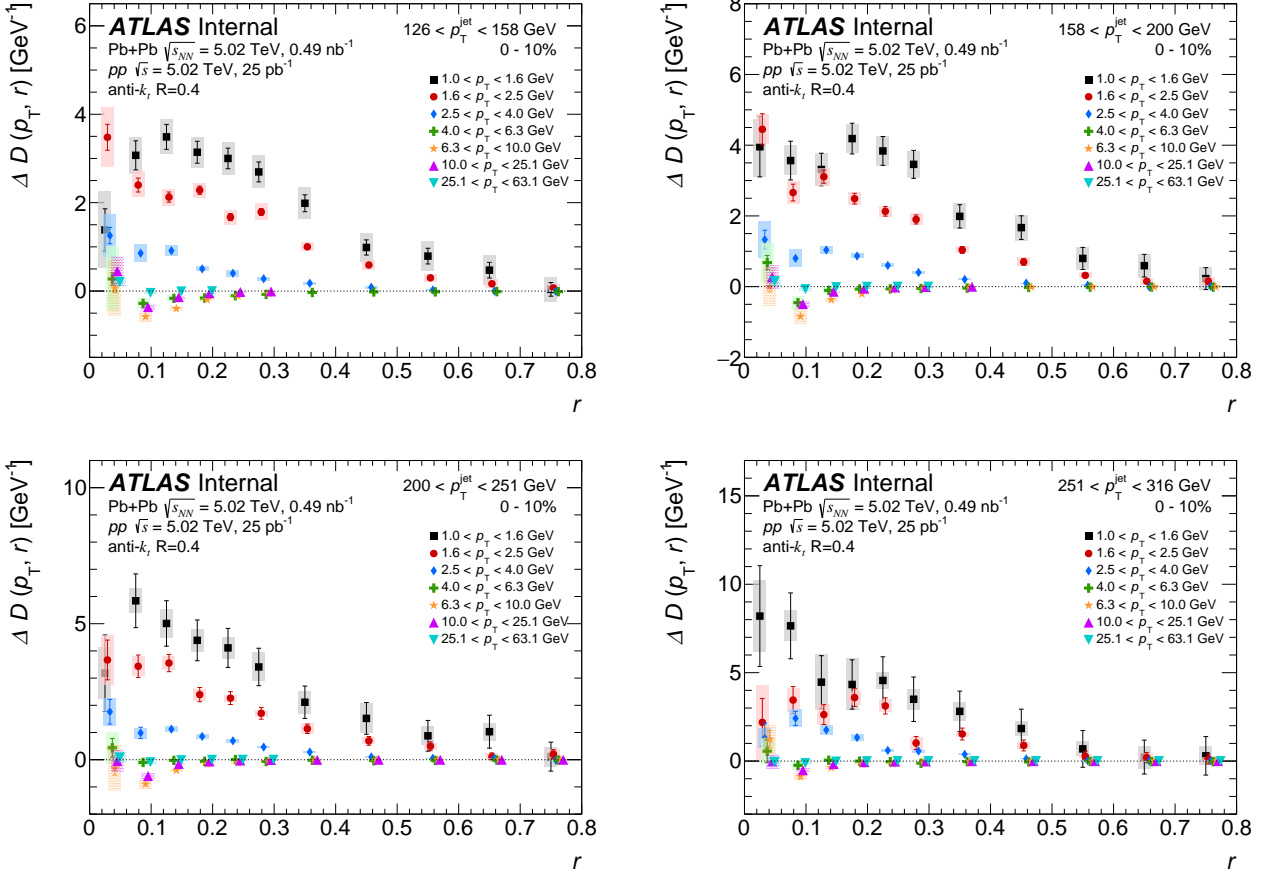


Figure 4.75: $\Delta D(p_T, r)$ as a function of r in central collisions for all p_T ranges in four p_T^{jet} selections: 126 – 158 GeV, 158 – 200 GeV, 200 – 251 GeV, and 251 – 316 GeV. The vertical bars on the data points indicate statistical uncertainties while the shaded boxes indicate systematic uncertainties. The widths of the boxes are not indicative of the bin size and the points are shifted horizontally for better visibility.

4.8.3 p_T integrated distributions

Motivated by similar studies of the enhancement of soft fragments in jet fragmentation functions in Pb+Pb compared to pp collisions from [13], the $D(p_T, r)$ distributions can be integrated for charged particles with $p_T \geq 4$ GeV to construct the quantities $\Theta(r)$ and $P(r)$ defined as:

$$\Theta(r) = \int_1^4 D(p_T, r) dp_T \quad (4.17)$$

$$P(r) = \int_0^r \int_1^4 D(p_T, r) dp_T dr' \quad (4.18)$$

The $\Theta(r)$ values are integrated between 1.0–4.0 GeV charged particles to provide a summary look at the p_T region of enhancement discussed above. The $P(r)$ values further add a running integral over r and provide information about the jet shape. Both of these quantities can be compared between the pp and Pb+Pb systems to give the following distributions:

$$\Delta_{\Theta(r)} = \Theta(r)_{\text{Pb+Pb}} - \Theta(r)_{pp} \quad (4.19)$$

$$R_{\Theta(r)} = \frac{\Theta(r)_{\text{Pb+Pb}}}{\Theta(r)_{pp}} \quad (4.20)$$

$$R_{P(r)} = \frac{P(r)_{\text{Pb+Pb}}}{P(r)_{pp}} \quad (4.21)$$

(the quantity $\Delta_{P(r)}$ can also be analogously defined, but is omitted from the present discussion). These aggregate quantities are intended to provide some summary information about the location with respect to the jet axis, magnitude, and p_T^{jet} dependence of the low- p_T charged-particle excess discussed above. The ratio quantities are useful for comparisons to other Pb+Pb measurements; $\Delta_{\Theta(r)}$ is very similar to $\Delta D(p_T, r)$, however it is integrated over charged-particle p_T from 1.0–4.0 GeV.

Figure 4.76 shows the $\Delta_{\Theta(r)}$ distributions as a function of r for 0–10%, 30–40%, and 60–80% central collisions. In the most central collisions, a significant p_T^{jet} dependence to $\Delta_{\Theta(r)}$ is observed; for $r < 0.4$ (particles within the jet cone) $\Delta_{\Theta(r)}$ increases with increasing p_T^{jet} . The value of $\Delta_{\Theta(r)}$ decreases in more peripheral collisions and the p_T^{jet} dependence is no longer significant.

Figure 4.77 shows $R_{\Theta(r)}$ and $R_{P(r)}$ for 0–10%, 30–40% and 60–80% central collisions. The $R_{\Theta(r)}$ distributions of the most central collisions show a maximum for $r \sim 0.4$ and decrease for larger r . However, since $R_{\Theta(r)}$ remains at or above unity for the full range of r values presented $R_{P(r)}$ continues to slowly

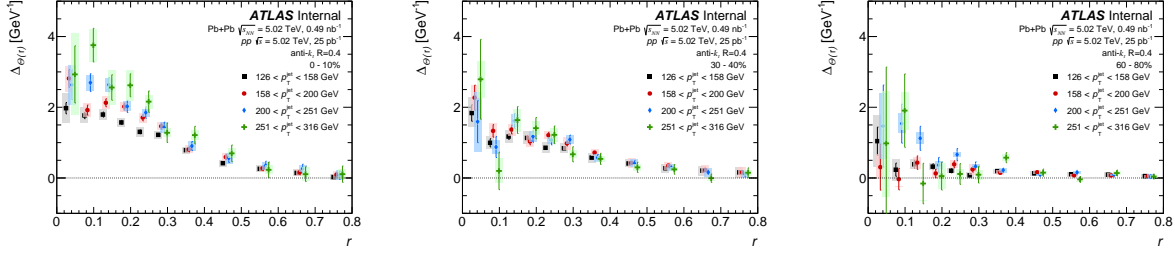


Figure 4.76: $\Delta_{\Theta(r)}$ as a function of r for charged-particles with $p_T > 4$ GeV ranges in four p_T^{jet} selections: 126–158 GeV, 158–200 GeV, 200–251 GeV, and 251–316 GeV and three centrality selections: 0–10% (left), 30–40% (middle) and 60–80% (right). The vertical bars on the data points indicate statistical uncertainties while the shaded boxes indicate systematic uncertainties. The widths of the boxes are not indicative of the bin size and the points are shifted horizontally for better visibility.

increase with increasing r over the full measured range. In more peripheral collisions, the magnitude of the excess is reduced and the trends in $R_{\Theta}(r)$ are less clear, however the slow increase of $R_P(r)$ is clearly seen for the 30–40% central collisions.

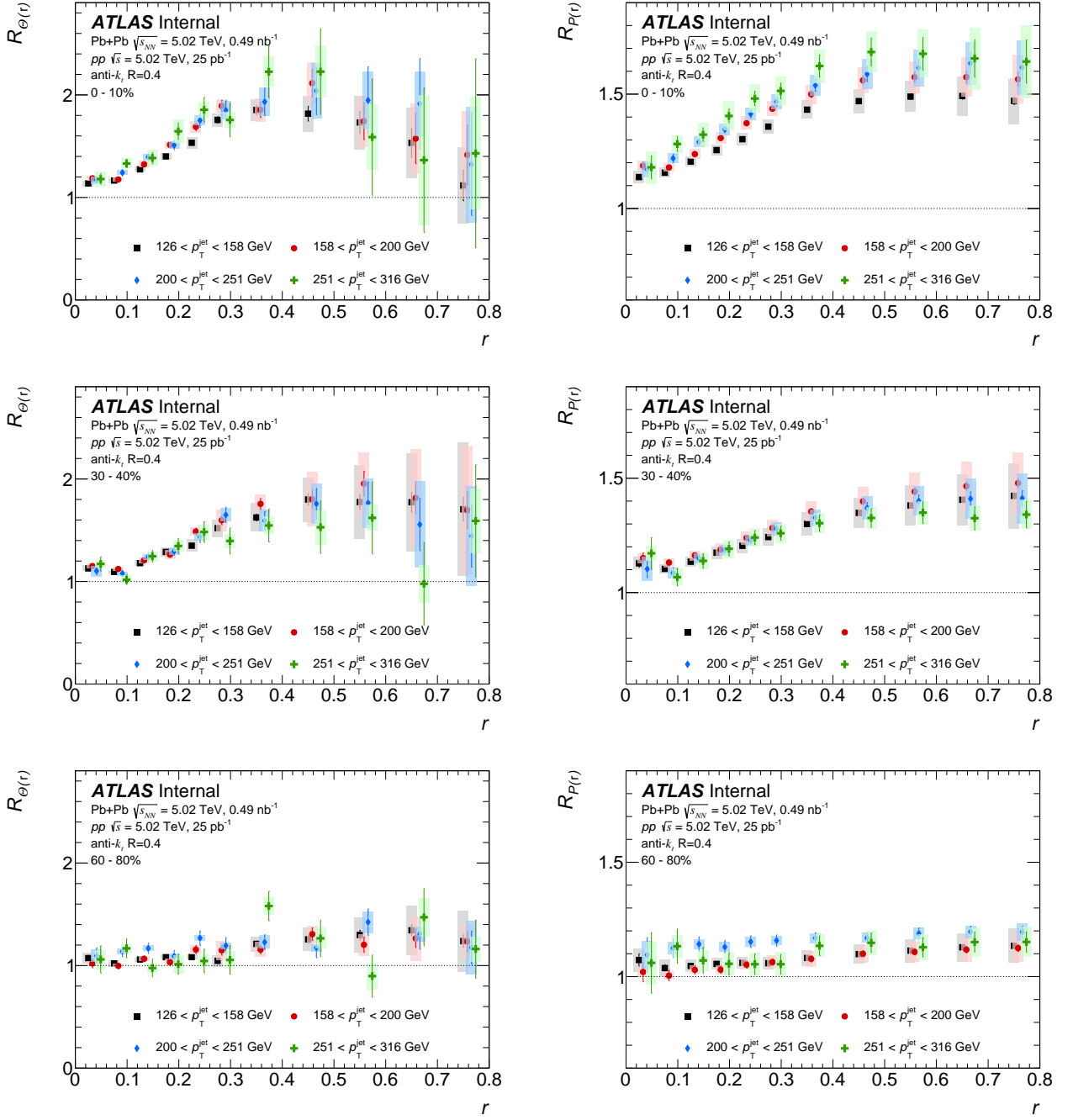


Figure 4.77: $R_{\Theta(r)}$ (left) and $R_{P(r)}$ (right) as a function of r in central collisions for charged-particles with $p_T > 4 \text{ GeV}$ ranges in four p_T^{jet} selections: 126–158 GeV, 158–200 GeV, 200–251 GeV, and 251–316 GeV and three centrality selections: 0–10% (top), 30–40% (middle) and 60–80% (bottom). The vertical bars on the data points indicate statistical uncertainties while the shaded boxes indicate systematic uncertainties. The widths of the boxes are not indicative of the bin size and the points are shifted horizontally for better visibility.

Appendix A

HI JER Uncertainty

A.0.1 Deriving the HI JER

1 Reviewing and updating Run 1 analysis

We will start with the starting point from the Run 1 note. Namely, we define the per-jet measurement errors in terms of terms that are fully correlated between EMTopo and HI collections and terms that are completely uncorrelated. For now, we assume the correlated contribution is the same for both collections.

$$\begin{aligned}\Delta p_T^{\text{EM}} &\equiv \Delta_c + \Delta_{\text{EM}} \\ \Delta p_T^{\text{HI}} &\equiv \Delta_c + \Delta_{\text{HI}}\end{aligned}\quad (1)$$

Then, the jet energy resolution, defined as the standard deviation of the jet energy from the true can be written,

$$\begin{aligned}R_{\text{EM}} &\equiv \text{Var}[\Delta p_T^{\text{EM}}] = \text{Var}[\Delta_c + \Delta_{\text{EM}}] = \text{Var}[\Delta_c] + \text{Var}[\Delta_{\text{EM}}] \\ R_{\text{HI}} &\equiv \text{Var}[\Delta p_T^{\text{HI}}] = \text{Var}[\Delta_c + \Delta_{\text{HI}}] = \text{Var}[\Delta_c] + \text{Var}[\Delta_{\text{HI}}].\end{aligned}\quad (2)$$

Following the convention of the note, we will simplify the notation: $\text{Var}[\Delta_c] \equiv s_c^2$, $\text{Var}[\Delta_{\text{EM}}] \equiv s_{\text{EM}}^2$, $\text{Var}[\Delta_{\text{HI}}] \equiv s_{\text{HI}}^2$ with the results that

$$\begin{aligned}R_{\text{EM}} &\equiv s_c^2 + s_{\text{EM}}^2 \\ R_{\text{HI}} &\equiv s_c^2 + s_{\text{HI}}^2\end{aligned}\quad (3)$$

We can use the MC to evaluate R_{EM} and R_{HI} and we can evaluate the difference between the result which we define as A :

$$A \equiv R_{\text{EM}} - R_{\text{HI}} = s_c^2 + s_{\text{EM}}^2 - s_c^2 - s_{\text{HI}}^2 = s_{\text{EM}}^2 - s_{\text{HI}}^2.\quad (4)$$

We can also evaluate a quantity that is differently sensitive to the relative resolution of the two jet collections. Namely we can evaluate the variance of the difference between Δp_T^{EM} and Δp_T^{HI} :

$$B_{\text{MC}} \equiv \text{Var}[(\Delta p_T^{\text{EM}} - \Delta p_T^{\text{HI}})] = s_{\text{EM}}^2 + s_{\text{HI}}^2.\quad (5)$$

However, we can also evaluate the same quantity but using data. The difference between these two values we will take as an estimate of the (squared) uncertainty on B :

$$\delta^2 B \equiv (B_{\text{MC}} - B_{\text{data}})^2.\quad (6)$$

The Jet-EtMiss group has provided an estimate for the uncertainty on R_{EM} , which we will write $\delta^2 R_{\text{EM}}$. The question we want to answer is “given $\delta^2 R_{\text{EM}}$ and $\delta^2 B$, what limits can we put on $\delta^2 R_{\text{HI}}$?

Using Eq. 3, we can write

$$\begin{aligned}\delta^2 R_{\text{EM}} &\equiv \delta^2 s_c^2 + \delta^2 s_{\text{EM}}^2 \\ \delta^2 R_{\text{HI}} &\equiv \delta^2 s_c^2 + \delta^2 s_{\text{HI}}^2\end{aligned}\quad (7)$$

Then, given a value of $\delta^2 R_{\text{EM}}$, $\delta^2 s_c^2$ can only vary over the range $0 \leq s_c^2 \leq \delta^2 R_{\text{EM}}$. Suppose we define $\delta^2 s_c^2 \equiv f \delta^2 R_{\text{EM}}$. Then, $\delta^2 s_{\text{EM}}^2 = (1-f) \delta^2 R_{\text{EM}}$. We do not know *a priori* the value of f , but $\delta^2 B$ constrains f since $\delta^2 B = \delta^2 s_{\text{EM}}^2 + \delta^2 s_{\text{HI}}^2$. Since both terms are positive definite, $\delta^2 s_{\text{EM}}^2 \leq \delta^2 B$ or, more explicitly,

$$(1-f) \delta^2 R_{\text{EM}} \leq \delta^2 B \rightarrow f \geq 1 - \frac{\delta^2 B}{\delta^2 R_{\text{EM}}}.\quad (8)$$

Let's consider the extreme values of f : $1 - \frac{\delta^2 B}{\delta^2 R_{\text{EM}}}$ and 1. For $f = 1 - \frac{\delta^2 B}{\delta^2 R_{\text{EM}}}$, $\delta^2 s_{\text{HI}}^2 = 0$ and then $\delta^2 R_{\text{HI}} = \delta^2 s_c^2 = f \delta^2 R_{\text{EM}} = \delta^2 R_{\text{EM}} - \delta^2 B$. In contrast, for $f = 1$, $\delta^2 s_{\text{EM}}^2 = 0$ so $\delta^2 B = \delta^2 s_{\text{HI}}^2$ and $\delta^2 R_{\text{EM}} = \delta^2 s_c^2$. As result, $\delta^2 R_{\text{HI}} = \delta^2 R_{\text{EM}} + \delta^2 B$. Thus, the uncertainty on the HI jet energy resolution can span the range $[\delta^2 R_{\text{EM}} - \delta^2 B, \delta^2 R_{\text{EM}} + \delta^2 B]$ depending on the value of f . Since we don't know f , the upper value provides a conservative estimate for the uncertainty on the HI jet energy resolution.

The difference between the above result and equation 20 in the Run 1 note results from the neglect of a covariance term in Eq. 20 in the note. That term reflects the fact that the uncertainty in the EMTopo jet energy resolution can be correlated with the systematic uncertainty on A . See e.g. Eq. 4. In the above analysis, that covariance is explicitly accounted for in the decomposition in Eq. 3. To evaluate the covariance using the above formulation, we can write the *uncertainty covariance* between R_{EM} ($\delta^2 \sigma_{\text{HI}}$ in the note) and A using Eq. 4

$$\text{Cov}[R_{\text{EM}}, A] = \text{Var}[R_{\text{EM}}] - \text{Cov}(R_{\text{EM}}, R_{\text{HI}}) = \delta^2 R_{\text{EM}} - \text{Cov}(R_{\text{EM}}, R_{\text{HI}}). \quad (9)$$

Here all of the variances and covariances are related to uncertainties on the parameters not their statistical distributions. Using Eq. 4 and assuming no uncertainty covariance between s_c^2 , s_{EM}^2 , and s_{HI}^2 , then $\text{Cov}(R_{\text{EM}}, R_{\text{HI}}) = \delta^2 s_c^2$ with the result that

$$\text{Cov}[R_{\text{EM}}, A] = \delta^2 R_{\text{EM}} - \delta^2 s_c^2 = \delta^2 R_{\text{EM}} (1 - f). \quad (10)$$

Repeating the procedure of the note, we re-write Eq. 4

$$R_{\text{HI}} = R_{\text{EM}} - A. \quad (11)$$

This is equivalent to equation 19 in the Run 1 note, but without taking the square root. Then, following the usual propagation of errors including the covariance term,

$$\begin{aligned} \delta^2 R_{\text{HI}} &= \delta^2 R_{\text{EM}} + \delta^2 A - 2\text{Cov}[R_{\text{EM}}, A] \\ &= \Delta^2 R_{\text{EM}} [1 - 2(1 - f)] + \delta^2 B \\ &= \Delta^2 R_{\text{EM}} (2f - 1) + \delta^2 B. \end{aligned} \quad (12)$$

Now, if we evaluate Eq. 12 at the minimum and maximum values of f per the above analysis we obtain estimates for $\delta^2 R_{\text{HI}}$ of $\delta^2 R_{\text{EM}} - \delta^2 B$ and $\delta^2 R_{\text{EM}} + \delta^2 B$, respectively. These results are consistent with the above analysis and yield $\delta^2 R_{\text{EM}} + \delta^2 B$ as a conservative estimate for $\delta^2 R_{\text{HI}}$.

2 Impact of GSC calibration

The application of the GSC to the pp jets introduces a complication because it likely violates the assumptions in Eq. 2 that the correlated contribution to the per-jet measurement errors are the same in the EMTopo and HI jets. The GSC calibration factors may introduce a scale difference between the correlated contributions to the two jet collections. For the following we will assume

$$\begin{aligned} \Delta p_T^{\text{EM}}|_{\text{GSC}} &\equiv \Delta_c + \Delta_{\text{EM}} \\ \Delta p_T^{\text{HI}} &\equiv \lambda \Delta_c + \Delta_{\text{HI}} \end{aligned} \quad (13)$$

Following the above,

$$\begin{aligned} R_{\text{EM}} &\equiv s_c^2 + s_{\text{EM}}^2, \\ R_{\text{HI}} &\equiv \lambda^2 s_c^2 + s_{\text{HI}}^2. \end{aligned} \quad (14)$$

and

$$A = s_c^2 + s_{\text{EM}}^2 - \lambda^2 s_c^2 - s_{\text{HI}}^2 = (1 - \lambda^2) s_{\text{EM}}^2 - s_{\text{HI}}^2, \quad (15)$$

$$B = s_c^2 + s_{\text{EM}}^2 + \lambda^2 s_c^2 + s_{\text{HI}}^2 - 2\lambda s_c^2 = (1 - \lambda)^2 s_c^2 + s_{\text{EM}}^2 + s_{\text{HI}}^2. \quad (16)$$

For the moment, we will assume that λ can be independently estimated without any uncertainty. We will come back below and discuss how to estimate λ and evaluate the effects of non-zero uncertainty on its value.

From Eq. 16, we can write the uncertainty on B ,

$$\delta^2 B = (1 - \lambda)^4 \delta^2 s_c^2 + \delta^2 s_{\text{EM}}^2 + \delta^2 s_{\text{HI}}^2. \quad (17)$$

Now, we follow the above approach and define $\delta^2 s_c^2 \equiv \delta^2 R_{\text{EM}}$ and $\delta^2 s_{\text{EM}}^2 = (1 - f) \delta^2 R_{\text{EM}}$. Then

$$\delta^2 B = \delta^2 R_{\text{EM}} (1 + f [(1 - \lambda)^4 - 1]) + \delta^2 s_{\text{HI}}^2. \quad (18)$$

Similar to the situation above, f is bounded by the requirement that $\delta^2 s_{\text{HI}}^2 \geq 0$, so

$$1 + f [(1 - \lambda)^4 - 1] \leq \frac{\delta^2 B}{\delta^2 R_{\text{EM}}} \rightarrow f \geq \left[\frac{1}{1 - (1 - \lambda)^4} \right] \left(1 - \frac{\delta^2 B}{\delta^2 R_{\text{EM}}} \right). \quad (19)$$

Depending on the value of λ , this “minimum” value of f may be larger than unity which means that there is an inconsistency in the formulation of the result. In other words, the uncertainty on B limits the possible values of λ . More specifically,

$$\frac{1}{1 - (1 - \lambda)^4} \leq 1 - \frac{\delta^2 B}{\delta^2 R_{\text{EM}}} \quad (20)$$

or

$$(1 - \lambda)^4 \leq \frac{\frac{\delta^2 B}{\delta^2 R_{\text{EM}}}}{1 - \frac{\delta^2 B}{\delta^2 R_{\text{EM}}}}. \quad (21)$$

Assuming that this limited is satisfied, at the lower limit of f , $\delta^2 s_{\text{HI}}^2 = 0$ and $\delta^2 R_{\text{HI}} = \lambda^4 \delta^2 s_c^2$ or

$$\delta^2 R_{\text{HI}}|_{f \min} = \left[\frac{\lambda^4}{1 - (1 - \lambda)^4} \right] (\delta^2 R_{\text{EM}} - \delta^2 B). \quad (22)$$

At the upper limit, $\delta^2 s_{\text{EM}}^2 = 0$ and $\delta^2 B = \delta^2 s_{\text{HI}}^2$. Then, $\delta^2 R_{\text{HI}} = \lambda^4 \delta^2 s_c^2 + \delta^2 B$ or

$$\delta^2 R_{\text{HI}}|_{f \max} = \lambda^4 \delta^2 R_{\text{EM}} + \delta^2 B. \quad (23)$$

This value should represent the maximum uncertainty on $\delta^2 R_{\text{HI}}$. Even though Eq. 22 appears to produce larger values in the case of small B , those values are not allowed by the restriction that $f \leq 1$.

The above analysis depends on the parameter λ which we can estimate by studying the correlation between Δp_T^{EM} and Δp_T^{HI} . If we measure in the MC samples, the statistical covariance $Cov(\Delta p_T^{\text{EM}}, \Delta p_T^{\text{HI}})$, then in the formulation here, the covariance reduces to $Cov(\Delta p_T^{\text{EM}}, \Delta p_T^{\text{HI}}) = \lambda Var \Delta_c = \lambda s_c^2$. We could also measure the covariance when not applying the GSC calibration to the EMTopo jets for which

$$\Delta p_T^{\text{EM}}|_{\text{No GSC}} \equiv \lambda \Delta_c + \Delta_{\text{EM}}' \quad (24)$$

and, for which the covariance would reduce to $Cov(\Delta p_T^{\text{EM}}|_{\text{No GSC}}, \Delta p_T^{\text{HI}}) = \lambda^2 s_c^2$. From these two covariances, an estimate for λ could be obtained:

$$\lambda = \frac{Cov(\Delta p_T^{\text{EM}}|_{\text{No GSC}}, \Delta p_T^{\text{HI}})}{Cov(\Delta p_T^{\text{EM}}, \Delta p_T^{\text{HI}})}. \quad (25)$$

Bibliography

- [1] G. Roland, K. Safarik and P. Steinberg, *Heavy-ion collisions at the LHC*, Prog. Part. Nucl. Phys. **77** (2014) 70 (cit. on p. 1).
- [2] W. Busza et al., *Heavy Ion Collisions: The Big Picture, and the Big Questions*, Ann. Rev. Nucl. Part. Sci. **68** (2018) 339, arXiv: [1802.04801 \[hep-ph\]](#) (cit. on p. 1).
- [3] L. Evans and P. Bryant, *LHC Machine*, Journal of Instrumentation **3** (2008) S08001 (cit. on p. 3).
- [4] C. Lefevre, ‘The CERN accelerator complex’, 2008 (cit. on p. 4).
- [5] ATLAS Collaboration, *The ATLAS Experiment at the CERN Large Hadron Collider*, JINST **3** (2008) S08003 (cit. on pp. 6, 7, 16).
- [6] A. La Rosa, *The ATLAS Insertable B-Layer: from construction to operation*, JINST **11** (2016) C12036, arXiv: [1610.01994 \[physics.ins-det\]](#) (cit. on p. 6).
- [7] ATLAS Collaboration, *ATLAS Insertable B-Layer Technical Design Report*, tech. rep., 2010 (cit. on p. 6).
- [8] A Angerami et al., *Jet energy scale determination for heavy ion jet reconstruction: JES for HI jets*, (2014) (cit. on pp. 12, 21, 27).
- [9] ATLAS Collaboration, *Jet energy measurement and its systematic uncertainty in proton-proton collisions at $\sqrt{s} = 7 \text{ TeV}$ with the ATLAS detector*, Eur. Phys. J. C **75** (2015) 17, arXiv: [1406.0076 \[hep-ex\]](#) (cit. on pp. 12, 72).
- [10] ATLAS Collaboration, *Jet energy measurement with the ATLAS detector in proton-proton collisions at $\sqrt{s} = 7 \text{ TeV}$* , Eur. Phys. J. C **73** (2013) 2304, arXiv: [1112.6426 \[hep-ex\]](#) (cit. on pp. 12, 16).
- [11] ATLAS Collaboration, *Jet energy scale measurements and their systematic uncertainties in proton-proton collisions at $\sqrt{s} = 13 \text{ TeV}$ with the ATLAS detector*, Phys. Rev. D **96** (2017) 072002, arXiv: [1703.09665 \[hep-ex\]](#) (cit. on p. 12).

- [12] ATLAS Collaboration, *Measurement of the jet radius and transverse momentum dependence of inclusive jet suppression in Pb+Pb collisions at with the ATLAS detector*, Physics Letters B **719** (2013) 220, ISSN: 0370-2693 (cit. on pp. 12, 16).
- [13] ATLAS Collaboration, *Measurement of jet fragmentation in Pb+Pb and pp collisions at $\sqrt{s_{NN}} = 5.02$ TeV with the ATLAS detector*, Phys. Rev. C **98** (2 2018) 024908 (cit. on pp. 12, 44, 46, 47, 54, 57, 60, 63, 72, 80, 82, 105, 109).
- [14] ATLAS Collaboration, *Measurement of jet fragmentation in 5.02 TeV proton-lead and proton-proton collisions with the ATLAS detector*, Nuclear Physics A **978** (2018) 65, ISSN: 0375-9474 (cit. on pp. 12, 53, 81).
- [15] ATLAS Collaboration, *Measurement of the nuclear modification factor for inclusive jets in Pb+Pb collisions at $\sqrt{s_{NN}} = 5.02$ TeV with the ATLAS detector*, Physics Letters B **790** (2019) 108, ISSN: 0370-2693 (cit. on p. 12).
- [16] ATLAS Collaboration, *Measurement of photon-jet transverse momentum correlations in 5.02 TeV Pb+Pb and pp collisions with ATLAS*, Physics Letters B **789** (2019) 167, ISSN: 0370-2693 (cit. on p. 12).
- [17] ‘ATLAS Production Group MC15c Twiki’, <https://twiki.cern.ch/twiki/bin/view/AtlasProtected/AtlasProductionGroupMC15c> (cit. on p. 13).
- [18] M. Cacciari, G. P. Salam and G. Soyez, *The Anti- $k(t)$ jet clustering algorithm*, JHEP **0804** (2008) 063, arXiv: [0802.1189 \[hep-ph\]](https://arxiv.org/abs/0802.1189) (cit. on pp. 16, 39).
- [19] M. e. a. Cacciari, *FastJet user manual*, The European Physical Journal C **72** (2012) 1, ISSN: 1434-6052 (cit. on p. 16).
- [20] ATLAS Collaboration, *Pile-up subtraction and suppression for jets in ATLAS*, (2013) (cit. on p. 16).
- [21] ‘Jet Et miss Recommendations 2016’, <https://twiki.cern.ch/twiki/bin/view/AtlasProtected/JetEtmissRecommendations2016> (cit. on pp. 16, 17).
- [22] ATLAS Collaboration, *Jet energy scale and its uncertainty for jets reconstructed using the ATLAS heavy ion jet algorithm*, (2015) (cit. on pp. 16, 17, 46, 78).
- [23] A. Sickles, ‘HIRun2JES’, <https://twiki.cern.ch/twiki/bin/view/AtlasProtected/HIRun2JES> (cit. on pp. 17, 39).
- [24] D. Varouchas, *JetResolution2015Prerecom*, <https://twiki.cern.ch/twiki/bin/viewauth/AtlasProtected/JetResolution2015Prerecom> (cit. on p. 21).

- [25] ATLAS Collaboration, *Measurement of jet fragmentation in Pb+Pb and pp collisions at $\sqrt{s_{\text{NN}}} = 2.76 \text{ TeV}$ with the ATLAS detector at the LHC*, Eur. Phys. J. **C77** (2017) 379, arXiv: [1702.00674 \[hep-ex\]](https://arxiv.org/abs/1702.00674) (cit. on p. 32).
- [26] ATLAS Collaboration, HI Jet derivations, <https://twiki.cern.ch/twiki/bin/view/AtlasProtected/HIRun2JetDFRecoDatas> (cit. on p. 32).
- [27] *ATLAS HI Trigger Twiki*, <https://twiki.cern.ch/twiki/bin/view/AtlasProtected/TrigHIRemovedTriggers> (cit. on p. 33).
- [28] ATLAS Collaboration, *ATLAS Run 1 Pythia8 tunes*, (2014) (cit. on p. 34).
- [29] *xAOD Analysis Twiki*, <https://twiki.cern.ch/twiki/bin/view/AtlasComputing/SoftwareTutorialxAODAnalysis> (cit. on p. 37).
- [30] ATLAS Collaboration, *HIAAnalysisTools*, <https://twiki.cern.ch/twiki/bin/view/Main/HIAAnalysisTools> (cit. on p. 37).
- [31] D. Perepelitsa, P. Steinberg, M. Zhou, S. K. Radhakrishnan and S. Tapia Araya, *Centrality determination in $\sqrt{s_{\text{NN}}} = 5.02 \text{ TeV}$ Pb+Pb collision data in 2015*, tech. rep. ATL-COM-PHYS-2016-1287, CERN, 2016 (cit. on p. 38).
- [32] A. Angerami et al., ‘Performance of Jet Reconstruction in Heavy Ion Collisions’, ATL-PHYS-INT-2012-058, <https://cds.cern.ch/record/1462582> (cit. on p. 39).
- [33] ATLAS Collaboration, *Measurements of the Nuclear Modification Factor for Jets in Pb+Pb Collisions at $\sqrt{s_{\text{NN}}} = 2.76 \text{ TeV}$ with the ATLAS Detector*, Phys. Rev. Lett. **114** (2015) 072302, arXiv: [1411.2357 \[hep-ex\]](https://arxiv.org/abs/1411.2357) (cit. on pp. 40, 41, 78).
- [34] ATLAS Collaboration, *Performance of Jet Reconstruction in Heavy Ion Collisions*, (2012), ATL-COM-PHYS-2011-1733, <https://cds.cern.ch/record/1409453> (cit. on p. 44).
- [35] A. Puri, *Cross calibration factors and their uncertainties for application to 2015 heavy ion jets*, tech. rep. ATL-COM-PHYS-2016-1253, CERN, 2016 (cit. on pp. 44, 77, 78).
- [36] ATLAS Collaboration, *Centrality and rapidity dependence of inclusive jet production in 5.02 TeV proton lead collisions with the ATLAS detector*, Physics Letters B **748** (2015) 392, ISSN: 0370-2693 (cit. on pp. 46, 77).
- [37] ATLAS Collaboration, ‘Tracking Recommendations for ICHEP 2016’, <https://twiki.cern.ch/twiki/bin/view/AtlasProtected/TrackingRecommendationsForICHEP2016> (cit. on pp. 46, 79).

- [38] ‘Tracking Recommendations for ICHEP2016’, <https://twiki.cern.ch/twiki/bin/view/AtlasProtected/TrackingCPICHEP2016> (cit. on pp. 51, 79).
- [39] T. Bold, I. Grabowska-Bold, P. A. Janus, J. A. Kremer and M. Przybycien, *Measurement of W boson production in $Pb+Pb$ collisions at $\sqrt{s_{NN}} = 5.02$ TeV - Supporting Note*, tech. rep. ATL-COM-PHYS-2016-828, CERN, 2016 (cit. on p. 53).
- [40] X.-N. Wang and M. Gyulassy, *HIJING: A Monte Carlo model for multiple jet production in $p\ p$, $p\ A$ and $A\ A$ collisions*, Phys. Rev. D **44** (1991) 3501 (cit. on p. 57).
- [41] ATLAS Collaboration, *Measurement of the azimuthal anisotropy of charged particles produced in $\sqrt{s_{NN}} = 5.02$ TeV $Pb+Pb$ collisions with the ATLAS detector*, Eur. Phys. J. **C78** (2018) 997, arXiv: [1808.03951 \[nucl-ex\]](https://arxiv.org/abs/1808.03951) (cit. on p. 62).
- [42] B. Cole et al., ‘Supporting note for measurement of inclusive jet charged particle fragmentation functions in $Pb+Pb$ collisions’, ATL-COM-PHYS-2012-1653 (cit. on p. 62).
- [43] T. Adye, *Unfolding algorithms and tests using RooUnfold*, Proceedings of the PHYSTAT 2009 Workshop, CERN, Geneva, Switzerland, CERN-2011-006, pp 313 (2011), arXiv: [1105.1160 \[physics.data-an\]](https://arxiv.org/abs/1105.1160) (cit. on p. 72).
- [44] ATLAS collaboration, *Jet global sequential corrections with the ATLAS detector in proton-proton collisions at $\sqrt{s} = 8$ TeV*, (2015) (cit. on p. 72).
- [45] G. D’Agostini, *A Multidimensional unfolding method based on Bayes’ theorem*, Nucl.Instrum.Meth. **A362** (1995) 487 (cit. on p. 72).
- [46] G Choudalakis and M Spousta, *Characteristic dip in average transverse energy density and multiplicity around the axis of Anti- kT jets*, tech. rep. ATL-COM-PHYS-2010-139, CERN, 2010 (cit. on p. 74).
- [47] ‘JES Uncertainties Twiki’, <https://twiki.cern.ch/twiki/bin/view/AtlasProtected/JetUncertainties2015ICHEP2016> (cit. on p. 77).
- [48] *JER Uncertainty Provider*, <https://twiki.cern.ch/twiki/bin/view/AtlasProtected/JetEnergyResolutionProvider> (cit. on p. 78).
- [49] ATLAS Collaboration, *Jet energy scale determination for heavy ion jet reconstruction: JES for HI jets*, (2014), ATL-COM-PHYS-2014-329, <https://cds.cern.ch/record/1696485> (cit. on p. 78).
- [50] B. P. Nachman, M. Shapiro and F. Rubbo, *Properties of Jet Fragmentation with the ATLAS detector at $\sqrt{s} = 13$ TeV*, tech. rep. ATL-COM-PHYS-2017-375, CERN, 2017 (cit. on p. 79).

- [51] ATLAS Collaboration, *Measurement of jet p_T correlations in $Pb+Pb$ and pp collisions at $\sqrt{s_{NN}} = 2.76$ TeV with the ATLAS detector*, Phys. Lett. **B774** (2017) 379, arXiv: [1706.09363 \[hep-ex\]](https://arxiv.org/abs/1706.09363) (cit. on p. 82).
- [52] M. Spousta and B. Cole, *Interpreting single jet measurements in $Pb + Pb$ collisions at the LHC*, Eur. Phys. J. C **76** (2016) 50, arXiv: [1504.05169 \[hep-ph\]](https://arxiv.org/abs/1504.05169) (cit. on p. 107).
- [53] O. Collaboration, *A Model independent measurement of quark and gluon jet properties and differences*, Z. Phys. **C68** (1995) 179 (cit. on p. 107).